

## ELECTRIC FIELD EFFECTS ON SINGLE AND SMALL NETWORKS OF NEURONS

by

Robert I. Reznik  
A Dissertation  
Submitted to the  
Graduate Faculty  
of  
George Mason University  
In Partial fulfillment of  
The Requirements for the Degree  
of  
Doctor of Philosophy  
Computational Sciences and Informatics

### Committee:

---

Dr. Evelyn Sander, Dissertation Director

---

Dr. Ernest Barreto, Committee Member

---

Dr. Nathalia Peixoto, Committee Member

---

Dr. Juan Cebral, Committee Member

---

Dr. Kevin Curtin, Acting Department Chair

---

Dr. Donna M. Fox, Associate Dean, Office  
of Student Affairs & Special Programs,  
College of Science

---

Dr. Peggy Agouris, Dean, College of Science

Date: \_\_\_\_\_ Spring Semester 2016  
George Mason University  
Fairfax, VA

Electric Field Effects On Single and Small Networks of Neurons

A dissertation submitted in partial fulfillment of the requirements for the degree of  
Doctor of Philosophy at George Mason University

By

Robert I. Reznik  
Master of Science  
Arizona State University, 1995  
Bachelor of Science  
University of Pittsburgh, 1992

Director: Dr. Evelyn Sander, Professor  
Department of Mathematical Sciences

Spring Semester 2016  
George Mason University  
Fairfax, VA

Copyright © 2016 by Robert I. Reznik  
All Rights Reserved

## **Dedication**

I dedicate this dissertation to my wife Lizet and son Joshua. Lizet, it was not fair. No riches, no fame, only many evenings and sunny weekends spent apart. Not what you bargained for, too many years and too few adventures. More than this thesis I dedicate future hours, days, and years to you and our wonderful son Joshua. To you Lizet, I raise a sweet complex glass of wine and to Josh a fine pouch of strawberry-bannana yogurt.

Love Husband and Dad,  
Robert

## Acknowledgments

I would like to thank my graduate committee: Dr. Evelyn Sander, Dr. Ernest Barreto, Dr. Nathalia Peixoto, and Dr. Juan Cebral for their support and advice. In particular, I would like to thank my adviser Dr. Sander for her considerable investment of time and for teaching such a great course in Mathematical Biology that happened to resonate so well with me. In addition, I would like to thank Dr. Barreto and Dr. Paul So for their time, advice, and collaboration. I also thank my employer Leidos (formerly SAIC) and our clients for their support and understanding. In particular, I would like to thank my managers, Dr. David Gilbert, Mr Martin Allen, Dr. Bill Todd as well as our many clients including Dr. David Hall. Their support and understanding has been invaluable especially during the last six months. I would like to thank my parents and in-laws for their support and invaluable help with our son Joshua the last three years.

## Table of Contents

	Page
List of Tables . . . . .	vii
List of Figures . . . . .	viii
Abstract . . . . .	xxiii
1 Introduction . . . . .	1
2 Effect of Non-Weak Polarization on the Excitability of Elongated Neurons With Active Dendrites. . . . .	4
2.1 Introduction . . . . .	4
2.2 Models and Methods . . . . .	8
2.2.1 Polarizable Pinsky-Rinzel model: approach and computational methods	8
2.2.2 Numerical Methods . . . . .	16
2.3 Results . . . . .	18
2.3.1 TTFS profiles . . . . .	18
2.3.2 Weak polarization region . . . . .	25
2.3.3 Intermediate polarization region . . . . .	25
2.3.4 Strong polarization region . . . . .	27
2.3.5 Effects of Morphology On Excitability . . . . .	35
2.3.6 Polarization-dependent Excitability Using Synaptic AMPA . . . . .	36
2.3.7 Inclusion of $I_h$ current. . . . .	39
2.4 Discussion . . . . .	42
3 Effects of Localized Ephaptic Currents On The Spike Timing of Small Networks of Neurons . . . . .	49
3.1 Introduction . . . . .	49
3.2 Methods . . . . .	55
3.2.1 Polarized two-compartment PR model neuron . . . . .	55
3.2.2 Modeling the extracellular conductance . . . . .	59
3.2.3 Synaptic strength and soma bias current modulate excitability . . . . .	62
3.2.4 Network Architecture . . . . .	63
3.2.5 Simplified models . . . . .	63
3.2.6 Integrals of currents to evaluate neural response to polarization. . . . .	67

3.2.7	Addition of a synaptically isolated and randomly spiking neuron. . . . .	67
3.3	Results . . . . .	67
3.3.1	The ECC from an isolated spike of a single neuron . . . . .	67
3.3.2	Sequentially excited chain with resistance is dominated by nearest-neighbor interactions. . . . .	71
3.3.3	Sequentially excited architecture without extracellular resistance and Type I excitability. . . . .	73
3.3.4	Sequentially excited architecture with resistive lattice. . . . .	75
3.3.5	Initial observations on how the ECC effects TTFS. . . . .	79
3.3.6	Generalization of AP related ephaptic effects using single-neuron models. . . . .	86
3.3.7	Effects of the ECC associated with a randomly spiking, synaptically isolated, neuron on spike-timing. . . . .	89
3.4	Discussion . . . . .	90
4	Conclusion . . . . .	102
	Bibliography . . . . .	104

## List of Tables

Table	Page
-------	------

## List of Figures

Figure		Page
2.1	Two-compartment Pinsky-Rinzel model neuron with electric field. Arrows denote the direction of the currents during stimulation from rest. Differences in potential along the body of a neuron outside the neural membrane induces a polarization within the neuron. Polarization induces a current between the two model compartments. All the active currents in the model involve cations so inward arrows are depolarizing and outward hyperpolarizing. Active currents in the soma are the depolarizing sodium (Na) and the hyperpolarizing potassium-delayed rectifier (K-DR). In the dendrite the calcium (Ca) current is depolarizing while the potassium after-hyperpolarization and potassium-calcium (K-C) are hyperpolarizing. $I_s$ and $I_d$ include any constant baseline currents as well as any stimulating currents. . . . .	13
2.2	Summary schematic of computational protocols used to characterize how polarization affects excitability. $I_{s,inj}(t)$ is the ramp current injected into the soma and is equal to $\bar{I}_s + M(t - t_0)$ where $M$ is in $\mu A/(cm^2 sec)$ . The Time To First Spike (TTFS) is defined as the time it takes for the model neuron's somatic membrane potential to pass through a predefined threshold value. This work will be concerned only with the dynamics driving the polarized neuron from rest to first spike. The TTFS was insensitive to soma potential thresholds above 10 mV. . . . .	13
2.3	For decreasing values of $V_{ds}^{out}$ , the TTFS increases linearly until about $-4$ mV. As $V_{ds}^{out}$ continues to decrease below this value, the TTFS curves display either sublinear (a, b, d) or superlinear (c) behavior depending on the rate of current injection ( $M$ ) and the potassium reversal potential $E_K$ . Here, as for all the computations in this work, $\bar{I}_s = -0.5\mu A/cm^2$ . The weak, intermediate, and strong, polarization regions are labeled. . . . .	19



2.7	The strong polarization region begins where the TTFS starts to decrease as $V_{ds}^{out}$ decreases. Here the TTFS values are calculated for a fast injection rate ( $M = 0.8\mu A/(cm^2 s)$ ) at four different $E_K$ . . . . .	24
2.8	Here we plot the total somatic and dendritic currents, the right-hand sides of $dV_s/dt$ and $dV_d/dt$ . Even at the fastest injection rates the somatic and dendritic potentials change at the same rate. This holds true during the soma injected current for all $E_K$ , $M$ , and $V_{ds}^{out}$ we examined. . . . .	28
2.9	Soma shunting to dendrite. $M = 0.4 \mu A/cm^2$ . $I_{ds}^{in}$ is defined to be the current out of the dendrite and into the soma. Thus, negative values of $I_{ds}^{in}$ indicate that this current flows from the soma to the dendrite. The curves terminate when a somatic membrane potential spike occurs. Compared to the sublinear case the superlinear shunting is increased by approximately 20 percent. This increase in shunting is enough to not only delay a somatic spike, but to cause significant dendritic hyperpolarization. For the case shown, the TTFS increases <i>by approximately 30 % for <math>V_{ds}^{out} = -10 mV</math> to a factor of two for <math>V_{ds}^{out} = -15 mV</math></i> . . . . .	29
2.10	The active dendritic currents for sublinear and superlinear profiles. Here $M = 0.4\mu A/cm^2 s$ and $I_{s,inj} = -0.5\mu A/cm^2$ . In (a) $E_K = -27.5 mV$ and the profile is sublinear. In (b) $E(K = -40 mV)$ and profile is superlinear. The total active dendritic currents are plotted and are equal to the sum of the hyperpolarizing potassium currents, K-AHP and K-C, as well as the depolarizing calcium. $I_{d,active} = I_{K-AHP} + I_{K-C} + I_{Ca}$ . For the sublinear profile the total active dendritic currents are monotonic in time and for increasingly negative $V_{ds}^{out}$ . For the superlinear profile with it's stronger hyperpolarizing currents the total active dendrite currents become non-monotonic with time for polarizations below around $-12 mV$ . Furthermore for polarizations below around $-13 mV$ the total active dendritic currents become net hyperpolarizing.	30
2.11	Plots of the active dendritic membrane currents (left), and for comparison, the total dendritic membrane current (right). The parameters are the same as in Figure 10. . . . .	31



2.16	The proportion of the total membrane area allocated to the soma compartment, $\rho$ , is varied over a range from 0.1 to 0.9. . . . .	38
2.17	For our synaptic AMPA protocol ( $g_{AMPA} = 0.3 \text{ mS/cm}^2$ ) we find a clear split in the $g_{KAHP} - E_K$ parameter space into neurons that fail to spike at some point in the intermediate range and those that have a spiking solution into the strong polarization region. In (a) we have plotted the maximum TTFS obtained in the intermediate polarization region, which we defined as $V_{ds}^{out} \in [-12.5, 0] \text{ mV}$ since this encompassed all of the polarization values capable of producing a maximum TTFS. Polarization values were stepped by 0.075 mV. In (b) we plot the TTFS profiles for four sets of $E_K - g_{KAHP}$ values. Two of them are in the "Fail to spike" region in (a) (white) and two are in the shaded region indicating that they spike throughout the intermediate region and into the strong region. The line marked with circles ( $E_K = -35 \text{ mV}$ and $g_{KAHP} = 0.1 \text{ ms/cm}^2$ ) is close to the boundary and reaches a maximum at around $-10 \text{ mV}$ at which point by our definition it reaches the end of the intermediate region and the beginning of the strong region. . . . .	40
2.18	For the AMPA current protocol, the neurons that fail to spike in the intermediate region and those that do is correlated with a qualitative change in the total active dendritic current. The sets of $E_K - g_{KAHP}$ values in (a)-(d) are the same as in Fig. 2.17 (b). For the two neurons that spike throughout the intermediate region, (a) and (b), The total active dendritic current grows linearly and at nearly the same rate regardless of the polarization. In contrast, for the two neurons that failed to spike the total active dendritic current, after about 10 ms, grows at a much slower rate and shows more pronounced polarization dependence. These observations are consistent with our observations and hypothesis made using the ramp injected protocol about the role of the active dendrite currents. One difference between the ramp injected protocol and the AMPA protocol is that for the ramp injected protocol the total active dendritic current become net hyperpolarizing in the superlinear case (Fig. 2.10 and Fig. 2.12). . . . .	41
2.19	This figure shows $V_{ds}^{out}$ versus $V_s$ , $V_d$ , and $i$ for the resting state (a)-(c) respectively. . . . .	43

2.20 The ramp injected protocol with polarized PR model plus $I_h$ current. The differences between the polarized PR without $I_h$ (square) and the different regulated states of $I_h$ (triangle, circle, star) are most apparent at larger $V_{ds}^{out}$ and at more hyperpolarized dendritic membrane potentials. Also apparent is the significant gap between what has been treated as the high up-regulated state from serotonergic studies [1] (circle) and the most active state used in [2] (star). . . . .	44
2.21 TTFS for different levels of $I_h$ , where darker is faster spiking and white denotes spike failure. The spike failure profile persists with added $I_h$ , but the depolarizing effect of $I_h$ causes quicker TTFS and decreases the size of the spike failure region. . . . .	45
3.1 Pinsky-Rinzel polarized model neuron . . . . .	58
3.2 Schematic of chain of synaptically coupled PR neurons embedded in a resistive lattice. The resistive lattice forms a continuous grid. However, the nth and 1st neurons are not synaptically connected. The resistive grid (i.e. the number of neurons) typically consisted of 51 model neurons. The duration of the computations were often such that only 10 or so neurons spiked. . . . .	60

3.3 Shown is the polarization induced between the soma and dendrite compartments by the ECC of a single spike and the resulting transmembrane potentials. There is no synaptic connectivity. Computations are with 51 PR neurons in a chain embedded in a resistive lattice as in Fig. 3.2. The Nth neuron is stimulated through its synaptic (AMPA) conductance (see methods). As a result the stimulated neuron responds with a single isolated spike. The changing membrane potentials produce ECC that flow to either side of the lattice. In the figure, results are shown only on one side of the stimulated neuron as the results are symmetric around N. (a)-(f) show the polarization,  $V_{ds}^{out}$ , (red) and the somatic and dendritic membrane potentials (blue and black respectively) for the stimulated neuron and its five closest neighbors. In (a) the soma and dendrite spike sharply to above 80 mV and 40 mV respectively (The y-axis is cut off to show the much smaller polarization) in only 1-2 ms. The ECC during this period dominates that produced over the prior 25 ms of subthreshold depolarization. The ECC propagate instantaneously through the lattice but diminishes significantly with distance from the stimulated neuron (b-f). The polarization,  $V_{ds}^{out}$ , and the resulting induced membrane potentials are shown for the five nearest neighbors (g-i). The amplitude decreases with neuronal position, however, the temporal profile of the signal does not change through the purely resistive lattice.

. 69

- 3.4 Time Between Spikes (TBS) down a sequentially excited chain. Results are shown with (b) and without (a) the resistive lattice. The symbol indicates the level of inhibition,  $I_s$ . The less inhibition the shorter the TTFS. Notice that in both cases the gap in TBS grows with increasing inhibition with a dramatic jump going from  $I_s = -0.295 \mu A/cm^2$  to  $I_s = -0.3 \mu A/cm^2$  especially in the resistive lattice case where the TBS more than doubles. This rapid increase in TBS near the bifurcation is shown more explicitly in Figs 3.5 and 3.7 and is characteristic of Type I neurons as discussed in Sec. 3.3.3. Next notice how there is little variation in TBS down the chains except for  $I_s = -0.3 \mu A/cm^2$ . Without the resistive lattice only small differences, proportional to the integration step size, are observed. This is as expected since the only coupling between neurons (without the resistive lattice) is synaptically which by design was made to be nearest-neighbor only. The inclusion of the resistive lattice does provide a global coupling that could introduce variability in the TTFS down the chain. However, in this case (sequentially excited architecture with *standard* resistances), greater than nearest-neighbor ECC effects are evidently negligible except for  $I_s = -0.3 \mu A/cm^2$  which is close to the point where spike failure occurs. . . . .
- 3.5 The TTFS down a synaptically (AMPA) connected chain as a function of excitability ( $I_s$ ) with no resistive lattice and thus no ECC. In (a) the black triangles (lying on the x-axis below  $I_s = -0.3 \mu A/cm^2$ ) denote failure to spike. The TTFS is seen to increase rapidly as  $I_s$  decreases to the threshold for spiking. In (b)-(e) we plot the somatic potential as a function of time for four different  $I_s$  values. In (b) for  $I_s = -0.32 \mu A/cm^2$ , the stimulation from the AMPA conductance ( $g_{AMPA} = 0.142 mS/cm^2$ ) is not sufficient to elicit a spike. In (c)-(e) as the neurons become more excitable the period of latency —a prolonged period of almost constant membrane potential—shrinks. The TTFS here is actually the mean of the differences in consecutive spiking neurons in the chain. The differences in the computed time to pass through 30 mV is nearly identical down the chain (Fig. 3.4) as would be expected given that all PR neurons are identical and the synaptic connectivity is nearest-neighbor. . . . .

70

72



- 3.8 Shown in (a)-(c) are the inter-compartment currents,  $g_c V_{ds}^{out}$  (dash-dot), the AMPA current (dots), and the soma membrane potential,  $V_s$  (solid), for three different values of  $R_{ds}^{out}$ . For each  $R_{ds}^{out}$  the polarization and its current increase in amplitude for increased resistance but the purely resistive lattice maintains the waveform. It is not immediately obvious how the ECC and its resulting polarization effects the TTFS. For example (a) and (c) result in practically the same TTFS even though the amplitude of the polarization current differs by at least a factor of four. The explanation of these effects is the primary subject of the remaining chapter. . . . .
- 3.9 (a) Shows the response of the resistive lattice (no neurons) as a function of  $R_{ds}^{out}$ . The transmembrane currents are replaced by constant currents at the junctions where the somatic and dendritic compartments would be. In this case  $I_d = 4$  nA and  $I_s = 0$  nA so that there is 4 nA of current flowing outside the source neuron from the dendrite to the soma. Shown are the polarizations at the source and the next three posts in the chain. Polarization is symmetric around the source neuron (i.e.  $V_{ds}^{out}(N+x) = V_{ds}^{out}(N-x)$ ). In all cases the neuron-neuron resistances are fixed to the *standard* values ( $R_{dd} = R_{ss} = 0.01R_{ds}^{in}$ ). Filled symbols denote *standard* resistance values of  $R_{ds}^{out}$ . The monotonicity persists over increased  $R_{ds}^{out}$  and increased neural distance from source. (b) We consider the transmembrane currents during an action potential for a single neuron by plotting  $I_s$  (black),  $I_d$  (blue) and  $I_d - I_s$  (red). Notice that the constant 4 nA current used in (a) is only exceeded for a fraction of a millisecond . . . . .

78

80

3.10 For the SE architecture with a resistive array the TTFS is unimodal with increasing resistance along the soma-dendrite axis,  $R_{ds}^{out}$ . In (a) we plot the mean time between spikes as  $R_{ds}^{out}$  is varied for a range of  $I_s$ . As expected the higher  $I_s$  and the more intrinsically excitable the neurons are, the less noticeable the effect of the extracellular resistance. Interestingly, the TTFS has a peak at about the *standard* resistance values. The filled symbols on the left y-axis at  $R_{ds}^{out} = 0.1R_{ds}^{in}$  are the TTFS for the SE architecture with no resistive lattice. In (b) we draw a schematic for the scenario used in the figure. The resistance in red denotes that these values are varied over the range along the x-axis of (a). In this picture, the soma lies beneath the dendrite and the arrows denote that the presynaptic soma triggers the AMPA current in the postsynaptic dendrite. Above we only vary the  $R_{ds}^{out}$  fixing the resistances connecting neuron to neuron to their *standard* values of 0.01  $R_{ds}^{out}$ . In (c) we plot  $V_s$  versus time for three  $R_{ds}^{out}$  at  $I_s = -0.30 \mu A/cm^2$  and correspond to the squares of like colors in (a). As  $R_{ds}^{out}$  increases, the resulting time-varying polarization,  $V_{ds}^{out}$  due to the action potential associated ECC increases in amplitude while maintaining its shape (Fig. 3.3). The effect of this monotonically increasing polarization amplitude on the TTFS is, however, not monotonic and the reasons for this will become clear through the work that follows. . . . .

81

3.11 With the neuron-to-neuron resistances removed the TTFS with respect to  $R_{ds}^{out}$  is monotonically increasing. (a) plots TTFS as a function of  $R_{ds}^{out}$  for a range of  $I_s$ . The filled symbols along the left y-axis are the TTFS for no resistive lattice. (b) shows a schematic for the scenario in this figure. Notice the complete absence of neuron-to-neuron resistance and thus, no neuron-to-neuron flow of ECC. The only effect the extracellular currents of each neuron has is due to self-polarization (referred to as source loading in the Introduction). In (c) we plot  $V_s$  versus time for the same three  $R_{ds}^{out}$  values sampled in Fig. 3.10 and correspond to the squares of like colors in (a). We conclude that the source loading component of the ephaptic effect is inhibitory and from Fig. 3.10 the remaining synaptic coupling and/or the non-synaptic membrane currents must have an excitatory component. . . .

82

- 3.12 The case of no neuron-to-neuron resistance as depicted in Fig. 3.11 (b). Here we show the induced polarization  $V_{ds}^{out}$  (solid) and  $V_s$  (at 1/40th scale) (dotted) for three different  $R_{ds}^{out}$  due to a neurons own action potential in (a) and the resulting decrease in spike width in (b). The polarization current associated with the repolarization of the soma results in further hyperpolarization of the soma and subsequent shorter time above the threshold for AMPA conductance (20 mV). Although the difference in spike width is only several percent, near the threshold to failure to spike the slight difference in AMPA current can make substantial difference in the TTFS. . . . .
- 3.13 This figure illustrates the strong reaction of the sodium current compared to other nonsynaptic membrane currents. Here, a chain of PR neurons is embedded in a full resistive array (as in Fig. 3.10) but without any synaptic connectivity. Depicted are the membrane currents (a) and the polarization current,  $g_c V_{ds}^{out}$ , (b) of a neuron in response to a nearest neighbors' spike. The polarization due to an action potential is a short pulse of less than 2 ms and thus contains high-frequency components that are filtered out by slowly activating currents. Also, the response of a given current will be dependent on the activation state of the potential-dependent channels prior to the spike and associated ECC. This is just one possible state existing at the moment the ECC occurs. In this case, the neuron depicted was completely at rest without any synaptic input and  $V_s \approx -3.75$  mV, and all of the currents are at a very low activation level. We see in (a) that the very fast activating sodium current dominates the somatic Kdr, the dendritic Ca and KAHP currents. The dendritic KC current is negligible and remains constant due to the depletion of  $Ca^{2+}$ . We will show (see for example Fig. 3.17) that the overall effect of the ECC on the membrane currents is excitatory and that the dominant response of the sodium current offers an explanation. . . . .

93

94

3.14 The response of the non-synaptic membrane currents and the polarization-dependent AMPA to a polarization induced by a neighboring AP on a resting neuron is characterized by integrating from when the neuron is at rest through the AP generated ECC and a sufficient time afterward until the neuron returns to rest. In this particular case, in (1) for the non-synaptic quantities we plot the total charge per  $cm^2$  from  $t = 0$  to  $t = 600$  ms.  $Q = \int_0^{600} I_{ion}(t)dt$ . In (b) we plot the total charge per  $cm^2$  for the polarization-dependent, that is  $V_d$  dependent, AMPA conductance,  $Q_{sa} = -g_{AMPA} \int_0^{600} W(t)V_d(t)dt$ . We see in (a) that the total integrated non-synaptic membrane charge (black line with circles) is positive and increases superlinearly with increasing  $R_{ds}^{out}$  and that the biggest contributor is the sodium current. In (b) we see that the increasing polarization with increasing  $R_{ds}^{out}$  leads to increasing depolarization of the post-synaptic dendritic potential and thus a decrease in AMPA. In summary, for the full lattice the response to increasing polarization due to a neighboring AP is excitatory and increases superlinearly with resistance while synaptic coupling term is inhibitory and increases linearly. For the lowest  $R_{ds}^{outs}$  the linearly increasing inhibitory synaptic coupling is dominant then as the  $R_{ds}^{out}$  continues to increase the superlinear the excitatory effect of the non-synaptic currents overtakes the inhibitory effect. . . . .

95

3.15 The TTFS using the single neuron model with interpolated  $V_{ds}^{out}$ . TTFS is computed as a function of both polarization amplitude and the difference in time,  $\tau$ , from the polarization due to a neighboring neuron's action potential and the initiation of synaptic AMPA. On the y-axis  $\tau$  is plotted along with graphical representation of the ECC induced polarization (blue) and the AMPA current red. The x-axis displays the amplitude which is a unitless scalar multiplying the  $V_{ds}^{out}(t)$  due to a neighboring neurons action-potential at standard resistances. Main features include peak inhibitory response around  $\tau = \tau^*$  surrounded by several milliseconds of relatively excitatory responses. For a fixed  $\tau$  the response is always more excitatory with increased polarization amplitude and thus extracellular resistance. . . . .

96

- 3.16 This figure shows different views of the single neuron model with interpolated  $V_{ds}^{out}$  shown in Fig. 3.15. In (a) is a three dimensional view of TTFS showing the change in TTFS as a projected height. In (b) we show for five different  $\tau$ 's around  $\tau^*$  TTFS as a function of Amp. Although the curves resemble the non-monotonic curve found using the full resistive lattice notice that the total difference in TTFS is only about 0.2 ms. In (c) for Amp=1 corresponding to  $R_{ds}^{out} = 0.1R_{ds}^{in}$  we see the pronounced dependence on  $\tau$  around  $\tau^*$ . Also note that by  $\tau = 4$  ms the sensitivity to  $\tau$  is greatly diminished. . . . .
- 3.17 The dependence of TTFS on polarization amplitude and spike timing with synaptic coupling and source loading removed. The response is due to the non-synaptic component of localized ephaptic effect. This single-neuron model uses a linear interpolation function for both  $V_{ds}^{out}$  and AMPA. Here  $I_s = -0.3 \mu A/cm^2$ . The region of inhibition seen in Fig. 3.15 around  $\tau = \tau^*$  is now absent. What remains is an excitatory response due to the non-synaptic currents around  $\tau$  around  $\tau^*$ . This single-neuron model with interpolated  $V_{ds}^{out}$  and with synaptic coupling eliminated is perhaps most similar to experiments of bulk spike propagation in pathologically excited hippocampal tissues with synaptic currents blocked which show increasing spike propagation with increasing EC resistance. . . . .
- 3.18 These are different views of the same data shown in Fig. 3.17. In (a) we can also visualize the response in three-dimensional projection. (b) shows that for  $\tau$  close to  $\tau^*$  the TTFS decreases linearly with increasing polarization amplitude. In (c) for Amp=1 equivalent to  $R_{ds}^{out} = 0.1R_{ds}^{in}$  the TTFS is at a minimum at  $\tau^*$  and increases as the polarization induced by a neighboring neurons spike stops overlapping the input from the interpolated AMPA. . .

97

98

99



## Abstract

ELECTRIC FIELD EFFECTS ON SINGLE AND SMALL NETWORKS OF NEURONS

Robert I. Reznik

George Mason University, 2016

Dissertation Director: Dr. Evelyn Sander

An electric field can polarize a neuron, especially a neuron with elongated dendrites, and thus modify its excitability. In this dissertation, we use computational models, experimental data, and analysis to investigate the effects on neural excitability due to externally applied static electric fields and the extracellular currents generated by a spiking neuron. We apply our results to individual and small networks of neurons. This work has potential implications in the areas of neural prosthetics and therapies to treat a number of neurological conditions such as Depression and Epilepsy. This work also contributes to our understanding of the effects of electric fields endogenous to the brain. We first address the effects of polarization induced by non-weak electric fields on elongated neurons with active dendrites. We find that our model agrees with experimental observation for both weak and strong polarization. For intermediate polarization, we identify novel behavior that should be amenable to experimental verification. Through analysis and modeling, we determine the underlying mechanisms for the observed behavior. Currents that are negligible at weak polarizations and associated with the spiking or bursting phase of a neuron play an important role in the response of a resting neuron to either injected or synaptically generated stimulus. For weak polarizations, small differences in model parameters such as extracellular potassium and rate of current injection yield proportionally small differences in the trajectory of the state

variables of the neuron. However, as polarization strength increases the trajectories begin to diverge falling into either a sublinear or superlinear response categories with respect to polarization. We identify the relative strengths of the hyperpolarizing and depolarizing active dendrite currents as a predictor of polarization-dependent excitability. In the second part of the dissertation we look at localized ephaptic effects due to a single spiking neuron on spike propagation in a chain of synaptically connected neurons. Modeling the extracellular currents using a resistive lattice we observe a non-monotonic relationship between excitability and extracellular resistance. Furthermore, this surprising result is evident for a range of resistances that fall within those estimated using experimentally measured parameters. We define three mechanisms of the localized ephaptic effects; source loading, synaptic coupling, and non-synaptic membrane currents. Through computational experiment and analysis we are able to analyze these effects as a function of the time between the ephaptic polarization and synaptic input as well as extracellular resistance.

## Chapter 1: Introduction

Neurons are often well-described by potentials and currents. Many of the most important ion channels are sensitive to the electric fields that arise from an imbalance of charge on either side of the membrane. The opening and closing of potential-dependent gates that control the flow through these channels and the natural drive towards an electrochemical equilibrium are largely responsible for the observed excitability of a neuron. Directed communication between neurons usually involves the generation of a spike in membrane potential that propagates through neural processes triggering a release of neurotransmitters. The release of neurotransmitters from the presynaptic neuron migrates a short distance to a postsynaptic neuron creating either an excitatory or inhibitory current. It is not surprising then that neurons have been found to be responsive to electromagnetic devices. Long before we knew about ion channels, and several decades before Mary Shelley's Frankenstein, Luigi Galvani [3] observed disembodied frog legs spontaneously contracting when touched with a scissors during an electrical storm. Even earlier, electricity was being used in medicine. Benjamin Franklin described treating a women's convulsions with a static charge (probably from a Leyden jar). Currently, electromagnetic therapies and procedures are being used to treat a number of conditions like depression and Parkinson's disease. However, there are many unanswered questions as to the biophysical mechanisms behind these therapies. In this work, we use computational models to study the interactions between neurons and electric fields. Chapter 2 concerns neurons in non-weak static electric fields, a scenario most likely to be found in experiments *in vivo* or *in vitro* and possibly in neurological therapies. While Chapter 2 deals with non-weak static fields Chapter 3 is concerned with weak oscillating currents generated by neurons themselves.

In Chapter 2 we use a computational model to explain how an applied constant electric field can polarize a neuron and affect its excitability. Our computational model agrees

with experimental measurements in the literature for weak and strong polarizations while predicting novel behavior for intermediate polarizations. Using these results we are able to give a mechanism for this behavior. Our analysis reveals how increasing polarization can, during subthreshold stimulation, lead to significant changes in currents that are negligible when unpolarized. Moreover, these currents only had to be activated very slightly for them to have an effect. In the intermediate polarization region we find that the somatic membrane potential would take one of two qualitatively different trajectories. We find the reason behind such a divergence of trajectories is competition between depolarizing and hyperpolarizing currents in the dendrite.

Often extracellular factors are not modeled. However, there are a number of cases where a cells environment needs to be accounted for. For example, extracellular potassium ion concentration, which can readily affect excitability, is known to depend on both neural activity and glial cells. The motion of charged particles in and out of the cellular membrane results in an extracellular current. Chapter 3 addresses how extracellular currents generated from neural activity affects other neurons. In Chapter 3 we ask the following questions: (1) How is a neuron's excitability affected by the extracellular currents generated by another nearby spiking neuron? (2) How are these effects dependent on the relative timing between when a neuron is polarized by the extracellular current and when that same neuron receives synaptic input? (3) How does this effect depend on the conductivity of the extracellular space? We find that an understanding of the effects of the extracellular currents (*i.e.* ephaptic effects) benefit from segregating the model into three components. These components are: (1) the coupling between synaptic current and the extracellular currents, (2) the response of the non-synaptic membrane currents, and (3) the effect of a neurons own extracellular currents on spike generation. We find that the synaptic coupling is a complicated function of spike timing and extracellular resistance. The coupling can be either inhibitory or excitatory, and it can transition from one to the other with spike timing changes of fractions of a millisecond. The effect on the non-synaptic membrane currents is always excitatory, and the effect due to source loading is always inhibitory. Using analysis and computational

experiments we are able to give the mechanism for the excitatory and inhibitory behaviors. Our work predicts novel spike propagation times as a function of extracellular resistance and are consistent with experimental results when synapses are blocked.

The primary neuron model used throughout this thesis is an eight-dimensional (or nine when we include synaptic AMPA) nonlinear coupled ordinary differential equation. Originated by Pinsky and Rinzel [4]. The model has the advantage of being low dimensional while still comparing favorably to a high dimensional model of Traub [5]. We use a modification derived in [6–8]. In these works, the two-compartment Pinsky-Rinzel model was modified to allow interactions with an external field, namely an applied extracellular difference. The modification of the two-compartment Pinsky-Rinzel model to allow interactions with an external field, or more precisely, an applied extracellular potential difference had been derived previously [6–9]. The solution to the polarized Pinsky-Rinzel model was simply the addition of a current equal to the imposed polarization times the internal conductance of the neuron.  $g_c V_{ds}^{out}$ , running between the dendritic and the somatic compartments. In the first part of this dissertation, the polarization is constant whereas for the second part the polarization is a brief oscillation. This oscillation mirrors the flow of current into and out of a neuron during an action potential. The modeling of the extracellular currents relies on a resistive lattice as in [6–9].

The thesis proceeds as follows: Chapter 2 Effect of Non-Weak Polarization on the Excitability of Elongated Neurons With Active Dendrites has been published and is available online [10]. The code, written in Matlab, is archived at <https://senselab.med.yale.edu/ModelDB/showModel.cshtml?model=185512> and can be searched for under Non-Weak E-Fields Pyramidal Neurons(Reznik et. al., 2015). The code for Chapter 3 contains both Matlab and code for the software XPPAUT [11]. This code will be stored and is accessible at [https://sites.google.com/site/reznikthesis.](https://sites.google.com/site/reznikthesis/)

## **Chapter 2: Effect of Non-Weak Polarization on the Excitability of Elongated Neurons With Active Dendrites.**

If the Lord almighty had consulted me before embarking on creation I should have recommended something simpler.

---

Alphonso X (Alphonso the Wise),  
1221-1284 King of Castile and Leon  
(attributed). Appears opposite Preface  
in J.D. Murray's Mathematical Biology

### **2.1 Introduction**

Neurons, whether in the intact nervous system or in experimental preparations, are commonly subjected to electric fields. These electric fields may be external or endogenous. External sources may be environmental (e.g. power lines, wireless transmissions), or be clinically or experimentally applied. Electric fields are applied to the surface of the brain to affect cortical regions, and probes have been implanted to stimulate sub-cortical regions. Electrical stimuli are currently being used in a number of therapies including those to alleviate depression and the effects of Parkinson's disease. In addition, the search for a viable means of controlling seizures has led to a number of experiments involving electrical stimuli, both *in vitro* and *in vivo*, as well as human trials (for a review see [12]).

Existing therapies using Deep Brain Stimulation (DBS) for Parkinson's disease, depression, and experimental human trials for seizure control use oscillating electric fields. However, there have been some promising experiments where epileptiform activity was suppressed through the application of constant electric fields or constant fields applied in pulses at very low frequencies. These experiments include placing a hippocampal slice between

electrodes to establish a DC field [13–16], and applying a single DC pulse onto a  $Cs^+$  model of epilepsy [17]. *In vivo* experiments include polarizing low-frequency electric fields (PLEF) in a rat model of epilepsy [18, 19].

Therapeutic methods that are applied proximally to the scalp and act on the cortex are attractive since they are non-invasive. One such method is Transcranial Direct Current Stimulation (tDCS). Typically tDCS uses two electrodes positioned on top of the head, and current flows from them through the skull, with a fraction of the current reaching the cortex. The electric fields and induced polarization on cortical neurons due to tDCS are estimated to be low, with fields of less than  $1V/m$  and cell membrane polarization less than  $1mV$  [20, 21]

Endogenous electric fields include those associated with the normal rhythmic activity of populations of neurons (e.g., the theta and gamma rhythms). In the hippocampus, endogenous field strengths range from about  $2 - 70$  mV/mm in amplitude [22]. The susceptibility of the somatic transmembrane potential to be polarized has been estimated for both DC and AC fields. The polarization of CA3 pyramidal somata to a DC field has been found to be nearly linear up to, at least, 16 mV/mm, yielding a constant susceptibility or polarization length of 0.18 mm. [23] and [24, 25] have measured hippocampal and cortical pyramidal neurons and found their polarization lengths to be between about 0.1 mm and 0.5 mm, and most frequently near 0.2 mm. For AC fields, the susceptibility is frequency dependent with higher frequencies being less polarizing as the neuron acts as a low-pass filter. At 10 Hz, the polarization length is about 0.225 mm, and at 100 Hz it is 0.05 mm [23]. In addition, near constant uniform fields have been detected up to 7.5 mV/mm and associated with changes in the potassium concentration that emerge along with neural hyperactivity [26].

Despite its importance, our understanding of how electric fields interact with and affect the functioning of neural populations remains incomplete. An understanding of such phenomena and their potential medical implications requires a careful analysis of effects on both single neurons and populations due to electric fields with a range of amplitudes, frequencies, and waveforms. Here we focus on the simplest case of a single neuron subject to

a constant uniform field. This study serves as a step towards understanding the excitability of elongated neurons with active dendrites subject to electric fields. The results here may be relevant to *in vivo* and *in vitro* work involving DC fields.

In response to a uniform electric field, charge within a cell spreads out along the field lines until an obstruction such as a cell wall is encountered. The resulting charge distribution creates polarization within the neuron. Here, when we speak of polarization, we are referring to the shift in membrane potential due to imposed differences in the extracellular potential along the neuron. The sensitivity of neurons, particularly elongated pyramidal neurons, to even low amplitude electric fields has been shown experimentally ([27]). Computational models of polarization and its effects on single neurons have ranged from a detailed finite-element model ([28]) to single-compartment models ([29, 30]). Another approach has employed multi-compartment models with an electric potential applied across the compartments. These compartment models have varied in complexity from two-compartment models ([6–8]) to a 19-compartment model ([9, 31]). Several studies, including this one, use the model of [4], which is itself a simplified version of the 19-compartment model of [32]. Recently a bifurcation study of neural excitability in response to polarization has been applied to a two-compartment modified Morris-Lecar model with passive dendrites [33]

Experiments ([13, 24, 25]) have shown that as long as the polarization is not too great, the somatic transmembrane potential of pyramidal neurons at rest is linearly proportional to the degree of polarization. In addition, changes in spike timing in response to an injected ramp current were found to vary linearly with polarization in the range studied, which was  $3 - 5 \text{ mV}$ . These results could be explained by a simple leaky (*i.e.* passive conductance) integrate-and-fire model. Accordingly, we define the weak polarization region as those values of polarization for which the neuron behaves passively, *i.e.*, the membrane conductances remain constant. Systematic measurements of the size of this linear response region are lacking, as they have not been the focus of previously published work.

The emphasis on smaller electric fields is understandable. Many medical applications seek the least invasive methods. Also, endogenous field effects such as the gamma and

theta oscillation in the hippocampus are often only several millivolts in amplitude [34] and thus probably within the passive region. We may estimate, however, that there exist some instances for which a neuron might experience polarization outside the passive region. As mentioned above, the length over which the electrical polarization is relevant in a uniform field has to be between 0.1 mm and 0.5 mm. Experiments on hippocampal slices have used field strengths exceeding 100  $mV/mm$  [13, 35] implying that pyramidal neurons may have experienced polarizations in excess of 50 mV. Very low frequency pulses were applied to the Rat hippocampus yielding an estimated 16-20 mV/mm electric field [18]. For moderate to high polarization lengths, such a field would induce a polarization outside of the weak region. The polarization of a pyramidal neuron in the hippocampus due to oscillating endogenous fields is harder to estimate. As noted above, the polarization decreases with increasing frequency and the largest amplitude endogenous fields, sharp waves, and epileptic discharges are associated with higher frequencies ( $> 50$  Hz). To exceed the outer limit of the weak polarization region, 5 mV, at the maximum estimated endogenous field amplitude of 70 mV/mm, a sensitivity of at least 0.07 mm is required. The 0.07 mm is, in fact, what was measured for a CA3 pyramidal cell at 50 Hz [23].

In this study, we explore the effects and underlying mechanisms over a broader range of polarizations, with emphasis on the effects beyond the weak polarization regime. We use the model of [4] and modify it to allow for an imposed extracellular potential difference between the two compartments. Polarization is then parametrized by this potential difference. With this model we study how polarization affects excitability and how changes in the extracellular potassium concentration and the rate of stimulating current injection modifies these effects. We chose the Pinsky-Rinzel (PR) model because it has the minimum number of compartments (two) needed to explore the effects of polarization on a neuron with distinct and spatially segregated ion channels. Furthermore, the PR model uses experimentally-derived ion channel kinetics to model specific currents, allowing for a more physiological interpretation compared to simplified lower-dimensional models.

In section II (Models and Methods) we derive the polarized PR model, present our stimulation protocol, define the time-to-first spike (TTFS), and discuss our numerical methods. In section III (Results) we present curves of TTFS as a function of polarization for different injection rates and extracellular potassium concentrations. We perform our computations over a range of inter-compartmental conductances and ratios of somatic to dendritic membrane surface area. These results are first computed using a commonly-used current injection protocol that might be amenable to experiment. To examine a more biologically plausible model, we subject the polarized model neuron to synaptic (AMPA) excitation. Lastly, we see how our results change when we introduce  $I_h$  currents into the dendritic compartment. In section IV (Discussion), we summarize our results and consider how they might be generalized to biological neurons.

## 2.2 Models and Methods

### 2.2.1 Polarizable Pinsky-Rinzel model: approach and computational methods

In the PR model, the primary ionic mechanisms for depolarization are the sodium ion channels of the soma and the calcium channels of the dendrite. Hyperpolarizing currents are provided by the  $I_{K-AHP}$  and  $I_{K-C}$  in the dendrite and  $I_{K-DR}$  in the soma. Current between the somatic and dendritic compartments flow passively in proportion to the potential difference. The somatic and dendritic membrane potentials, the calcium level in the dendrite, four voltage-dependent gates, and one calcium-dependent gate constitute a system of eight coupled ordinary differential equations. In this work, we focus on the effects that polarization *induced* by electric fields have on a neuron's dynamics. The source for the electric field, how it couples into the extracellular medium and how charge redistributes itself around the neural membrane will not be considered (for details into field calculations see for example [36–38]). The component of the electric field relevant to the neural dynamics is along the soma-dendrite axis and is modeled by the outside potential difference between

the soma and the dendrite,  $V_{ds}^{out}$ . The polarization is then parameterized by  $V_{ds}^{out}$ .

We modify the PR model to accommodate this polarization between compartments as was done in [6–8]. The transmembrane potential is defined by the difference in potential across the cell membrane.

$$V_s = V_s^{in} - V_s^{out} \quad (2.1a)$$

$$V_d = V_d^{in} - V_d^{out} \quad (2.1b)$$

Membrane channels are functions of the transmembrane potentials. However, current flowing passively between the two compartments is proportional to the difference in their intracellular potentials,  $V_s^{in}$  and  $V_d^{in}$ . The original PR model, as in most models, implicitly assumed a constant extracellular potential,  $V_s^{out} = V_d^{out}$ . In this case, the intracellular potential between compartments,  $(V_d^{in} - V_s^{in})$ , is equal to the difference in transmembrane potentials,  $(V_d - V_s)$ .

Allowing for our compartments to have two different extracellular potentials, we define the potential difference directly outside the dendrite and soma as  $V_{ds}^{out} \equiv V_d^{out} - V_s^{out}$ . With the inter-compartment conductance given by  $g_c$  and  $\rho$  defined as the fraction of somatic surface area to the total cell surface area, the current out of the dendrite and into the soma is defined as  $I_{ds}^{in}$  and is given by:

$$\begin{aligned} I_{ds}^{in} &= \frac{g_c}{\rho} (V_d^{in} - V_s^{in}) \\ &= \frac{g_c}{\rho} (V_d - V_s + V_{ds}^{out}). \end{aligned} \quad (2.2)$$

The polarized PR model follows,

$$C_m \cdot dV_s/dt = I_{sLeak}(V_s) + I_{Na}(V_s, h) + \\ I_{K-DR}(V_s, n) + I_{ds}^{in} + I_{s,inj}(t)/\rho, \quad (2.3a)$$

$$C_m \cdot dV_d/dt = I_{dLeak}(V_d) + I_{Ca}(V_d, s) + \quad (2.3b)$$

$$I_{K-AHP}(V_d, q) + I_{K-C}(V_d, Ca, c) -$$

$$I_{ds}^{in} \frac{\rho}{1 - \rho}$$

$$dCa/dt = -0.13I_{Ca} - 0.075Ca \quad (2.3c)$$

$Ca$  represents a unitless measure of the amount of intra-cellular calcium,  $Ca^{2+}$ . In the equation governing intra-cellular calcium levels, the coefficient  $-0.075$  is based on optical measurements of the decay of calcium in Purkinje dendrites ( $-0.075s^{-1} = 1/\tau_{Ca} = 1/13.33ms$ ) [32, 39]. The sign of the coefficient  $-0.13$  multiplying  $I_{Ca}$  means that current into the dendritic compartment results in an increase in intracellular calcium [32]<sup>1</sup>. The only difference between the polarized PR model and the original one is the addition of the terms  $I_{ds}^{in}$  and  $-I_{ds}^{in}\rho/(1 - \rho)$  in the equations for the somatic and dendritic compartments, respectively. Note that since we define  $\rho$  as the fraction of somatic surface area to total surface area,  $I_{ds}^{in}$  is then defined as current per total soma area. In this work, as in the original PR model and the models used in the Park et al. works referenced above, we shall assume that the somatic and dendritic compartment surface areas are equal, so that  $\rho = 0.5$  and the flow of current from the soma to the dendrite is  $-I_{ds}^{in}$ . The individual currents with

---

<sup>1</sup>[32] presents an abstract model of intracellular calcium where each compartment's rate of absorption can be varied by varying the thickness of an imagined sub-cellular membrane. This coefficient was fine-tuned to best match experimental data.

their dependencies on the dynamic gating variables  $h$ ,  $n$ ,  $s$ ,  $c$ , and  $q$  follow.

$$\begin{aligned}
I_{sLeak} &= -g_L(V_s - E_L) \\
I_{dLeak} &= -g_L(V_d - E_L) \\
I_{Na} &= -g_{Na}m_\infty^2 h(V_s - E_{Na}) \\
I_{K-DR} &= -g_{K-DR}n(V_s - E_k) \\
I_{Ca} &= -g_{Ca}s^2(V_d - E_{Ca}) \\
I_{K-AHP} &= -g_{K-AHP}q(V_d - E_k) \\
I_{K-C} &= -g_{K-C}c\chi(V_d - E_k)
\end{aligned} \tag{2.4}$$

These currents and whether they flow inward (depolarizing) or outward (hyperpolarizing) at typical steady-state values are depicted by arrows in Fig. 2.1. Note that for our model, a cathode is imagined to be placed near the soma and the anode near the apical dendrites, so that a positive (negative) field depolarizes (hyperpolarizes) the soma and hyperpolarizes (depolarizes) the dendrite. Note that this convention is a reversal in field sign from that found in [13, 24, 25], and [29], but follows that used in [7, 8]. There are five gating variables ( $h$ ,  $n$ ,  $s$ ,  $c$ , and  $q$ ) whose kinetics take on the standard Hodgkin-Huxley form. The gating variables  $h$  and  $n$  are functions of  $V_s$ ,  $s$  and  $c$  are functions of  $V_d$ , and both  $q$  and  $\chi$  are functions of the intracellular calcium concentration  $Ca$ . Equations 3.3 and 3.4 are thus

coupled with the five first-order gating kinetics given below:

$$dh/dt = (h_\infty(V_s) - h)/\tau_h(V_s) \quad (2.5a)$$

$$dn/dt = (n_\infty(V_s) - n)/\tau_n(V_s) \quad (2.5b)$$

$$ds/dt = (s_\infty(V_d) - s)/\tau_s(V_d) \quad (2.5c)$$

$$dc/dt = (c_\infty(V_d) - c)/\tau_c(V_d) \quad (2.5d)$$

$$dq/dt = (q_\infty(Ca) - q)/\tau_q(Ca). \quad (2.5e)$$

For our model, the stimulus is a ramp current,  $I_{ramp}$ , injected into the soma. The term  $I_{s,inj}$  in Equation 3.3 is the sum of the ramp current and a constant bias current,  $\bar{I}_s$ . For the computations reported here,  $\bar{I}_s = -0.5\mu A/cm^2$ , which was used as the standard value in the original PR model.

$$I_{s,inj}(t) = \bar{I}_s + I_{ramp}(t) \quad (2.6)$$

where  $I_{ramp}$  is defined as the following linearly increasing function with ramp rate  $M$ .

$$I_{ramp}(t) = M(t - t_0). \quad (2.7)$$

The ramp protocol, illustrated in Fig. 2.2, calls for the current density to be steadily increased until the soma is depolarized to 30 mV. Note that in Traub's 19-compartment model and the PR model, the potentials are normalized such that the resting potential of the unpolarized neuron is 0 mV. In our numerical experiments, we estimate the TTFS as the time when the somatic membrane potential reaches 30 mV. The metric TTFS is used since it is relevant to excitable but resting neurons, and pyramidal neurons are typically associated with such states.

We adopt the numerical values for the reversal potentials and conductances as given in

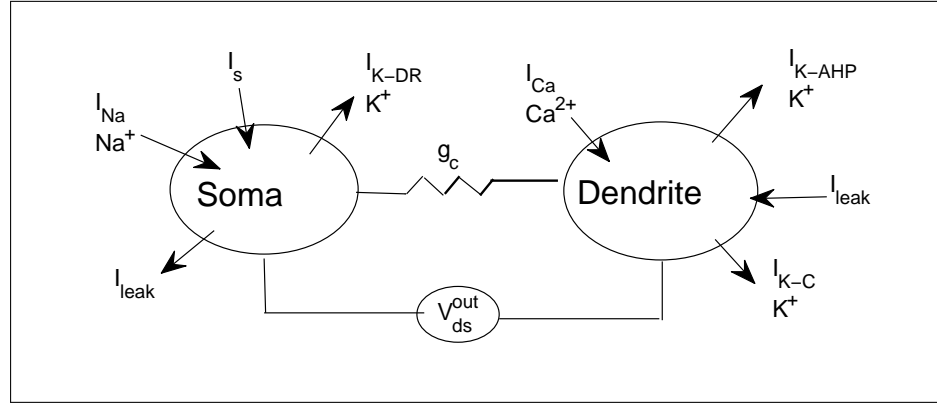


Figure 2.1: Two-compartment Pinsky-Rinzel model neuron with electric field. Arrows denote the direction of the currents during stimulation from rest. Differences in potential along the body of a neuron outside the neural membrane induces a polarization within the neuron. Polarization induces a current between the two model compartments. All the active currents in the model involve cations so inward arrows are depolarizing and outward hyperpolarizing. Active currents in the soma are the depolarizing sodium ( $\text{Na}^+$ ) and the hyperpolarizing potassium-delayed rectifier ( $\text{K-DR}$ ). In the dendrite the calcium ( $\text{Ca}^{2+}$ ) current is depolarizing while the potassium after-hyperpolarization and potassium-calcium ( $\text{K-C}$ ) are hyperpolarizing.  $I_s$  and  $I_d$  include any constant baseline currents as well as any stimulating currents.

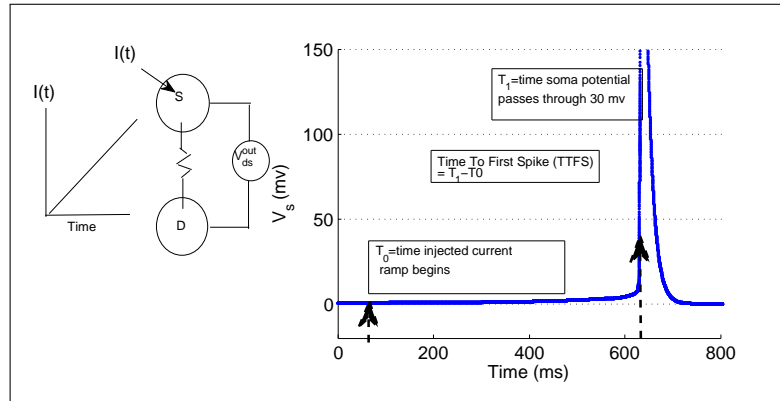


Figure 2.2: Summary schematic of computational protocols used to characterize how polarization affects excitability.  $I_{s,inj}(t)$  is the ramp current injected into the soma and is equal to  $\bar{I}_s + M(t - t_0)$  where  $M$  is in  $\mu\text{A}/(\text{cm}^2 \text{sec})$ . The Time To First Spike (TTFS) is defined as the time it takes for the model neuron's somatic membrane potential to pass through a predefined threshold value. This work will be concerned only with the dynamics driving the polarized neuron from rest to first spike. The TTFS was insensitive to soma potential thresholds above 10 mV.

the original PR model:

$$\begin{aligned}
E_{Na} &= 120 \text{ mV}, E_L = 0 \text{ mV} \\
E_{Ca} &= 140 \text{ mV}, C_m = 3 \text{ uf/cm}^2 \\
g_L &= 0.1 \text{ mS/cm}^2, g_{Na} = 30 \text{ mS/cm}^2 \\
g_{K-DR} &= 15 \text{ mS/cm}^2, g_{K-AHP} = 0.8 \text{ mS/cm}^2 \\
g_{K-C} &= 15 \text{ mS/cm}^2, g_{Ca} = 10 \text{ mS/cm}^2 \\
g_c &= 2.1 \text{ mS/cm}^2, \rho = 0.5, \bar{I}_s = -0.5 \mu A/cm^2
\end{aligned} \tag{2.8}$$

The extracellular potassium concentration,  $[K^+]_o$ , controls the reversal potentials of the somatic hyperpolarizing potassium-delayed rectifier current  $I_{K-DR}$ , the dendrite-hyperpolarizing calcium-activated potassium current  $I_{K-C}$ , and the after-hyperpolarizing potassium current  $I_{K-AHP}$ . Extracellular potassium levels are known to increase with increased neuronal activity [40], and the increasing extracellular potassium in turn excites the surrounding neurons. However, the positive feedback between neural hyper-activity and extracellular potassium is modulated by Glia cells which tend to suppress high extracellular potassium through uptake and spatial buffering. For more on the dynamics of the ion concentrations and its effects on neuronal behavior see [41–43].  $E_K$  in the polarized PR model is related to the extracellular potassium concentration through the Nernst equation. Since the extracellular potassium is known to vary *in vivo* and can be manipulated in the laboratory we examined the excitability of the polarized PR model over a range of physiologically plausible  $E_K$  and corresponding extracellular potassium concentrations. The higher the extracellular potassium concentration the higher the reversal potential. Here we varied  $E_K$  from  $-25 \text{ mV}$  to  $-45 \text{ mV}$ . To place these values in context note that a reversal potential of  $E_K = -38.56 \text{ mV}$  has been associated with a normal potassium environment [8]

corresponding to  $[K^+]_o = 3.5 \text{ mM}$  assuming  $[K^+]_i = 140 \text{ mM}$  and  $T = 36.9^\circ\text{C}$ . A high extracellular potassium concentration is  $[K^+]_o = 8.45 \text{ mM}$  corresponding to  $E_K = -15 \text{ mV}$  and is associated with spontaneous periodic bursting. Such high potassium levels have been measured in hippocampal slices exhibiting epileptic like activity [44] and *in vivo* in seizing cats [40].

In section 3.6 we replace the ramp current stimulus with synaptic AMPA input modeled as in Pinsky and Rinzel (1994) and Park et al. (2003, 2005). This class of model for synaptic conductance assumes that the transmitter release is always at a maximum as long as the pre-synaptic potential  $V_{s,pre}$  exceeds a certain threshold potential. The equation for the AMPA synaptic conductance is as follows:

$$I_{AMPA} = \bar{g}_{AMPA} W(t)(V_d - V_{syn}) \quad (2.9)$$

$$W' = H(V_{s,pre} - 20) - W/2,$$

where  $H$  denotes the Heaviside function. We apply the AMPA current by defining  $V_{s,pre}$  as follows:

$$V_{s,pre} = AH(t - t_i)H(t_i + t_{spkdur} - t) \quad (2.10)$$

$$t_{spkdur} = 1.2 \text{ ms}$$

$$A > 20 \text{ mV}$$

In section 3.7, we include a model of the  $I_h$  current into our polarized PR model. We model  $I_h$  model as in [2] and [45]. The family of  $I_h$  currents have a unique set of characteristics including an inward current activated at hyperpolarized membrane potentials, significant current at rest, moderately long time constants, and various regulated states characterized by changes in channel density and activation potentials. Here, we use  $i$  to

denote the  $I_h$  gating variable. The model is

$$I_h = g_h i(V_d - E_h) \quad (2.11a)$$

$$di/dt = (i_\infty(V_d) - i)/\tau_i(V_d) \quad (2.11b)$$

$$i_\infty = \frac{a_i(V_d)}{a_i(V_d) + b_i(V_d)} \quad (2.11c)$$

$$\tau_i = \frac{500}{a_i(V_d) + b_i(V_d)} \quad (2.11d)$$

$$a_i(V_d) = \exp(0.1054(V_d - V_{i-half})) \quad (2.11e)$$

$$b_i(V_d) = \exp(0.1581(V_d - V_{i-half})) \quad (2.11f)$$

a and b determine the steady-state value,  $i_\infty$ ,  $\tau_i$  is the time constant, and  $V_{i-half}$  is the half-activation parameter. Also as in [2] we adopted four pairs of  $g_h$  and  $V_{i-half}$  parameter values representing a control state ( $0.03 \text{ mS/cm}^2$ ,  $-21 \text{ mV}$ ), a low level of  $I_h$  up-regulation ( $0.035 \text{ mS/cm}^2$ ,  $-18 \text{ mV}$ ) and a high level of up-regulation ( $0.04 \text{ mS/cm}^2$ ,  $-15 \text{ mV}$ ) in accordance with serotonergic modulation of  $I_h$  [1]. To this we also added the most highly-regulated state looked at by [2] ( $0.06 \text{ mS/cm}^2$ ,  $-11 \text{ mV}$ ). Here, as before the reversal potentials are normalized to correspond with a resting potential of 0 mV for the unpolarized neuron.

## 2.2.2 Numerical Methods

### Computing the TTFS

When performing calculations on excitability, we used only those polarizations for which a stable resting equilibrium exists. The polarized Pinsky-Rinzel neuron was coded in MATLAB. MATLAB's ODE23 was used for integrating the eight-dimensional coupled nonlinear ODE of Eqs. 3.3 – 2.7 with the parameter set given in Eq. 2.8. For a given choice of  $E_K$

and  $M$ , a TTFS profile was generated over a range of  $V_{ds}^{out}$  for which the model neuron was stable prior to any injected current. The range of  $V_{ds}^{out}$  for which the resting equilibrium is stable varied with  $E_K$ , but was found to be continuous and generally ranged from around  $+15\text{ mV}$  to  $-30\text{ mV}$ . Stability was first calculated using a nonlinear root-finding method after setting the gating variables and  $Ca$  to their equilibrium values. As a further measure to insure stability, the solutions were integrated for  $50\text{ ms}$  prior to the start of ramp injection. To estimate the sensitivity to numerical methods, MATLAB's higher order ODE45 was used in the integration and these were shown to yield TTFS values that differed less than  $10^{-9}$  from those of the faster ODE23. We define a single run of our system to be the computation of the TTFS for a particular  $V_{ds}^{out}$ ,  $E_K$  and  $M$ .

### Numerical analysis of TTFS profiles

In the intermediate polarization region, it was observed that either the TTFS grew sublinearly or superlinearly with  $V_{ds}^{out}$  depending on  $E_K$  and  $M$ . To quantify the curvature found in the resulting TTFS profiles with respect to the imposed  $V_{ds}^{out}$ , we computed a second-order centered difference using the TTFS data points. These were calculated at every  $V_{ds}^{out}$ . It was observed that within the intermediate polarization region,  $V_{ds}^{out} \in [-4\text{mV}, -15\text{mV}]$ , the numerically-calculated second derivatives did not change sign as we varied  $V_{ds}^{out}$ . This means that for a particular  $E_K$  and  $M$ , the solution remained either sublinear or superlinear over the intermediate polarization, thus allowing us to unambiguously define a sublinear and superlinear profile by the sign of the second derivative at any of the intermediate polarizations. To bound the values for  $M$  at a given  $E_K$  at which the profile transitioned between sublinear and superlinear, we increased  $M$  starting at the very slow injection rate of  $0.05\mu A/(cm^2 s)$ . At this value, the second derivative was always found to be negative, indicating a superlinear profile. As  $M$  increased, we determined when the second derivative became positive. The second derivative was computed at  $0.25\text{ mV}$  steps over the intermediate polarization and over a grid of  $E_K$  and  $M$  values.  $E_K$  was varied from  $-20\text{ mV}$  to  $-45$

$mV$  in steps of  $2.5\text{ mV}$ , while  $M$  varied from  $0.1\text{ }\mu A/(cm^2sec)$  to  $0.8\text{ }\mu A/(cm^2sec)$  in steps of  $0.05\text{ }\mu A/(cm^2sec)$ . For each  $E_K$ , the lowest  $M$  value for which the second derivative of the profile became positive was used to estimate the boundary curve separating sublinear and superlinear profiles. Sensitivity to step size was evaluated by performing the same algorithm but for a much smaller step size of  $0.075\text{ mV}$ . The smaller step sizes resulted in small changes in the second derivative and did not qualitatively change the boundary curve in the  $E_K - M$  parameter space.

Code for computations, analysis, and graphics were written in MATLAB and are available online at ModelDB (<http://senselab.med.yale.edu/modeldb/>)

## 2.3 Results

### 2.3.1 TTFS profiles

Fig. 2.3 shows four plots of TTFS as a function of  $V_{ds}^{out}$ . Each data point on the plot is obtained by integrating Eqs. (3.3–2.7) (see Methods) with parameters as in Eq. 2.8 for the specific values of  $V_{ds}^{out}$ ,  $M$ , and  $E_k$  indicated in the figure, and measuring the time until  $V_s$  exceeds  $30\text{ mV}$ . Each of the plots is obtained using either a high ( $-25\text{ mV}$ ) or low ( $-45\text{ mV}$ )  $E_k$ , and a slow ( $0.3\text{ }\mu A/(cm^2s)$ ) or fast ( $0.8\text{ }\mu A/(cm^2s)$ ) current injection rate  $M$ . In each case there is a range of polarization for which the TTFS is linear with  $V_{ds}^{out}$ , and a range at stronger soma-hyperpolarizing fields for which the TTFS is no longer linear with polarization. We call the linear range the weak polarization region. We define the extent of the weak polarization region by noting the most negative polarization for which the  $R^2$  measure<sup>2</sup> stays above 0.99. In all four cases the TTFS profile deviates from our  $R^2$  criterion at  $V_{ds}^{out} = -4\text{ mV}$ , which is consistent with experimental observation (i.e., departure from linearity between  $-3\text{ mV}$  and  $-5\text{ mV}$ ; see Introduction). Outside the weak polarization region, we see in Fig. 2.3 that both  $E_k$  and  $M$  affect how TTFS varies with polarization. For  $E_k = -45\text{ mV}$ , the fast current injection rate yields a sublinear TTFS profile (Fig. 2.3

---

<sup>2</sup> $R^2 \equiv 1 - (\text{sum square of residuals}) / (\text{sum square of differences of the dependent variable from the mean})$

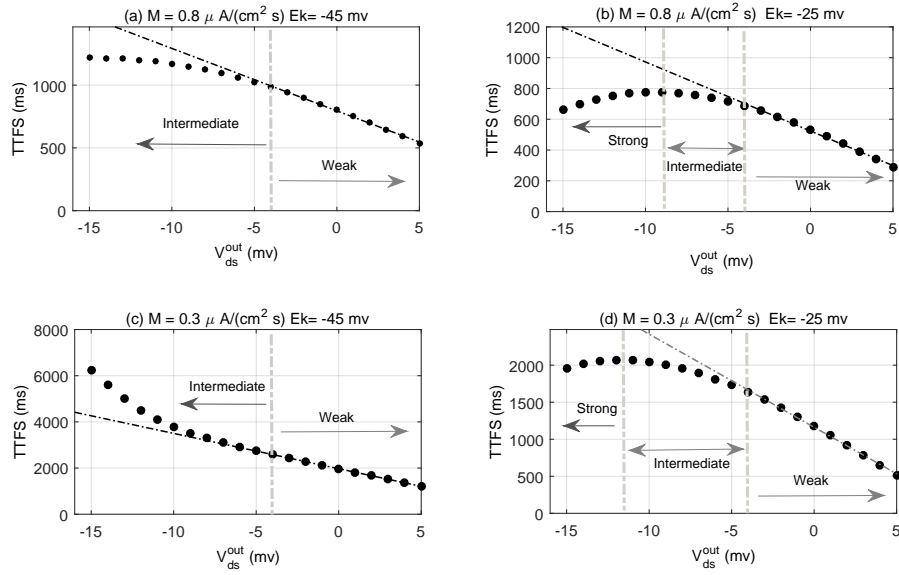


Figure 2.3: For decreasing values of  $V_{ds}^{out}$ , the TTFS increases linearly until about  $-4 mV$ . As  $V_{ds}^{out}$  continues to decrease below this value, the TTFS curves display either sublinear (a, b, d) or superlinear (c) behavior depending on the rate of current injection ( $M$ ) and the potassium reversal potential  $E_K$ . Here, as for all the computations in this work,  $\bar{I}_s = -0.5 \mu A/cm^2$ . The weak, intermediate, and strong, polarization regions are labeled.

a), while the slower ramp injection yields a superlinear one (Fig. 2.3 c). For  $E_k = -25\text{ mV}$ , the profile is sublinear for both injection rates (Fig. 2.3 b and d).

In Figs. 4 and 5 we show the behavior of the transmembrane potential of the soma versus time, where we continue to integrate our model past the occurrence of the first spike, maintaining a constant current injection at the soma equal to the ramp current at the time of the first spike. Results are shown in Fig. 2.4 for  $M = 0.3\text{ }\mu\text{A}/(\text{cm}^2\text{s})$  and Fig. 2.5 for  $M = 0.8\text{ }\mu\text{A}/(\text{cm}^2\text{s})$ . In both cases, we examine the situations with  $E_K = -25\text{mV}$  and  $-45\text{mV}$ . We classify the spiking behavior of the soma using two characteristics: (1) whether or not a particular waveform (a single spike or burst of activity) repeats periodically over a long duration ( $> 20\text{ms}$ ) or if it is limited to a single spike or burst of activity, and (2) by the number of individual spikes occurring within a particular waveform. For periodicity, we classify the activity as a single burst or spike if there is only one occurrence of a particular waveform within our run-time of 10 seconds and is denoted by an open symbol. The number of somatic membrane potential spikes in each waveform are encoded by the symbol shapes (see figure caption). A number of spiking behaviors are observed over the  $E_K$  and  $M$  values chosen. In particular, note that the sublinear profiles at weak polarizations exhibit periodic spikes or bursts, and at intermediate to strong polarizations, show only isolated spikes or bursts. In contrast, the superlinear profile exhibits isolated spikes at weak polarizations and becomes periodic towards the end of the intermediate polarization region. Thus, qualitative differences between sublinear and superlinear profiles appear in spiking behavior as well as the TTFS.

Fig.2.6 shows how the occurrence of sub- or super-linear TTFS profiles in the intermediate region depend more generally on  $E_k$  and  $M$ . The data points divide the parameter space into regions in which the system exhibits sub- and superlinear behavior in the intermediate polarization region where the second-derivative test is unambiguous (see 2.2.2). Note that the accuracy of the line dividing the sublinear and superlinear regions is limited by our choice of discretization in  $M$  (i.e., steps of size  $0.05\mu\text{A}/(\text{cm}^2\text{s})$ ).

Note that for the sublinear case shown in Fig. 2.3 b the TTFS curve turns over and

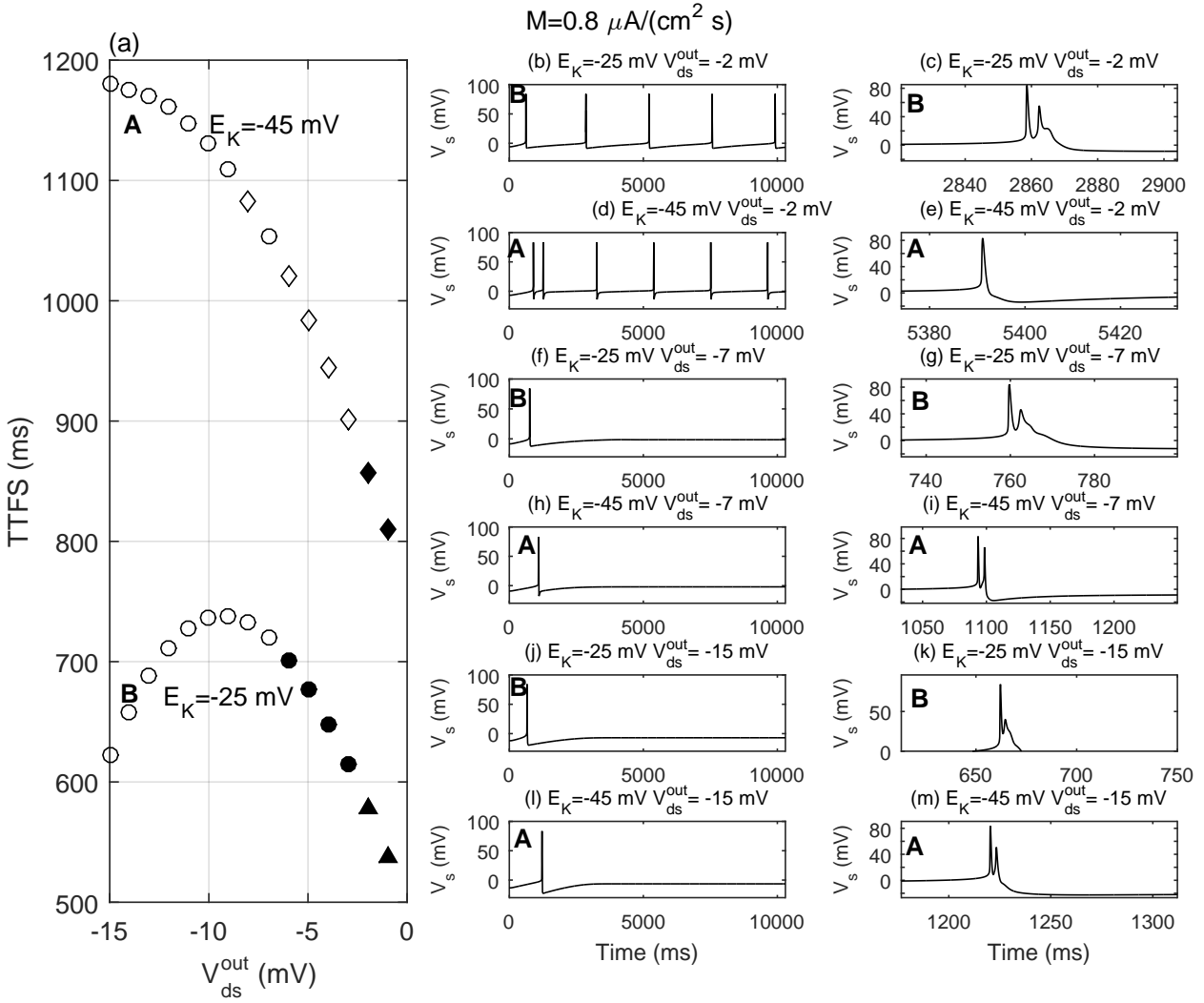


Figure 2.4: Spike behavior for two sublinear profiles, A and B. For both profiles  $M = 0.8\mu A/(cm^2 s)$ .  $E_K = -45$  mV for A and  $E_K = -25$  mV for B. All parameter values are the same as that used in Fig. 2.3 (a) and (b). Here, however, the integration is continued past the TTFS with a constant current injection =  $M \cdot TTFS$ . Filled symbols denote periodic spiking or bursting, and open symbols denote an isolated spike or burst, or that activity was at such a low frequency that no other spikes appeared during the 10 second runtime. Shapes symbolize number of spikes within a particular waveform (< 20ms): diamond denotes a single spike, circle denotes a spike doublet, and triangle denotes 3 or more spikes (e.g. a burst). The third column of plots is a magnification around a spike in the second column of plots.

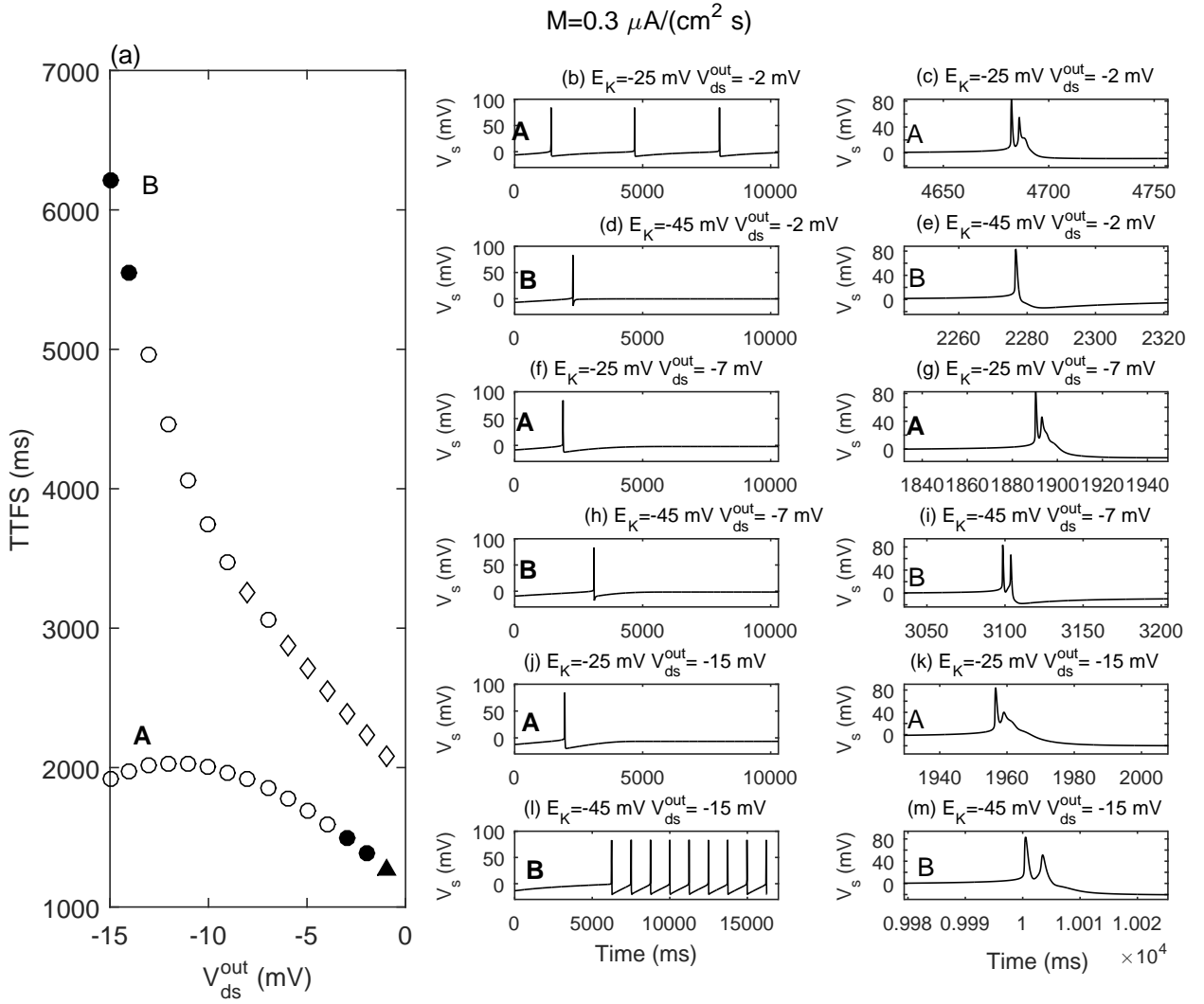


Figure 2.5: Spike behavior for a sublinear profile, A, and superlinear profile, B. Both profiles use a slow injection rate,  $M = 0.3\mu A/(cm^2 s)$ . For profile A  $E_K = -25$  mV and for profile B  $E_K = -45$  mV. All parameter values are the same as that used in Fig. 2.3 (a) and (b). Here, however, the integration is continued past the TTFS with a constant current injection =  $M \cdot TTFS$ . Filled symbols denote periodic spiking or bursting while open symbols are isolated spike or bursts or, at least, with a period greater than 10 s. Shapes symbolize number of spikes within a particular waveform (< 20ms): diamond denotes a single spike, circle denotes a spike doublet, and triangle denotes 3 or more spikes (e.g. a burst). The third column of plots is a magnification around a spike in the second column of plots. Notice how the superlinear profile exhibits isolated spikes at weak polarizations and periodic spiking near the end of the intermediate region. While the sublinear profile exhibits periodic spiking/bursting at weak polarizations and isolated spikes in the intermediate region. Superlinear and sublinear profiles show qualitative differences in both spike behavior and TTFS (see Fig. 2.6).

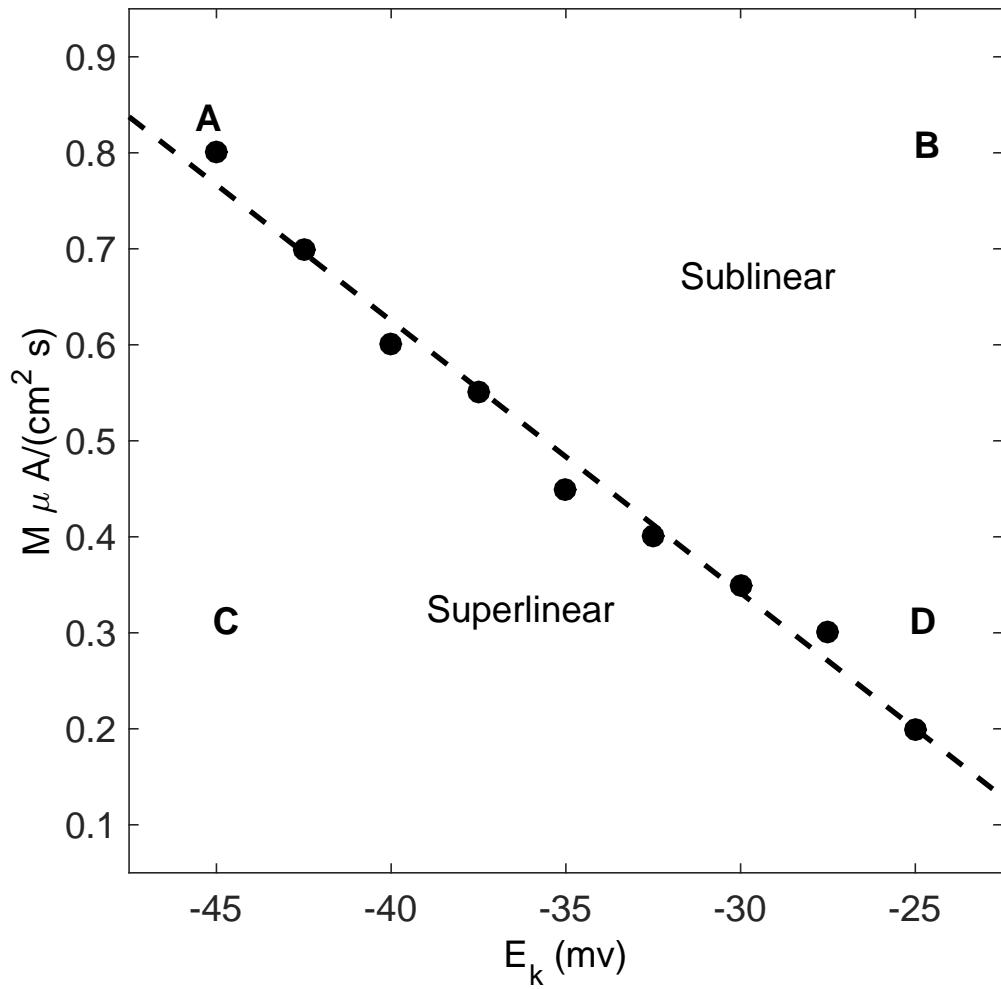


Figure 2.6: The  $E_K - M$  parameter-space boundary that separates sub- and super-linear behavior exhibits an inverse relationship. Below the line the profile is superlinear and above it is sublinear. As discussed in section 2.2.2 sublinear and superlinear profiles were associated with the sign of the numerical second-derivative computed over the intermediate polarization region,  $V_{ds}^{out} \in [-15mV, -4mV]$ . Parameter values are as in 2.3

begins to decrease with increasingly negative  $V_{ds}^{out}$ . A more complete view of this behavior is shown in Fig. 2.7, which shows the TTFS over a full range of stable polarizations for the

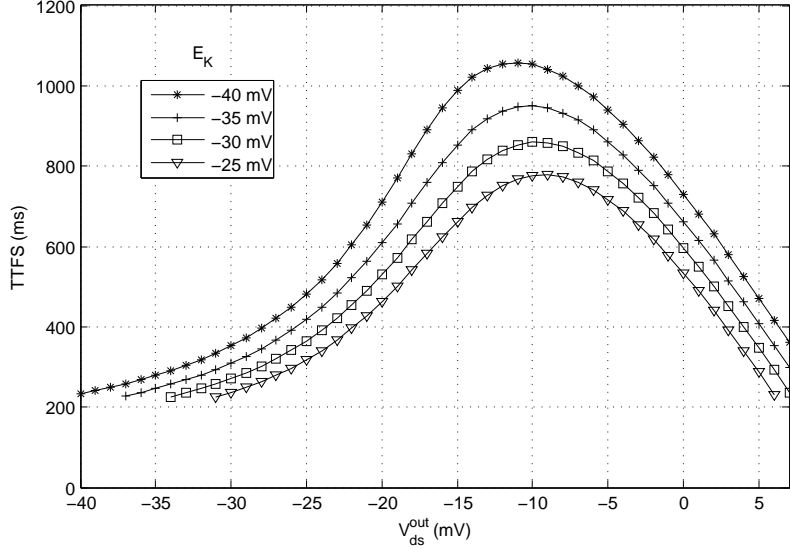


Figure 2.7: The strong polarization region begins where the TTFS starts to decrease as  $V_{ds}^{out}$  decreases. Here the TTFS values are calculated for a fast injection rate ( $M = 0.8\mu A/(cm^2 s)$ ) at four different  $E_K$ .

fast injection rate ( $M = 0.8\mu A/(cm^2 s)$ ). Even for the superlinear case the overall tendency is for the TTFS to decrease in the strong polarization region. For a superlinear profile the TTFS reaches several seconds or more in the strong polarization region. An interesting pattern emerges which includes sudden changes in TTFS (not shown). This complex profile occurs due to interactions of the very slow decay rate of the  $I_{K-AHP}$  and the ramp injection protocol. While interesting, these results might be difficult to replicate experimentally.

We define the polarization at which the TTFS begins to decrease with increasingly negative  $V_{ds}^{out}$  as the beginning of the strong polarization region. We then refer to the region between the weak and strong polarization as the intermediate region.

Figs. 2.3, 2.6, and 2.7 show how the polarization-dependent excitability varies over a

range of extracellular potassium and current injection rates. In summary, we categorize polarization as follows:

1. Weak polarization – in this region, the TTFS increases linearly with increasingly negative polarization (*i.e.* increasing somatic hyperpolarization). This corresponds to a  $V_{ds}^{out}$  ranging from about 10 mV to  $-4$  mV.
2. Intermediate polarization – In this region, the TTFS departs from its linear dependence on polarization. The TTFS increases either sublinearly or superlinearly with polarization, depending on the values of  $M$  and  $E_K$ .
3. Strong polarization – In this region, the TTFS decreases with increasingly negative polarization. The strong polarization region begins around a  $V_{ds}^{out}$  equal to about  $-15$  mV, but this onset depends on the chosen parameters.

We now take a closer look at the three regions, and most significantly, identify the mechanisms that give rise to the observed TTFS behavior in the intermediate and strong regions.

### 2.3.2 Weak polarization region

The TTFS behavior of our polarized PR model is linear at weak polarizations and is in agreement with experimental observations [13, 24, 25].

### 2.3.3 Intermediate polarization region

As  $V_{ds}^{out}$  becomes more negative, the resting potential of the dendrite becomes more depolarized. Starting from a more depolarized state, more of the dendritic channels are open, and the dendrite as a whole is primed for activity with the incoming soma current injection. We will show that the division of the solutions into either sublinear or superlinear profiles is due to the active currents in the dendrite. We note that  $I_{KAHP}$  and  $I_{KC}$  are functions of  $E_K$ , while  $I_{Ca}$  does not have any explicit dependence on  $E_K$ . In addition,  $M$  only affects the slow q-gating variable of  $I_{KAHP}$ . It is the modulation, through  $E_K$  and  $M$ , of the strength of the hyperpolarizing dendritic currents that is responsible for the occurrence of

sub- or superlinear TTFS profiles. The following observations and deductions lead us to this conclusion:

(1) Except for the strong polarization case, the soma was always found to spike before the dendrite.

(2) Prior to an action potential, the somatic and dendritic membrane potentials rise at the same rate in response to the soma-injected current ramp for all parameters tested in our numerical simulations. This is to be expected due to the high inter-compartment conductance,  $g_c$ , and rapid equilibration compared to the current injection rate. The membrane potentials continue to rise at the same rate until a spike occurs <sup>3</sup>. To show that indeed  $dV_s/dt \approx dV_d/dt$ , we examined the right-hand side of  $dV_s/dt$  and  $dV_d/dt$  for various values of  $E_K$ ,  $M$ , and  $V_{ds}^{out}$ . We found that the total somatic and dendritic currents are indistinguishable for even the fastest ramp we explored,  $M = 0.9 \mu A/(cm^2 s)$  (see Fig.2.8).

(3) Significantly more current is shunted away from the soma and into the dendrite for the superlinear case compared to the sublinear case. This is shown in Fig. 2.9. It might be inferred that the increase in the shunting current in the superlinear cases is due to an increase in hyperpolarizing outward dendritic current. Support for this assertion can be found by plotting the total active dendritic current for the sublinear and superlinear cases, respectively. Fig. 2.10 shows how differently the active dendritic currents of a sublinear and superlinear profile vary with time and over a range of intermediate polarizations. For the sublinear cases, the active dendritic currents monotonically increase and result in a net depolarizing effect over the range of intermediate polarization. However, for the superlinear case, the active dendritic currents depolarize very slowly from  $-10mV$  to  $-12mV$  and become non-monotonic, eventually resulting in a net hyperpolarizing effect at negative polarization values below -13 mv.

(4) The effect that polarization has on the rate at which the soma depolarizes can be analyzed by examining the active and total dendritic currents (since  $dV_s/dt \approx dV_d/dt$ ). At

---

<sup>3</sup>The rate of change of the somatic and dendritic membrane potentials are appreciably different only in a 1-2 millisecond period after the TTFS and during an action potential.

intermediate polarization (Fig. 2.11) we see that the total dendritic current is significantly reduced for the superlinear case and delays the TTFS as compared to the sublinear case. In contrast, at weak polarization, when the voltage-activated gating variables are minimal and have yet to begin their rapid ascent we see in Figure (Fig. 2.12) that the sublinear and superlinear cases do not exhibit such qualitative differences in their dendritic currents.

(5) Finally, we note that the division of the  $E_K - M$  parameter space into sublinear and superlinear profiles corresponds to a separation into stronger and weaker dendritic hyperpolarizing currents. The effect of lowering the potassium reversal potential  $E_K$  can be understood by examining the equations for the polarized PR neuron (Eqs. 3.3, 3.4, 3.5) and noting that for all potassium currents in both the dendrite and the soma, a more negative  $E_K$  corresponds to a stronger drive for positive current to flow out of the compartments. The role of  $M$  is made clear by examination of the gating kinetics. We plotted the gating variables during our ramp-stimulation protocol over a range of  $M$  and we see that  $M$  only affects the very slow q-gating variable of the  $I_{K-AHP}$  current (Fig. 2.13). With a lower  $M$ , the slow equilibrating q-gating variable has more time to reach its equilibrium value. Since  $q$  is monotonically increasing with  $V_d$ , and  $V_d$  is always increasing during the ramp somatic current injection (at least for the range of parameters we examined),  $q$  will always be in the process of equilibration to a higher value. Thus the lower  $M$  is, the greater  $q$  gets, and the greater the hyperpolarizing  $I_{K-AHP}$  current will become.

In summary: As polarization becomes increasingly negative, the dendritic calcium currents increasingly depolarize the dendrite. Simultaneously, the dendritic potassium currents increasingly hyperpolarize it. Thus, these currents have competing effects: one works to excite, the other to inhibit. If the calcium current dominates, then we observe a sublinear response, and if the potassium current dominates, we observe a superlinear response.

### 2.3.4 Strong polarization region

The mechanism behind the decrease in the TTFS (as  $V_{ds}^{out}$  decreases) at strong polarizations is revealed by examining the shunting current from the soma to the dendrite. Fig. 2.14

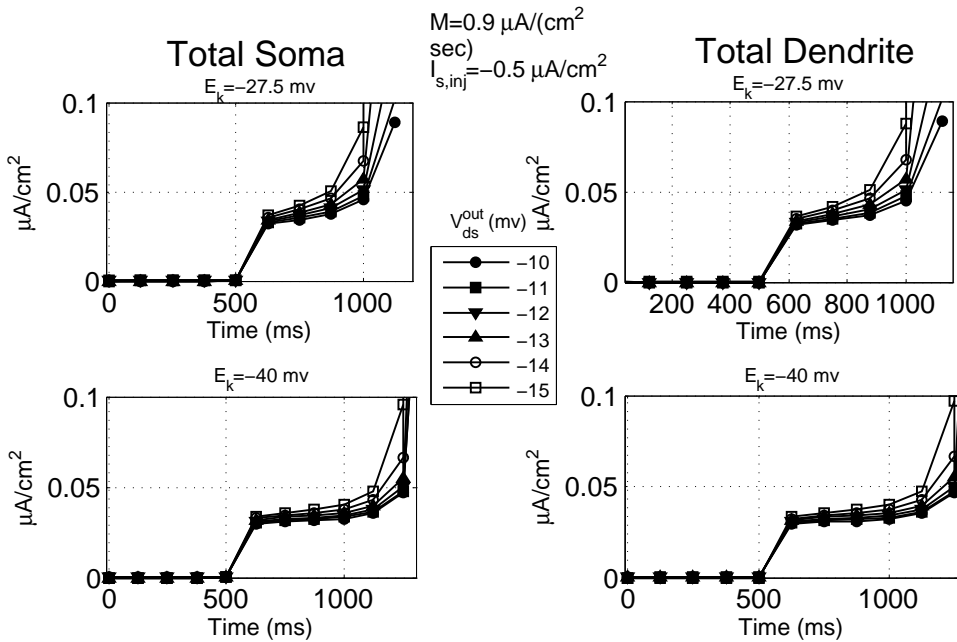


Figure 2.8: Here we plot the total somatic and dendritic currents, the right-hand sides of  $dV_s/dt$  and  $dV_d/dt$ . Even at the fastest injection rates the somatic and dendritic potentials change at the same rate. This holds true during the soma injected current for all  $E_K$ ,  $M$ , and  $V_{ds}^{out}$  we examined.

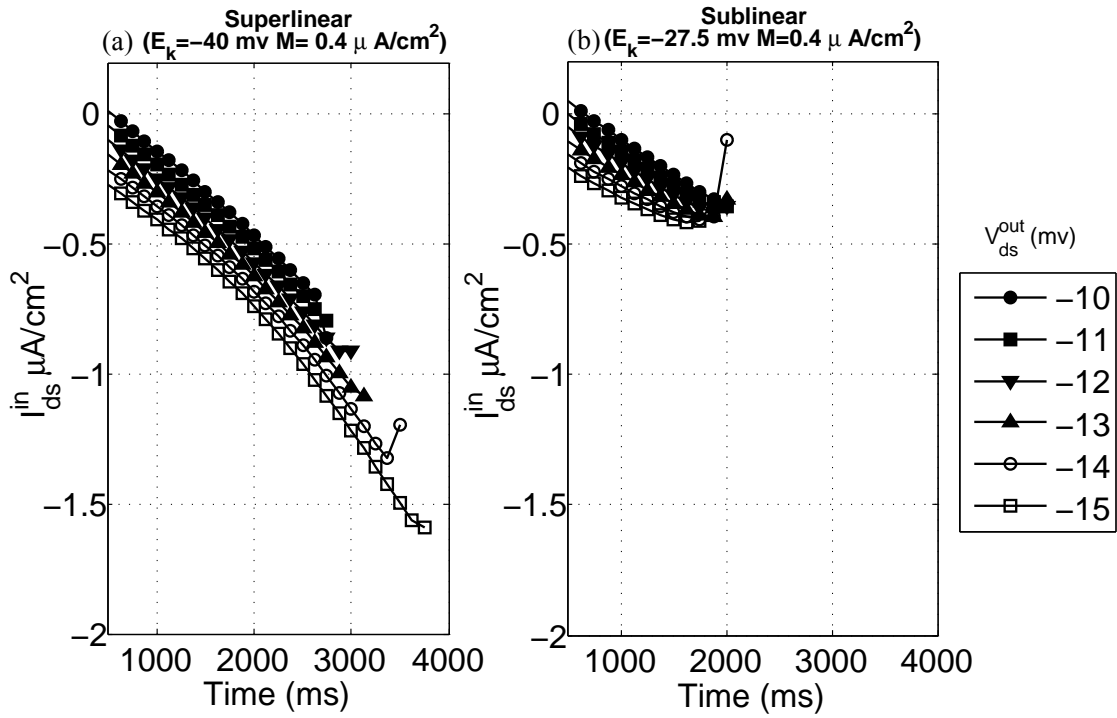


Figure 2.9: Soma shunting to dendrite.  $M = 0.4 \mu A/cm^2$ .  $I_{ds}^{in}$  is defined to be the current out of the dendrite and into the soma. Thus, negative values of  $I_{ds}^{in}$  indicate that this current flows from the soma to the dendrite. The curves terminate when a somatic membrane potential spike occurs. Compared to the sublinear case the superlinear shunting is increased by approximately 20 percent. This increase in shunting is enough to not only delay a somatic spike, but to cause significant dendritic hyperpolarization. For the case shown, the TTFS increases by approximately 30 % for  $V_{ds}^{out} = -10$  mV to a factor of two for  $V_{ds}^{out} = -15$  mV.

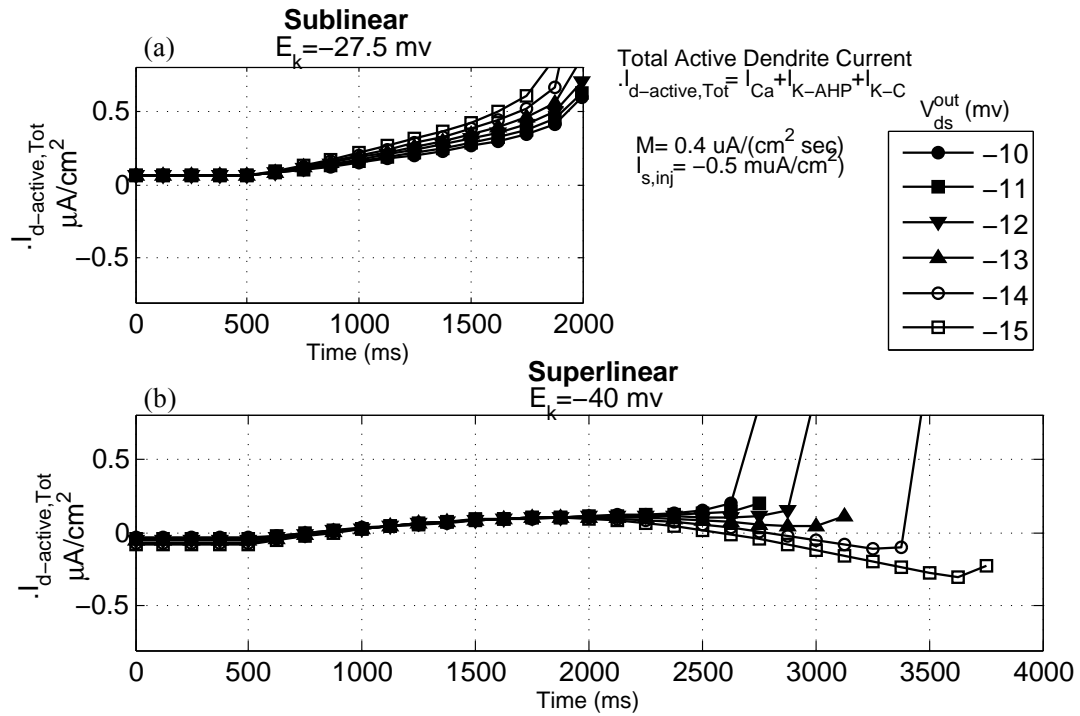


Figure 2.10: The active dendritic currents for sublinear and superlinear profiles. Here  $M = 0.4\mu A/cm^2 s$  and  $I_{s,inj} = -0.5\mu A/cm^2$ . In (a)  $E_K = -27.5$  mV and the profile is sublinear. In (b)  $E_K = -40$  mV and profile is superlinear. The total active dendritic currents are plotted and are equal to the sum of the hyperpolarizing potassium currents, K-AHP and K-C, as well as the depolarizing calcium.  $I_{d,active} = I_{K-AHP} + I_{K-C} + I_{Ca}$ . For the sublinear profile the total active dendritic currents are monotonic in time and for increasingly negative  $V_{ds}^{out}$ . For the superlinear profile with it's stronger hyperpolarizing currents the total active dendrite currents become non-monotonic with time for polarization below around  $-12$  mV. Furthermore for polarizations below around  $-13$  mV the total active dendritic currents become net hyperpolarizing.

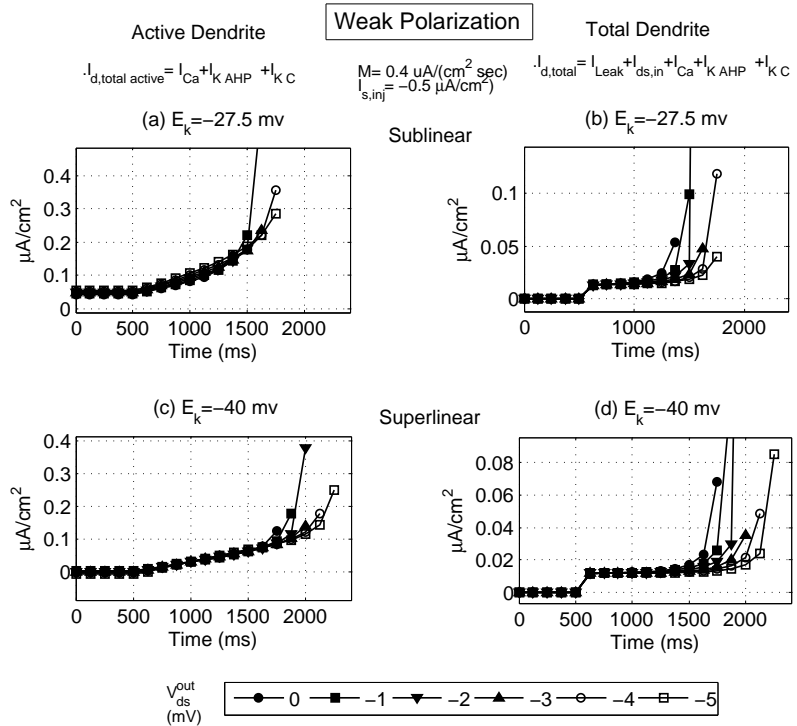


Figure 2.11: Plots of the active dendritic membrane currents (left), and for comparison, the total dendritic membrane current (right). The parameters are the same as in Figure 10.

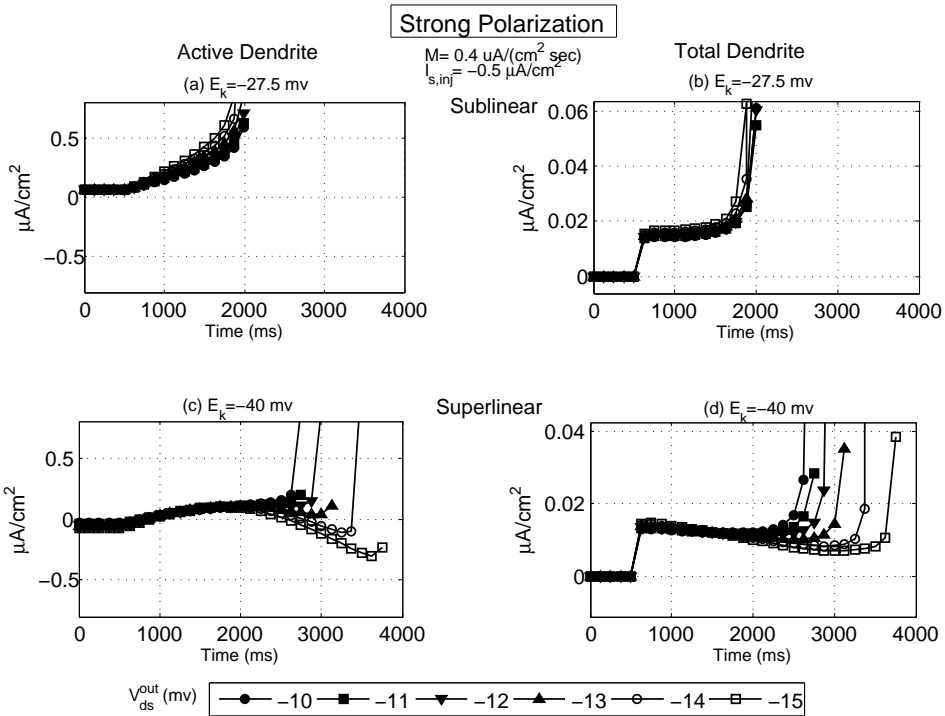


Figure 2.12: The superlinear and sublinear profiles emerge only at stronger polarizations which primes the activation of the dendritic channels. For the same parameters as in Fig. 2.11 but at weak polarizations while there is some increase in the hyperpolarization and longer TTFS there is no qualitative difference in the currents as there is when it is at stronger negative polarizations.

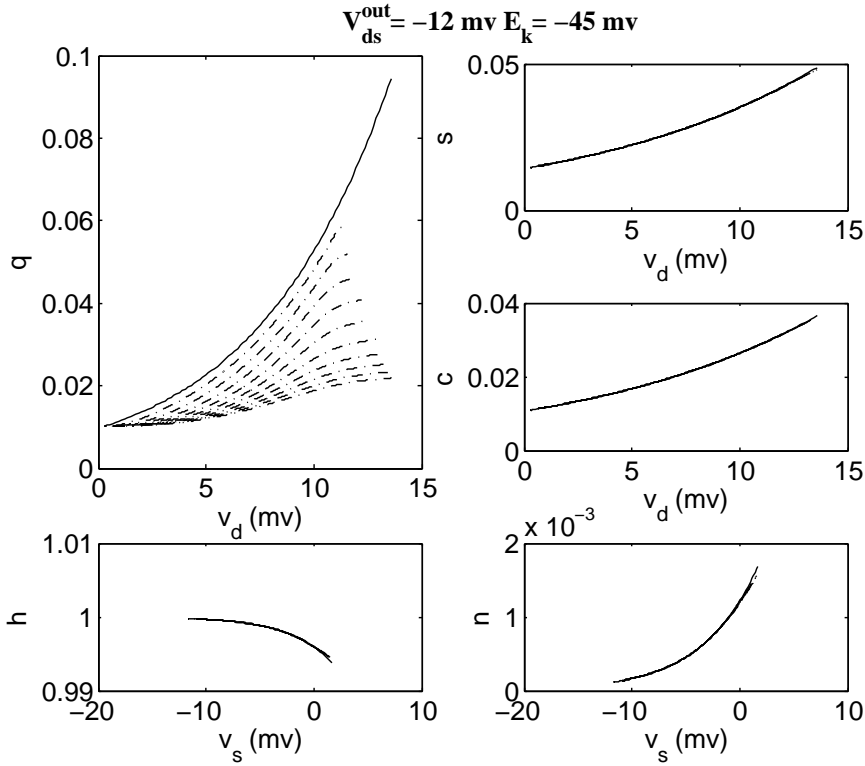


Figure 2.13: The  $q$  gating variable is the only gating variable sensitive to  $M$  over the range considered here. The five gating variables of the polarized PR neuron are shown as the neuron is taken from rest to a somatic potential spike in response to a range of injected ramp currents. In each case  $V_{ds}^{out} = -12 \text{ mV}$  and  $E_k = -45 \text{ mV}$ . For each plot, the equilibrium value is denoted by a solid line, and the computational results are denoted by dashed lines. There are ten different dashed lines corresponding to  $M$  from  $0.1 \mu\text{A}/(\text{cm}^2\text{s})$  to  $1.0 \mu\text{A}/(\text{cm}^2\text{s})$ . Only the slowly-activating  $q$  gating variable exhibits significant deviation from the equilibrium curve. In all other plots, the gating variables track the equilibrium curve so closely, regardless of the injection rate, that the lines can barely be distinguished. Note that although  $q$  is a function of  $Ca$  the fact that  $Ca$  equilibrates with changing  $V_d$  well over an order of magnitude faster than  $q$  equilibrates with changes in  $Ca$  allows us to approximate the  $q$  kinetics  $q(Ca(V_d))$  by  $q(Ca_\infty(V_d))$ .

plots this shunting current,  $I_{ds}^{in}$ , with negative values indicating positive charge flowing

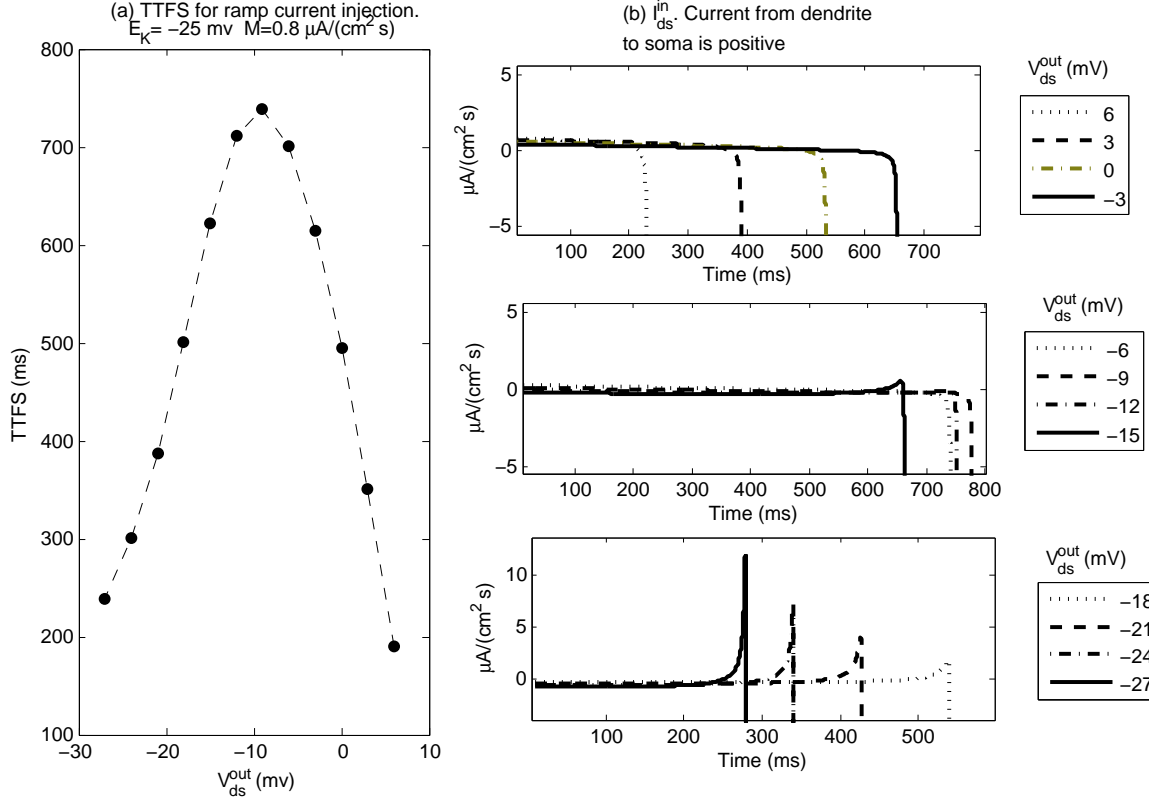


Figure 2.14: In the strong polarization region, where TTFS decreases, a dendritic spike precedes the somatic potential spike. Somatic and dendritic potential spikes are revealed when plotting  $I_{ds}^{in}$ . Plots of the current flow between compartments,  $g_c(V_d - V_s + V_{ds}^{out})$  are shown in (b) for the corresponding  $V_{ds}^{out}$  shown in (a). Spikes in  $V_d$  result in positive current spikes in (b) while spikes in  $V_s$  result in negative current spikes in (b). Since for each polarization the applied current ramp grows until the somatic potential spike in all cases the  $I_{ds}^{in}$  ends with a negative spike. The appearance of dendritic spikes (positive  $I_{ds}^{in}$ ) coincides with the decreasing TTFS. Evidently the increase in depolarizing current coming from the dendrite back into the soma more than compensates for the increased soma-hyperpolarizing  $V_{ds}^{out}$ .

from the soma to the dendrite and positive values indicating the reverse. Since in all cases the stimulus ends when the soma spikes, all the curves end with a sharp negative drop. However, corresponding to the strong polarization values at which the TTFS begins to decrease, positive deflections in  $I_{ds}^{in}$  are seen in increasing magnitude (see the two right lower panels in Fig. 2.14). These positive deflections result from dendritic spikes back-propagating into the soma. These then act as a depolarizing trigger which induces a soma

spike.  $I_{Ca}$  is the only active depolarizing dendritic current, and it is this current that is responsible for the dendritic potential spikes and subsequent decrease in the TTFS.

### 2.3.5 Effects of Morphology On Excitability

We have used only one value for  $g_c$  ( $2.1 \text{ mS/cm}^2$ ) and one for  $\rho$  (0.5) in our simulations so far. These values were used as standard values in [4]. Biological pyramidal neurons are most likely not so electro-tonically “close”, and the dendritic and somatic areas may vary substantially. To gauge the sensitivity of our results to variation of these morphological parameters, we systematically varied  $g_c$  and  $\rho$  for the ramp injection protocol. Results are shown in Figs. 2.15 and 2.16 respectively. To understand how  $g_c$  effects the TTFS in Fig. 2.15 it helps to think of the path of the injected soma current: (1) out of the soma through the membrane (i.e., leak) (2) into the dendrite, and (3) from the dendrite out through the dendritic membrane. We can neglect (1) since the leak current is small compared to the inter-compartment conductance and the membrane currents. For very small  $g_c$  (see circles and squares in Fig. 2.15 (a-d)) the linearity of the TTFS as a function of  $V_{ds}^{out}$  can be explained by the inter-compartment current,  $I_{ds} = g_c(V_d - V_s + V_{ds}^{out})$ , becoming dominant. For moderate and higher levels of  $g_c$ , the current leaving through the dendrite via the nonlinear active dendritic membrane currents play an increasing role as we go through the intermediate and strong polarization regions. In this case, the calcium and hyperpolarizing potassium currents become increasingly active, and the TTFS profiles display the same qualitative shapes we saw earlier for  $g_c = 2.1 \text{ mS/cm}^2$  (Fig. 2.3).

Fig. 2.16 shows how varying the proportion of total membrane area allocated to the soma,  $\rho$ , affects the TTFS as a function of  $V_{ds}^{out}$ . The qualitative features of the TTFS profiles are consistent with the profile for  $\rho = 0.5$ . Because of the mismatch in load at  $\rho = 0.9$  (stars in (a-d)), more of the current remains in the soma, and it is the linear dependence of  $I_{ds}$  on  $V_{ds}^{out}$  that contributes to a more linear TTFS profile. As  $\rho \rightarrow 0$ , the current flows increasingly into the dendrite where the nonlinear dendritic membrane

currents affect the TTFS.

### 2.3.6 Polarization-dependent Excitability Using Synaptic AMPA

The preceding results were based on the use of an injected ramp current, delivered at various rates, primarily to facilitate comparison with experiments. The ramp injected current is a commonly-used protocol for characterizing neural excitability. However, it is also of interest to examine how polarized neurons respond to synaptic inputs.

Accordingly, we replaced the ramp current injection with synaptic AMPA currents in the dendritic compartment using the same synaptic model for AMPA as in Pinsky and Rinzel (1994) and Park et al. (2003, 2005). In the intermediate region, the shape of somatic spikes change somewhat with increasing polarization, as was shown in Figs. 4 and 5. Thus, we would expect polarization-dependent effects on the synaptic current based on the model described above. However, to facilitate the following analysis, we fix the pre-synaptic activity to consist of a single spike such that  $V_{s,pre}$  is above 20 mV for 1.2 ms.

The main difference between this approach and the ramp current protocol is that in the synaptic input case, a failure to spike is an important possible outcome. This is illustrated in Fig. 2.17, using  $g_{AMPA} = 0.3 \text{ mS/cm}^2$  and  $I_{s,inj} = 0.5\mu\text{A/cm}^2$ . Panel (a) shows the TTFS versus  $V_{ds}^{out}$  profiles for two cases (with parameters  $E_K$  and  $g_{KAHP}$ ) in which the curve terminates because the neuron fails to spike. The same panel shows two other cases in which the TTFS profile could be obtained throughout the range of  $V_{ds}^{out}$  studied.

Panel (b) shows the maximum TTFS obtained over  $V_{ds}^{out} \in [-12, 0] \text{ mV}$ , as a function of  $g_{KAHP}$  and  $E_K$ , noting the cases in which the neuron fails to spike somewhere in the  $V_{ds}^{out}$  range. Polarization values were stepped by 0.075 mV. We find a clear division of this parameter space into a region corresponding to spike failure, and a region for which spikes occur throughout the  $V_{ds}^{out}$  range and a value of the maximum TTFS can be obtained. The values of  $g_{KAHP}$  at the boundary increase with increasing  $E_K$ , as the increased excitability due to extracellular potassium is somewhat balanced by an increase in hyperpolarizing  $K_{AHP}$  conductance.

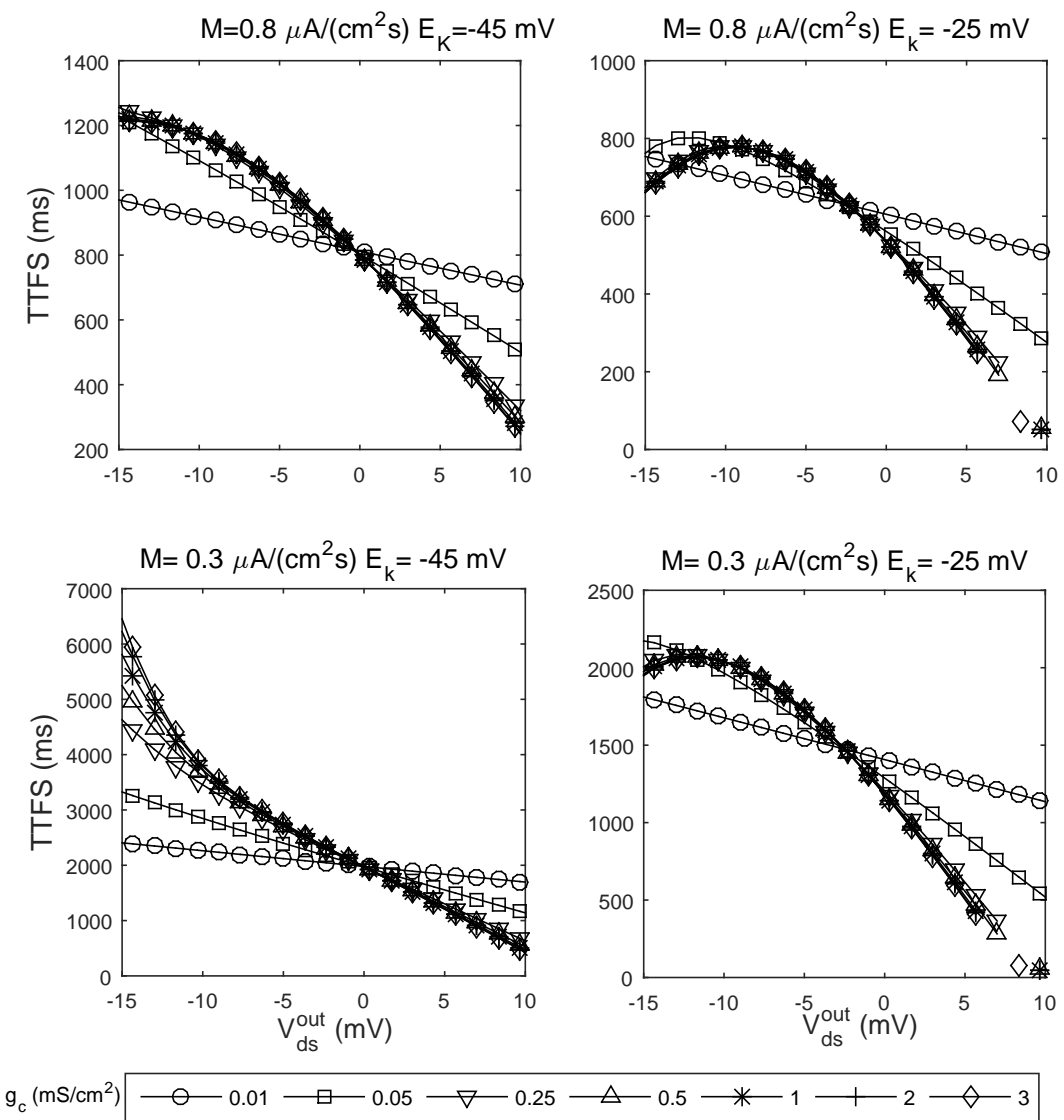


Figure 2.15: TTFS profiles for various values of  $g_c$ , the electrotonic coupling between the soma and the dendrite.

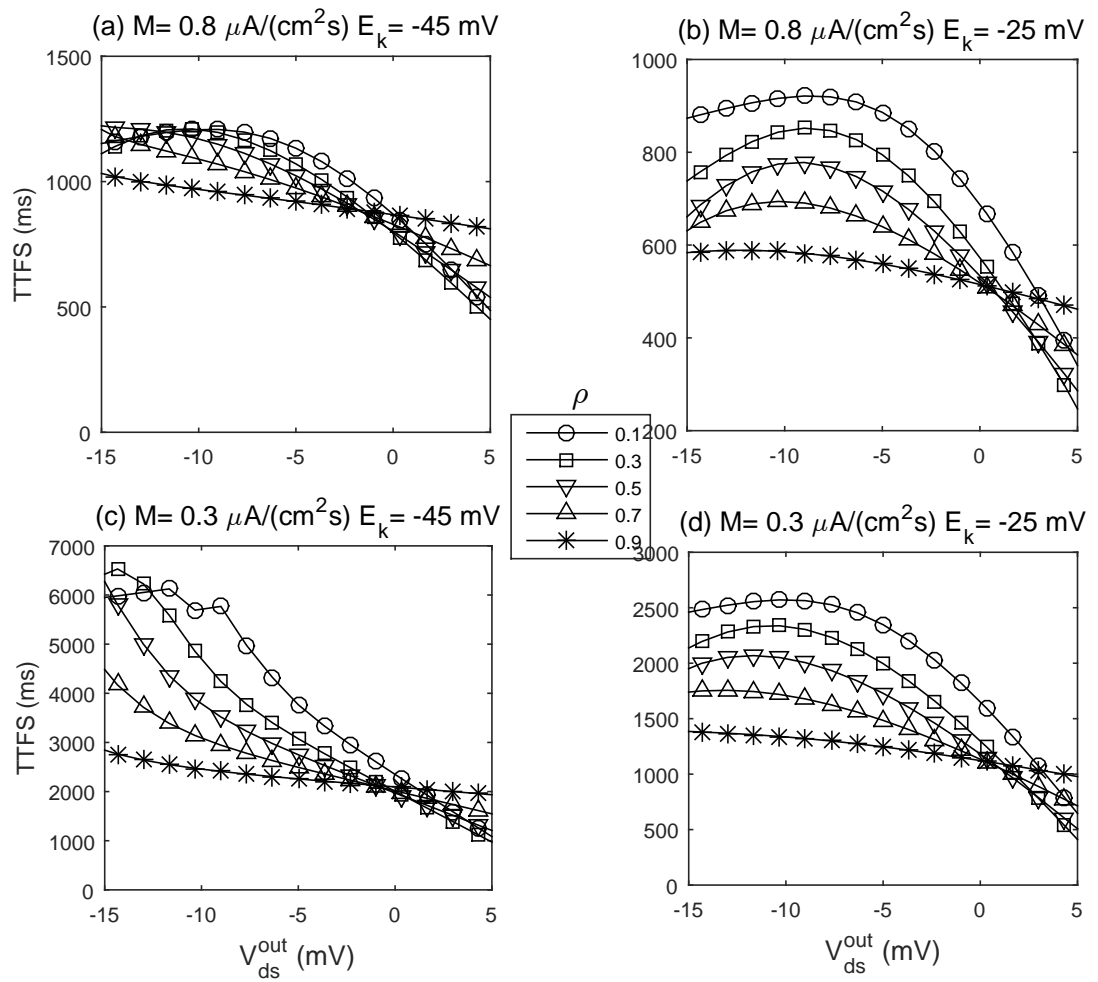


Figure 2.16: The proportion of the total membrane area allocated to the soma compartment,  $\rho$ , is varied over a range from 0.1 to 0.9.

In Fig. 2.18, we see that the segregation of cases that fail to spike and those that do spike is correlated with a qualitative change in the total active dendritic currents. The sets of  $E_K$  and  $g_{KAHP}$  values in (a)-(d) are the same as in Fig. 2.17 (a). For the two cases without spike failure (panels (a) and (b)), the total active dendritic current grows linearly and at nearly the same rate roughly independently of the polarization. In contrast, for the two cases with spike failure (panels (c) and (d)), the total active dendritic current after about 10 ms grows at a much slower rate and shows more pronounced polarization dependence. These observations are consistent with our previous observations using the ramp current protocol regarding the role of the active dendritic currents. In particular, neurons that were superlinear for the ramp protocol and those that failed to spike for the AMPA protocol were associated with similar total active dendritic currents. Namely, the total active dendritic currents are significantly suppressed, polarization-dependent, and were modulated by the potassium-dependent hyperpolarization currents.

### 2.3.7 Inclusion of $I_h$ current.

The concentration of  $I_h$  channels is many times higher in the dendritic portion of pyramidal cells than in the somatic region [46]. We therefore equip our existing polarized PR model with an  $I_h$  current in the dendritic compartment. The  $I_h$  current is activated at hyperpolarizing potentials, is active at rest, has moderately long time constants, and can obtain various regulated states. These regulated states are simulated by adopting various values of the maximal conductance  $g_h$  and the channel half-activation voltage  $V_{i-half}$ . The equations and parameters are given in the Methods section.

In the following computations, except for the inclusion of the  $I_h$  current, all other parameters and currents remain the same as in previous ramp-injected and AMPA-injected computations. First, we show how the resting membrane potentials change with the inclusion of  $I_h$  at different levels of regulation. Fig. 2.19 depicts the somatic and dendritic potential and the  $I_h$  gating variable  $i$  ((a)-(c) respectively) as a function of  $V_{ds}^{out}$ . The changes in resting membrane potential coincide with the activation of  $i$  at hyperpolarized

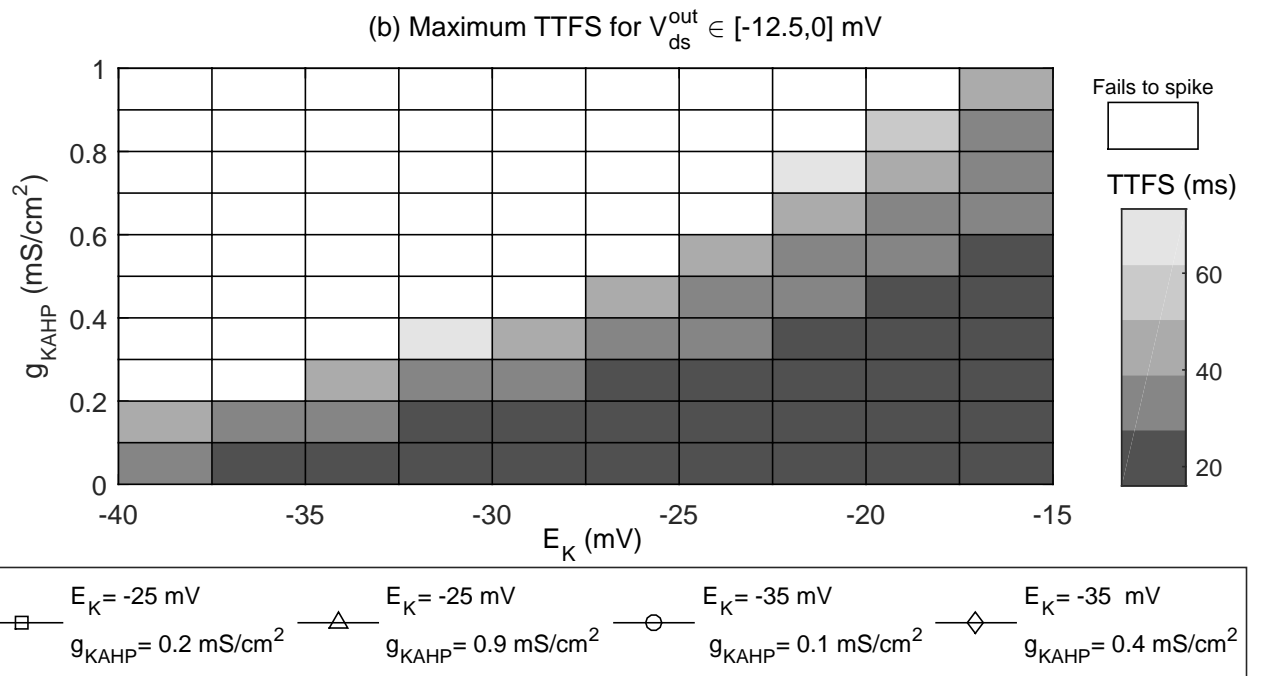
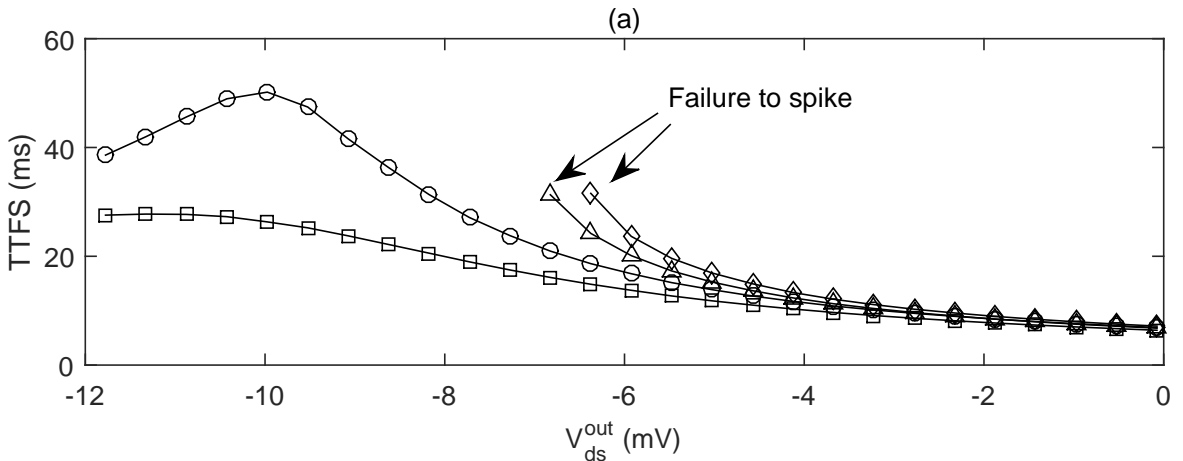


Figure 2.17: For our synaptic AMPA protocol ( $g_{AMPA} = 0.3 \text{ mS/cm}^2$ ) we find a clear split in the  $g_{KAHP} - E_K$  parameter space into neurons that fail to spike at some point in the intermediate range and those that have a spiking solution into the strong polarization region. In (a) we have plotted the maximum TTFS obtained in the intermediate polarization region, which we defined as  $V_{ds}^{out} \in [-12.5, 0] \text{ mV}$  since this encompassed all of the polarization values capable of producing a maximum TTFS. Polarization values were stepped by 0.075 mV. In (b) we plot the TTFS profiles for four sets of  $E_K - g_{KAHP}$  values. Two of them are in the "Fail to spike" region in (a) (white) and two are in the shaded region indicating that they spike throughout the intermediate region and into the strong region. The line marked with circles ( $E_K = -35 \text{ mV}$  and  $g_{KAHP} = 0.1 \text{ ms/cm}^2$ ) is close to the boundary and reaches a maximum at around  $-10 \text{ mV}$  at which point by our definition it reaches the end of the intermediate region and the beginning of the strong region.

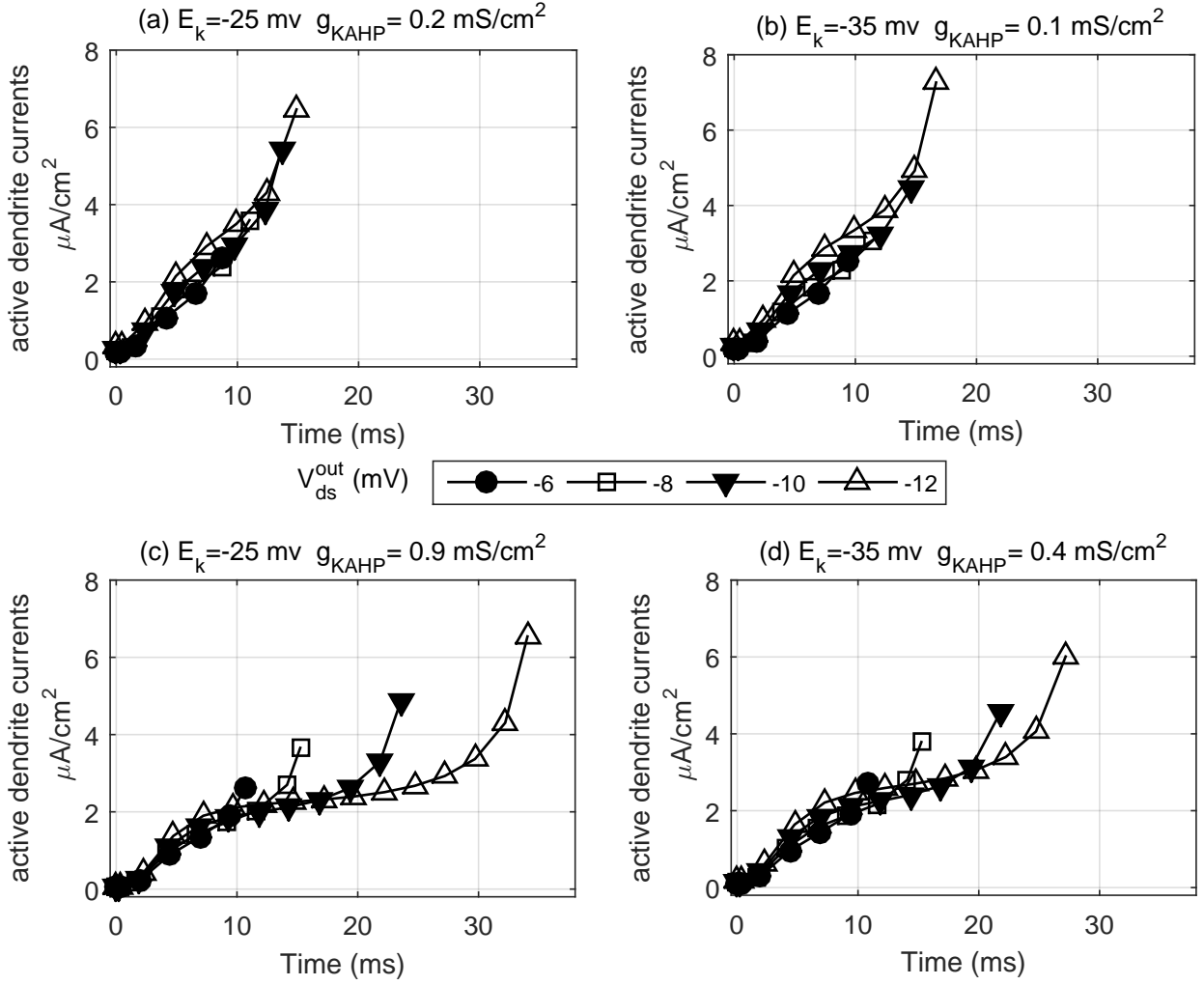


Figure 2.18: For the AMPA current protocol, the neurons that fail to spike in the intermediate region and those that do is correlated with a qualitative change in the total active dendritic current. The sets of  $E_K - g_{KAHP}$  values in (a)-(d) are the same as in Fig. 2.17 (b). For the two neurons that spike throughout the intermediate region, (a) and (b), The total active dendritic current grows linearly and at nearly the same rate regardless of the polarization. In contrast, for the two neurons that failed to spike the total active dendritic current, after about 10 ms, grows at a much slower rate and shows more pronounced polarization dependence. These observations are consistent with our observations and hypothesis made using the ramp injected protocol about the role of the active dendrite currents. One difference between the ramp injected protocol and the AMPA protocol is that for the ramp injected protocol the total active dendritic current become net hyperpolarizing in the superlinear case (Fig. 2.10 and Fig. 2.12).

values of  $V_d$  occurring at more positive  $V_{ds}^{out}$ . The effect is greater at more up-regulated states when  $g_h$  and  $V_{i-half}$  are increased. We next examine how the various regulated states of the  $I_h$  current affect our ramp-injected protocol results. In Fig. 2.20 we performed computations analogous to those of Fig. 2.3 depicting the polarization-dependent TTFS for high and low  $E_K$  and for fast and slow  $M$ . The results are qualitatively similar to those in Fig. 2.3, which had no  $I_h$  currents. The small differences between the polarized PR without  $I_h$  (square) and with  $I_h$  (circle, triangle, star) are most apparent for larger  $V_{ds}^{out}$ , corresponding to more hyperpolarized dendritic membrane potentials. Also apparent is the significant gap between what has been treated as the high-level up-regulated state from serotonergic studies [1] (circle) and the most active state used in [2] (star).

In Fig. 2.21, the AMPA protocol is used as in Fig. 2.17. We compare the polarized PR neuron without  $I_h$  (a) to the polarized PR neuron with  $I_h$  at two up-regulated levels (b) and (c). The clear split in the  $g_{KAHP}-E_K$  plane into those neurons that have a spiking solution throughout the intermediate region and those that fail at some intermediate polarization is present both without  $I_h$  (a) and with  $I_h$  currents at both the control state (b) and the extreme activation range used in [2] (c). In (b) and (c) the depolarizing effect of  $I_h$  is apparent in the diminishing area of spike failure and the decreasing TTFS.

## 2.4 Discussion

There is experimental evidence of a weak polarization region where the excitability decreases linearly with increasing soma-hyperpolarizing polarization [13, 24, 25]. In addition, a strong polarization region has been found where the excitability increases with stronger soma-hyperpolarizing polarization [13]. We are unaware of any theoretical or experimental work exploring excitability at intermediate polarizations. Our results provide experimentally-testable predictions of how neuronal excitability is affected by polarization. The boundaries of the polarization regions and the  $E_K - M$  bifurcation values will undoubtedly vary from neuron to neuron, reflecting variations in their density of channels and even changes in

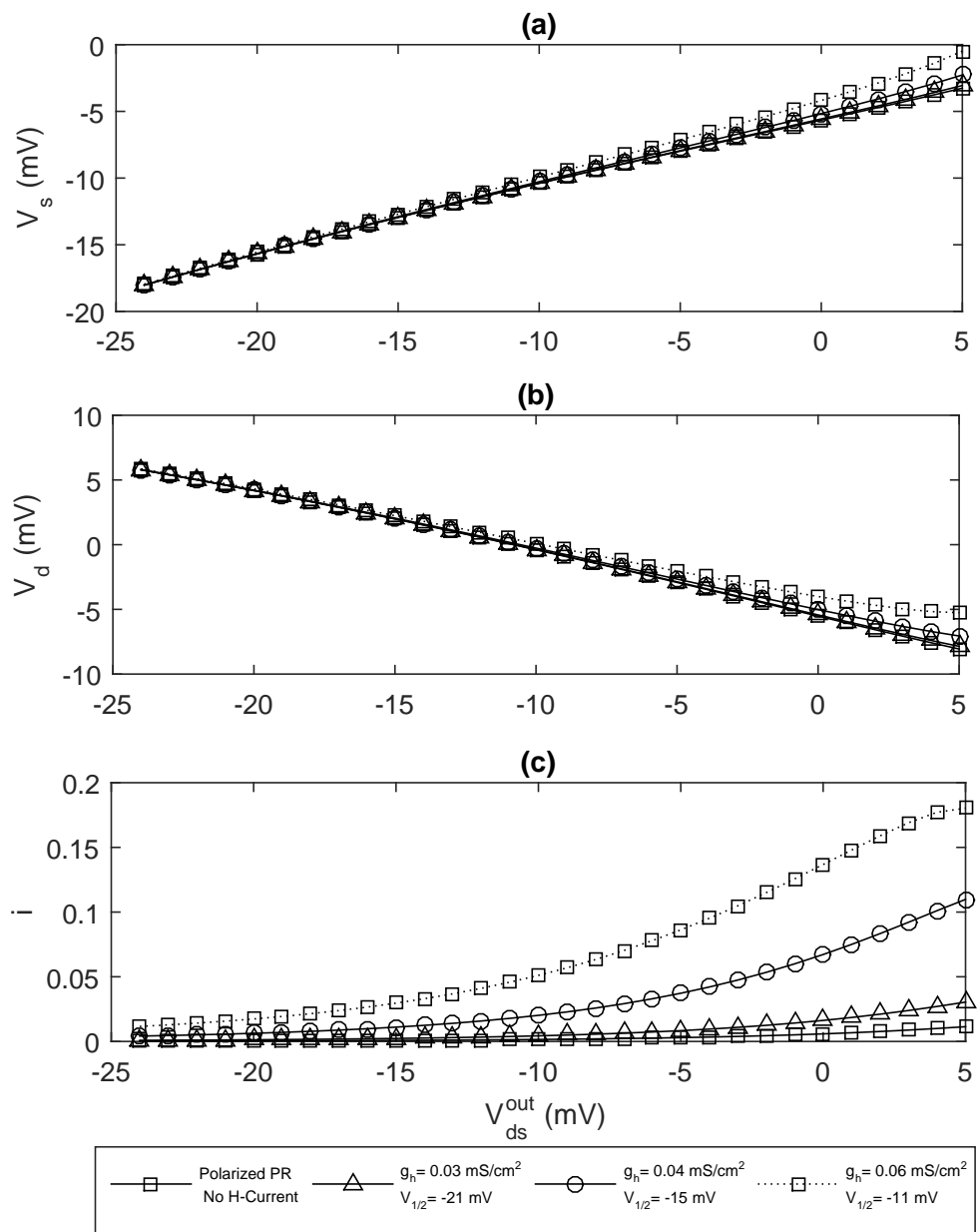


Figure 2.19: This figure shows  $V_{ds}^{out}$  versus  $V_s$ ,  $V_d$ , and  $i$  for the resting state (a)-(c) respectively.

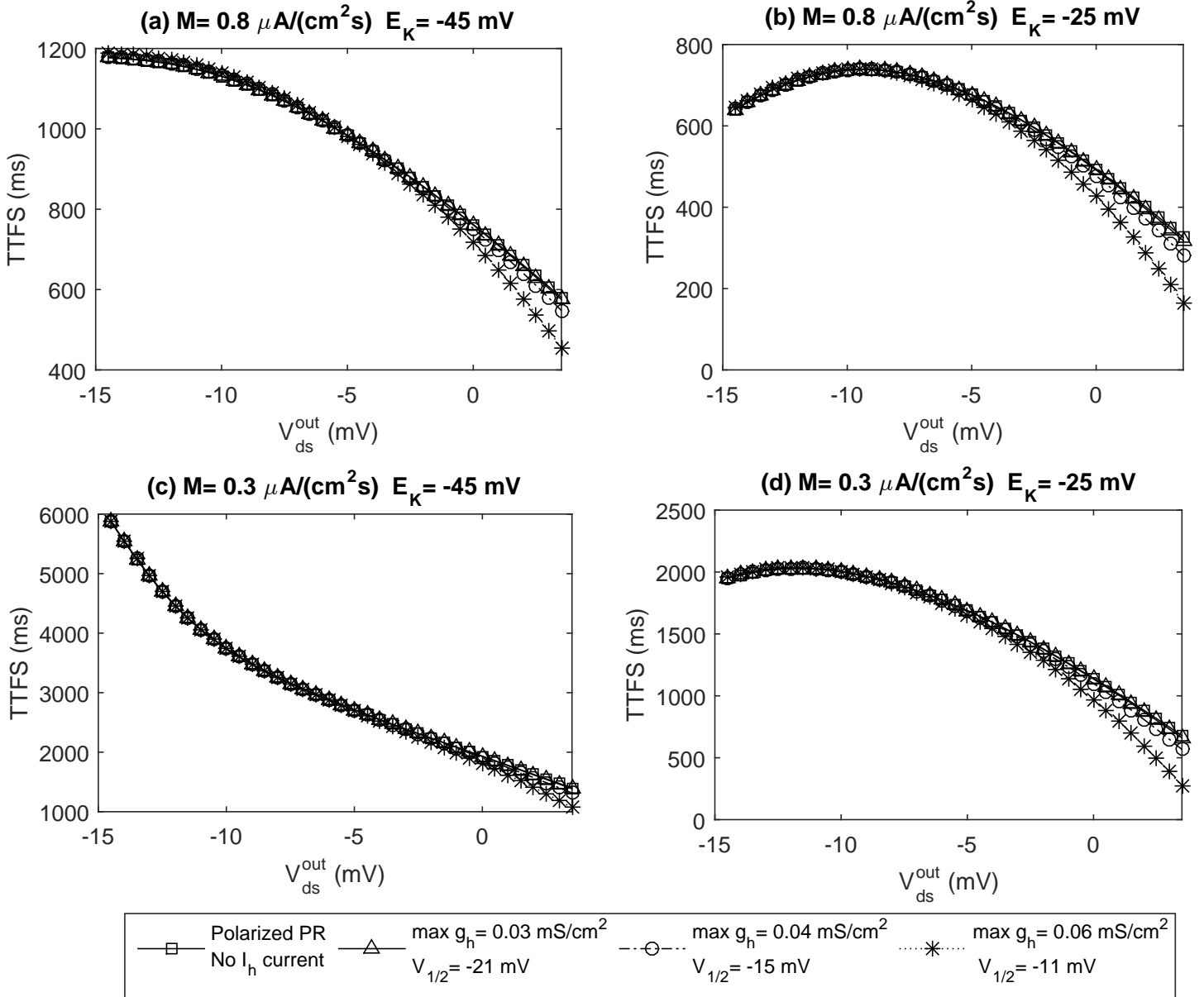


Figure 2.20: The ramp injected protocol with polarized PR model plus  $I_h$  current. The differences between the polarized PR without  $I_h$  (square) and the different regulated states of  $I_h$  (triangle, circle, star) are most apparent at larger  $V_{ds}^{out}$  and at more hyperpolarized dendritic membrane potentials. Also apparent is the significant gap between what has been treated as the high up-regulated state from serotonergic studies [1] (circle) and the most active state used in [2] (star).

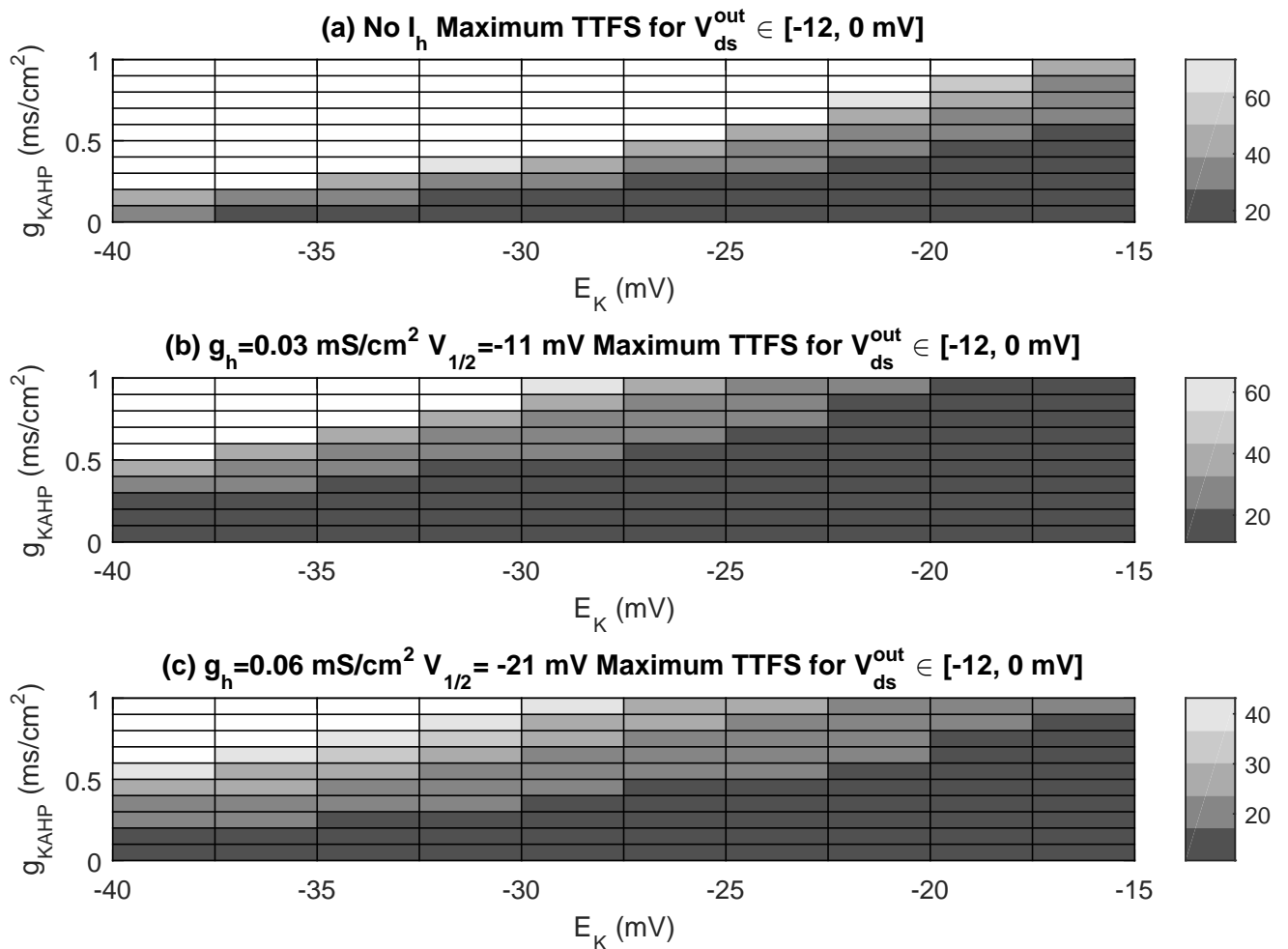


Figure 2.21: TTFS for different levels of  $I_h$ , where darker is faster spiking and white denotes spike failure. The spike failure profile persists with added  $I_h$ , but the depolarizing effect of  $I_h$  causes quicker TTFS and decreases the size of the spike failure region.

their activation potentials. However, the qualitative structure of polarization-dependent excitability that we have shown might well serve as an initial working hypothesis.

Several consequences follow from our results. First, once outside the weak polarization region, efforts to control the dynamics of a neuron or a network of neurons may depend critically on whether the neuron(s) has (have) a sublinear or superlinear TTFS sensitivity to polarization. In particular, the ability of  $[K^+]_o$  to drive the neuron to and from a sublinear and superlinear dependence on polarization might suggest that the extracellular potassium and its dynamics may need to be considered when trying to modulate neural activity with electric fields. As we have mentioned, neural hyperactivity has been shown to lead to an increase in  $[K^+]_o$ , thus increasing  $E_K$  [26, 47, 48] which in turn further increases neural excitability. The neural activity and extracellular potassium levels by themselves form a positive feedback loop. However, application of increasingly soma-hyperpolarizing fields will, in the intermediate and strong regions, decrease excitability. The decreased excitability would be expected to decrease  $[K^+]_o$  and hence decrease the polarization-dependent excitability induced by soma-hyperpolarizing fields, thus resulting in a negative feedback loop. Further still, if the decrease in  $[K^+]_o$  is sufficient to draw neurons from a sublinear to superlinear profile, then we might expect to see a sudden step-down in excitability and a qualitative change in the rate at which excitability is decreased with polarization strength.

Second, outside the weak polarization region we found that channels and their currents, which are normally associated with a neuron in its active spiking or bursting state, can also significantly influence its subthreshold excitability. Third, we found that although the values of  $q$  (gating variable for the dendritic  $K_{AHP}$  current) obtained during subthreshold stimulus are small (being no more than about 0.05 of the maximum, compared to near 1 during the burst), results in Fig. 2.6 indicate that the variation in  $q$  with  $M$  is significant enough to effect a transition between sublinear and superlinear TTFS profiles.

The observation that a small fraction of activated channels can have significant influence on the excitability of a polarized neuron places a particular importance on the nascent stages of channel activation. For computational ease many models truncate the

early stages of channel activation (or simply replace more complex functions with sigmoidal or step functions). These modifications may have little effect on spike trains of unpolarized or weakly polarized neurons, however, they will most likely fail to accurately depict polarization-dependent excitability outside of the weak polarization regime.

The ramp injection rate  $M$  may model actual applied ramp currents, or it may approximate the convolution of many pre-synaptic inputs to the dendrite. Results differ only slightly when the somatic injection is replaced by dendritic injection in the model and is less significant when  $g_c$  is larger (data not shown). For the ramp injected current protocol, we have shown that slower sustained input allows for more time for the very slow  $K_{AHP}$  gates to open, thus facilitating hyperpolarization and potential superlinear profiles. These superlinear profiles may also be obtained by varying either  $E_K$  and  $g_{K_{AHP}}$ . In addition, we showed further evidence that the dendritic spikes at strong polarization cause a reversal in excitation (i.e., decreasing TTFS with decreasing  $V_{ds}^{out}$ ) and we note that this is due to the same calcium currents that are responsible for the back-propagation that sustains a burst [49]. In summary, our results suggest that the activation or partial activation of dendritic currents critical to pyramidal cell burst dynamics also play an important role in shaping the polarization-dependent excitability of a neuron.

We chose a two-compartment model to facilitate our analysis. It would be interesting to see how a more complex multi-compartment model would behave. For example, a model with apical and basilar dendritic compartment on either end of a soma compartment would allow for the possibility of injected current taking two paths out of the soma. Although the degree of polarization from the soma to the apical dendrites may be significantly reduced. A possible extension of this study would include a multi-compartment model such as [32]'s 19-compartment CA3 pyramidal model with a graded distribution of currents and possibly additional types of currents.

Finally, looking at our results abstractly beyond the framework of a particular neuron or model neuron, we speculate on the question of what it takes for a neuron to exhibit the characteristics of the weak, intermediate, and strong polarization regions observed in our study

using the polarized PR-model. We conjecture that (1) without a depolarizing dendritic current any reversal in excitability seen at strong polarization would be impossible, (2) the ranges of the weak, strong and intermediate regions depend on how the channels activate with membrane potential, and (3) that the clear division in the polarization-dependent excitability seen in the intermediate region requires two competing currents, one depolarizing and one hyperpolarizing.

## Chapter 3: Effects of Localized Ephaptic Currents On the Spike Timing of Small Networks of Neurons

I go among the Fields and catch a glimpse of a Stoat or a fieldmouse peeping out of the withered grass - the creature hath a purpose and its eyes are bright with it. I go amongst the buildings of a city and I see a Man hurrying along - to what? the Creature has a purpose and his eyes are bright with it.

---

Keats

### 3.1 Introduction

The conduction of ions back-and-forth between the intracellular and extracellular space drives the transmembrane potentials that defines neural activity. However, most models ignore the effects of the extracellular current (ECC). In essence, these models treat the cell membranes as perfectly insulated, dependent on specific anatomical connections such as synapses or gap-junctions for interactions between neurons. Theory and experiments have shown that the ECC due to electrical activity in one neuron may induce a polarization within surrounding cells. As discussed in Chapter 2 the polarization due to electric fields has been shown to affect neurons in several ways including; the resting membrane potential, the time to first spike and spike frequency [13, 14, 25]. In particular, there have been a number of experiments suggesting that the spike propagation through neural tissue can occur solely due to endogenous electric fields. Most recently Qiu et al. [50] has experimentally and computationally shown that the speed of spike propagation through a hippocampal slice is inversely proportional to the distance between cells and thus proportional to the

corresponding increase in extracellular resistance and field amplitude. Importantly, in Qiu et al and preceding work, the effects of endogenous fields on spike propagation were studied using pathological models of neural tissue [51]. These experiments raised the excitability of the neurons by immersing the tissue in a low  $Ca^{2+}$  solution with  $Mn^{2+}$  or through application of convulsants like AP-4 as a model of epileptic activity. In addition, both inhibitory and excitatory synaptic conduction was blocked. The effects of endogenous fields have been probed experimentally by assessing the ability of the endogenous field to synchronize neural populations. These experiments have also been performed with epileptic like models and synaptic activity blocked [15,52–54]. Snow [55] demonstrated that endogenous electric fields could also synchronize with pathologically excitable spike activity in the presence of functional excitatory chemical synapses (picrotoxin was used to suppress inhibitory synapses). To the best of our knowledge there has not been any experimental demonstration of ephaptic effects on physiologically normal tissue models with intact synaptic architecture. In contrast to the waves of propagating spikes found in the aforementioned pathological slices, *in vivo* measurements of pyramidal cell field potentials within the Rodent Hippocampus during several behavioral states reveal selective, sparse, and isolated spiking activity. These selectively spiking pyramidal cells include place cells that encode spatial memory for navigation [56–58]. Here, we focus on the localized effects of polarization induced by ECC, mainly due to the action potentials of neighboring neurons, on the propagation of spikes in a synaptically coupled chain of neurons. We also uncover the underlying mechanisms that relate the induced polarization to cell dynamics and their effect on spike timing.

In this chapter, we are interested in the impact of the ECC due to individual neurons within a network. We first utilize a model where two-compartment pyramidal neurons are embedded in a resistive lattice. The resistive lattice transmits the ECC generated by membrane currents from one neuron throughout the resistive lattice, inducing a polarization in neighboring neurons. Our primary synaptic architecture is where each neuron is synaptically connected to only its neighboring neuron (in one direction). This connectivity we refer to as the sequentially excited (SE) architecture. The SE architecture has the

properties that (1) localized ephaptic effects are limited to nearest-neighbor and (2) the timing between the polarization induced by the neighboring neurons action potential and the synaptic current is fixed. For the SE architecture we find that the time-to-first-spike (TTFS) is non-monotonic with increasing extracellular resistance. This result is contrasted with experimental results showing a monotonically decreasing TTFS with increasing extracellular resistance. The experimental results, however, are with synapses blocked and where the neuons are in a hyper-excited state. Our model is similar to that used by Gluckman [6] in a study of stochastic resonance. Our model is also an extended version of the embedded pair of two-compartment models employed by Park [7, 8] to study synchronization effects between two synaptically and resistively coupled neurons. This model was also used in Cong [59] to explore the effect of DC fields on firing patterns. In these models, the extracellular currents and their effect on the neurons are explicitly solved for at each time step. To both freely vary the timing between action-potential (AP) generated polarized currents and synaptic AMPA current as well as to differentiate mechanisms we developed two single-neuron models. one uses  $t_u$  where we vary the resistances and relative timing between a synaptic current and the polarization induced by ECC associated with neighboring action potentials.

The terminology used for the electrical properties of the extracellular space and its effects has varied over time and among authors. Anastassiou [60] uses the term ephaptic to refer to any effects due to changes in extracellular potential anywhere along the cell membrane, while Jefferys [61] uses ephaptic only when referencing local effects such as that due to the biphasic high-frequency pulses of action potentials. Here we adopt Anastassiou's over-arching definition of ephaptic, ephaptic effects occur at a variety of spatial scales; synapses (microscale), neurons(mesoscale) and networks (macroscale). This work focuses on ephaptic effects at the mesoscale and microscale involving neurons and synapses. The source of the ephaptic current is the transmembrane currents of a single neuron in an active state<sup>1</sup>.

---

<sup>1</sup>We use the term active state to describe any form of sustained depolarization whether it be a single spike or burst. However, under the conditions presented here the active state consists of a single isolated

Previous authors considered the effects of ECC on neurons by combining external electric fields with the endogenous ephaptic effects. However, external fields tend to obscure the relatively small ephaptic effects. Therefore, we focus solely on the endogenous ephaptic effects due to the current sources from individual neurons. Our emphasis on localized current sources at the neuron and synaptic scales differs from a number of previous computational studies, which have focused on the network-wide local field potentials (LFP) that oscillate throughout the hippocampus [51, 62–65]. Note that despite its name LFP’s are not local but global in extent and will not be considered here. In Park et al. [7,8] the ephaptic effects from a single action potential were considered in the context of two coupled continuously spiking Pinsky-Rinzel neurons under an external applied field and found to have important synchronizing effects. Also, Holt and Koch [36] estimated the extracellular potentials associated with an action potential in a cortical pyramidal cell. We are interested in uncovering physiologically plausible conditions for ephaptic currents due to individual neurons in order to have significant neuro-computational effects.

The geometry and physiology of many, if not most neurons, minimizes both the ECC transmitted by a neuron and that neuron’s susceptibility to polarization. Neurons whose active channels are localized and not well aligned with their neighbors generate less ephaptic polarization and have less of an effect on its neighbors. Pyramidal cells are the primary excitatory neurons in the hippocampus and neocortex. They have elongated dendrites with active channels. In the hippocampus, they are arranged in a laminar fashion, and the somatic-dendritic axis of neighboring pyramidal cells are well-aligned. Pyramidal cells of the hippocampus are well-suited for a study on ephaptic effects. As in the previous chapter we adopt a model consisting of Pinsky-Rinzel CA3 pyramidal neurons [4] synaptically connected and embedded in a resistive array to approximate the flow of currents in the extracellular space (ECS) and subsequent polarization. The Pinsky-Rinzel model has previously been used in a number of studies involving electric-field induced polarization [7,8,10,16].

We may view the neurons as current sources and sinks to the extracellular space (ECS).  
spike.

The resistance of the ECS modulates the polarization potentials imposed on the neurons. Resistance is a product of the fluid properties of the ECS and the path the ions must navigate. Kuffler [66] describes this path as being like the thin streams of water that surround the bubbles in a foam of soap. Several factors have been found to change either the path that the ions flow or the resistivity of the fluid. For example, extracellular potassium levels have been shown to influence cell volume and thus affect the extracellular volume (ECV) and EC resistance [67]. The resistivity of the fluid will also vary depending on concentrations of macromolecules and an associated change in tortuosity in the ECS [68].

The ECS was observed to act as a low-pass filter so that higher frequency components of a signal diminish as the signal passes through the ECS. This fact has been used to explain the dominance of the lower-frequency synaptic sources and the apparent absence of the high-frequency action potentials in scalp recordings [69]. Based on computations by Bedard [70] dispersive effects should be minimal over the short distance between pyramidal cells while there may be more significant dispersion along the soma-dendrite axis. In this work, we do not model frequency-dependent conductance.

Ephaptic effects with synaptic conduction blocked, have been shown to induce synchronized firing in a hippocampal slice [53]. However, this appears to be true only for neurons that are in a highly excitable state (see for example [53]). Here, we compute the sensitivity of the time-to-first-spike (TTFS) driven by chemical synapses with respect to the timing of action potential generated ECC and the extracellular resistance. The significance of the ECC is dependent on the synaptic excitatory current relative to the excitability of the neuron in its resting state. In other words, the level of effect of the ECC on TTFS depends on how close the synaptically excited neuron is to a bifurcation between spiking and a failure to spike.

To help understand the underlying mechanisms responsible for our results we found it useful to divide the localized ephaptic effects due to the activity of individual neurons into three components: (1) Source loading: which refers to the polarization of the source neuron by its own transmembrane currents. (2) The response of a neurons' non-synaptic membrane

currents to a neighboring neuron's action potential. (3) Synaptic coupling: The ECC polarizes the post-synaptic dendrite which alters the synaptic currents driving potential. Source loading is not an independent component rather it depends on both the synaptic coupling and the interactions with the non-synaptic currents. The dominant mechanism for source loading is the effect of the polarizing current to shorten slightly the spike width and thus the AMPA current delivered to the next neuron.

In this work, we explicitly compute the excitability through computational modeling and simulation. We may also understand excitability in the context of dynamical systems and bifurcation theory. A bifurcation occurs when there is a qualitative change in the solution as one or more parameter values are varied. Hodgkin [71] classified the repetitive firing of axons into three types: Class I exhibits spiking at arbitrarily low frequency, Class 2 only has a minimum spiking frequency and Class 3 neurons only spike once . Later, it was established that Class 1 or Class 2 excitability may be placed in the context of a saddle-node on an invariant circle (SNIC) or Andronov-Hopf type bifurcations [72]. Neurons with Type I excitability are described as being integrators and those with type 2 as resonators [73,74], and each has their own neural-computational properties. It is important to realize that real neurons and many model neurons may switch from one type to another. Often, this switch occurs in response to changes in the baseline excitability through higher or lower levels of synaptic input [75, 76]. Also, relating real or multi-dimensional model neurons to an SNIC or Andronov-Hopf bifurcation may not be straightforward or even possible since these bifurcations are defined for one- and two- dimensions respectively. In some cases, we may neglect a variable or treat it as a constant and formally reduce the dimensions. Here we use the full eight-dimensional PR model and project the state of the neuron onto the  $V_s - n$  plane to see if we can observe a qualitative change in the trajectories. By projecting the eight-dimensions onto the two soma variables we are effectively saying that nothing interesting happens in the other six dimensions.

Our results suggest that spike timing and synaptic coupling through the polarization of the post-synaptic dendrite could play an important role in ephaptic effects on spike

timing. When we remove synaptic coupling, our modeling is consistent with experimental results showing decreasing TTFS with increasing extracellular resistance and associated increase in field potential amplitude. Furthermore, we found that we were able to employ single-neuron models to compute the response of a pyramidal neuron to the ECC from a neighboring neurons action potential for a range of amplitudes and timing relative to some external synaptic input. These computed responses predicted well the spiking behavior found using our full resistive lattice subject to randomly spiking and synaptically isolated neurons.

In section 3.2 we describe our methodology including numerical methods and physiological basis for our choice of parameters. In section 3.3 we present our results in the form of time-to-first-spike (TTFS) calculations for a range of extracellular resistances. In section 3.4 we discuss our results and potential future work.

## 3.2 Methods

### 3.2.1 Polarized two-compartment PR model neuron

For the two-compartment PR model, we modify the equations to accommodate the polarization between compartments as was done in [7, 8]. The transmembrane potentials are defined by the difference in potential across the cell membrane.

$$V_s = V_s^{in} - V_s^{out} \quad (3.1a)$$

$$V_d = V_d^{in} - V_d^{out} \quad (3.1b)$$

Membrane channels are functions of the transmembrane potential. However, current flowing passively between the two compartments is proportional to the difference in their intracellular potentials,  $V_s^{in}$  and  $V_d^{in}$ . The original Pinsky-Rinzel model, as in most models, implicitly assumed a constant extracellular potential, *i.e.*  $V_s^{out} = V_d^{out}$ . In this case, the intracellular potential between compartments,  $(V_d^{in} - V_s^{in})$ , is equal to the difference in

transmembrane potentials,  $(V_d - V_s)$ . Allowing our compartments to have two different extracellular potentials, we define the potential difference directly outside the dendrite and soma as  $V_{ds}^{out} = V_d^{out} - V_s^{out}$ . The current out of the dendrite and into the soma is defined as  $I_{ds}^{in}$  and is given by:

$$\begin{aligned} I_{ds}^{in} &= \frac{g_c}{\rho} (V_d^{in} - V_s^{in}) \\ &= \frac{g_c}{\rho} (V_d - V_s + V_{ds}^{out}). \end{aligned} \quad (3.2)$$

The parameter  $g_c$  is the inter-compartment conductance, and  $\rho$  is the fraction of soma surface area to the total cell surface area. The polarized PR model is given by

$$\begin{aligned} C_m \cdot dV_s/dt &= I_{sLeak}(V_s) + I_{Na}(V_s, h) + \\ &\quad I_{K-DR}(V_s, n) + I_{ds}^{in} + I_s(t)/\rho, \end{aligned} \quad (3.3a)$$

$$C_m \cdot dV_d/dt = I_{dLeak}(V_d) + I_{Ca}(V_d, s) + \quad (3.3b)$$

$$\begin{aligned} &I_{K-AHP}(V_d, q) + I_{K-C}(V_d, Ca, c) - \\ &I_{ds}^{in} \frac{\rho}{1-\rho} + \frac{I_{AMPA}(V_d)}{1-\rho} \\ &dCa/dt = -0.13I_{Ca} - 0.075Ca. \end{aligned} \quad (3.3c)$$

The parameter  $Ca$  represents a unitless measure of the amount of intracellular calcium. For the equation governing intracellular Ca levels, the coefficient  $-0.075$  is based on optical measurements of the decay of Ca in Purkinje dendrites ( $-0.075s^{-1} = 1/\tau_{Ca} = 1/13.33ms$ ) from [32, 39]. The sign of the coefficient  $-0.13$  multiplying  $I_{Ca}$  means that current into the dendrite compartment results in an increase intracellular Ca. This coefficient represents an

exchange of coulombs provided by the  $I_{Ca}$  current for moles of  $Ca^{2+}$ . Traub [32] presents an abstract model of intracellular  $Ca^{2+}$  where each compartment rate of absorption can be varied by varying the thickness of an imagined sub-cellular membrane. Traub fine-tuned this coefficient to best match experimental data. The polarized PR model differs from the original only in the addition of the terms  $I_{ds}^{in}$  and  $-I_{ds}^{in}\rho/(1-\rho)$ . In this work, we fix the morphology of the model neurons by setting  $\rho = 0.5$  for all neurons in the chain. We also hold fixed the electrotonic relationship between soma and dendrite by setting  $g_c = 2.1 \text{ ms/cm}^2$ . The individual currents with their dependencies on the dynamic gating variables  $h, n, s, c$ , and  $q$  are as follows:

$$\begin{aligned}
I_{sLeak} &= -g_L(V_s - E_L) \\
I_{dLeak} &= -g_L(V_d - E_L) \\
I_{Na} &= -g_{Na}m_\infty^2 h(V_s - E_{Na}) \\
I_{K-DR} &= -g_{K-DR}n(V_s - E_k) \\
I_{Ca} &= -g_{Ca}s^2(V_d - E_{Ca}) \\
I_{K-AHP} &= -g_{K-AHP}q(V_d - E_k) \\
I_{K-C} &= -g_{K-CC}\chi(V_d - E_k) \\
I_{AMPA} &= -g_{AMPA}W(t)(V_d - V_{syn}).
\end{aligned} \tag{3.4}$$

Fig. 3.1 depicts the flow of currents, either inward (depolarizing) or outward (hyperpolarizing), at typical steady-state values. In our model, a cathode is imagined to be placed near the soma and the anode near the apical dendrites. Thus, a positive (negative) field depolarizes (hyperpolarizes) the soma and hyperpolarizes (depolarizes) the dendrite. Note that this convention is a reversal in field sign from that found in [13, 24], and [29], but follows that used in [7, 8].

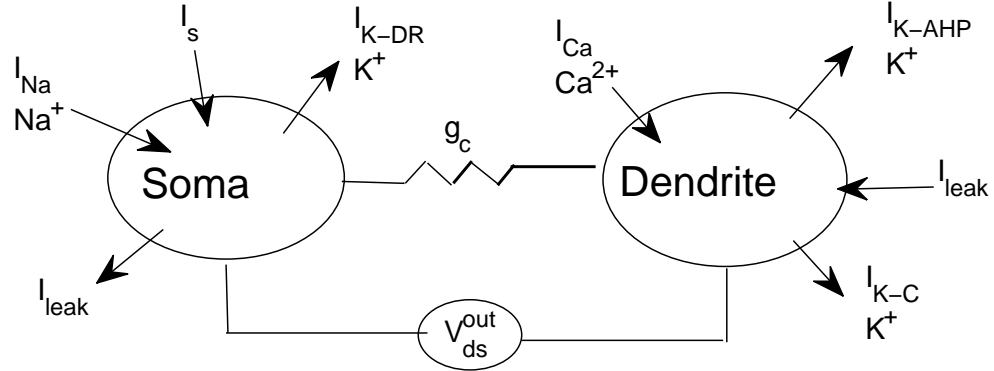


Figure 3.1: Pinsky-Rinzel polarized model neuron

There are five gating variables ( $h$ ,  $n$ ,  $s$ ,  $c$ , and  $q$ ) whose kinetics take on the *standard* Hodgkin-Huxley form. The gating variables  $h$  and  $n$  are functions of  $V_s$ ,  $s$  and  $c$  are functions of  $V_d$ , and both  $q$  and  $\chi$  are functions of the intra-cellular calcium concentration  $Ca$ . Equations 3.3 and 3.4 are thus coupled with the five first-order gating kinetics given below:

$$dh/dt = (h_\infty(V_s) - h)/\tau_h(V_s) \quad (3.5a)$$

$$dn/dt = (n_\infty(V_s) - n)/\tau_n(V_s) \quad (3.5b)$$

$$ds/dt = (s_\infty(V_d) - s)/\tau_s(V_d) \quad (3.5c)$$

$$dc/dt = (c_\infty(V_d) - c)/\tau_c(V_d) \quad (3.5d)$$

$$dq/dt = (q_\infty(Ca) - q)/\tau_q(Ca) \quad (3.5e)$$

$$dW/dt = \sum_j H(V_{s,j} - 20) - W/2. \quad (3.5f)$$

In eq. 3.5(f) the index  $j$  refers to any pre-synaptic neurons connected to the dendrite compartment. In this case the synaptic conductance does not activate until the pre-synaptic

soma of the neuron has exceeded 20 mv.

### 3.2.2 Modeling the extracellular conductance

We use a resistive lattice to model the ECC. Our lattice is similar to that used to embed the chain of PR neurons found in Gluckman et al. [6] and the pair of PR neurons in Park et al. [7,8]. For each neuron in the chain the two PR compartments act as current sources and sinks. Here, the top and bottom of the lattice is set to ground. In our model, the resistive lattice forms a ring of N neurons. A diagram of our embedded chain of PR neurons is shown in Fig. 3.2. For most of the results presented here N=51 while for the hgh resolution computations involving the randomly spiking neuron (Sec. 3.3.7) N=25. Due to our synaptic architecture, limited runtime, and the attenuation of the current through the lattice additional neurons did not change our results. All of the dynamic variables in each neuron in the chain are coupled through the currents in the lattice. More specifically, the neurons are coupled through  $V_{ds}^{out} = I_{ds}^{out} R_{ds}^{out}$ , the imposed potential difference outside the dendrite and soma of each neuron. Thus the system is a large set of coupled linear equations. The currents in the lattice satisfy Kirchoff laws at junctions and over loops. The ODEs of the polarized PR neurons and the linear equations to solve the currents constitute a differential algebraic equation. As in Park et al. [7,8], Gluckman et al.[6], and Traub et al. [9] the ODE describing the polarized PR neurons are updated using the  $V_{ds}^{out}$ 's calculated at the prior time step. Such a methodology means that the solution may be unstable at a certain step size. Our problem is inherently stiff in the sense that we have vastly different time-scales. Specifically, we have over three orders of magnitude difference in the kinetics of the gating variables and have an effectively instantaneous algebraic condition due to solving the resistive array. Nonetheless, we found that our solution stabilized for reasonable step sizes. We employed the ODE45 Matlab integrator with an absolute error of  $1e^{-6}$  and a relative error of  $1e^{-11}$ . However the TTFS converged to about  $1e^{-4}$  of its value for a  $1e^{-12}$  relative error. Thus when computational time is limited we relaxed the relative tolerance down to  $1e^{-6}$ .

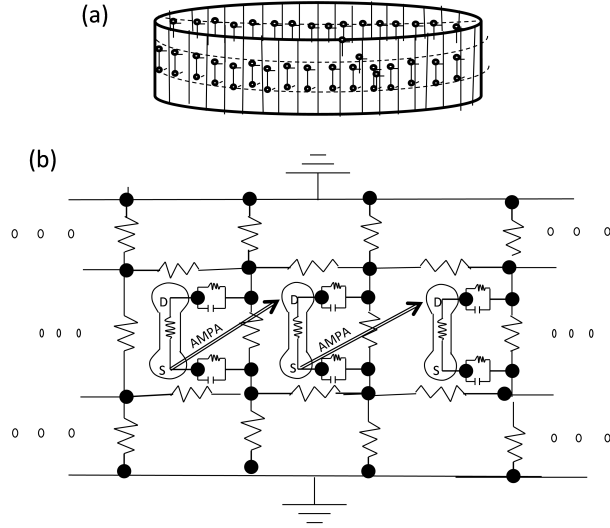


Figure 3.2: Schematic of chain of synaptically coupled PR neurons embedded in a resistive lattice. The resistive lattice forms a continuous grid. However, the  $n$ th and 1st neurons are not synaptically connected. The resistive grid (i.e. the number of neurons) typically consisted of 51 model neurons. The duration of the computations were often such that only 10 or so neurons spiked.

### Extracellular Properties of the Hippocampus and Our Model.

Most previous studies explored the ephaptic effects assuming a fixed value for the extracellular resistance [6–9]. Wei [65] recently investigated the effects of extracellular resistance on the dependence of spike threshold and frequency as a function of a constant applied electric field.<sup>2</sup> Anatomical studies and experiment have revealed substantial variation in the geometry of the ECS as well as the properties of the interstitial fluid, thus implying

---

<sup>2</sup>Park (2005) related the  $[K^+]_o$  to the resistance, but this paper did not present any systematic results.

significant variation in the EC resistance [77–80]. Also, there is evidence that age, disease, and activity levels in the hippocampus can affect the extracellular resistance [68, 81, 82]. Thus we try to gauge the significance of changing extracellular resistance when it comes to spike timing and spike propagation.

Gluckman [6] and Park [7, 8] specified the extracellular resistances in their lattices in terms of fractions of the internal dendritic-somatic resistance,  $R_{ds}^{in}$ , which is equal to  $1/(g_c Area)$ . These papers all used the same resistances:  $R_{ds}^{out} = 0.1R_{ds}^{in}$ ,  $R_{dd} = R_{ss} = 0.1R_{ds}^{out}$ , and top and bottom resistances  $R_{td} = R_{sg} = 12R_{ds}^{out}$ . Here, we will refer to these resistances as the *standard*. As in [7, 8] we use  $R_{ds}^{in} \approx 80M\Omega$  meaning that for the *standard* resistance,  $R_{ds}^{out} \approx 8M\Omega$ . To understand how the geometry and interstitial media effect the resistance we first assume as in [9] that the space between pyramidal neurons is a rectangular parallelepiped. Then if we assume a uniform flow we can apply the familiar formula,  $R = \rho l/A$ . Where  $A$  is the cross-sectional area,  $l$  is the length parallel to the current, and  $\rho$  is the resistivity. In general, there is a great uncertainty in the parameters that determine resistance. These uncertainties include the actual flow of current. (For example, an unknown fraction of current is known to take transglial paths [79].) Furthermore, these characteristics change due to different mechanisms operating over a number of different time-scales. At a slow time-scale these mechanisms include changes in cell morphology with age and the effects of disease [81]. At a much faster time scale [79] has shown *in vivo* that localized resistivity in the ECS surrounding CA1 layer is activity-dependent increasing from 20-50%. The same study [79] found that resistivity measured about 30% greater in slices than *in vivo*. Pyapali [78] performed measurements of the CA1 morphology in the Rat using intracellular staining *in vivo* and *in vitro* and found that the total length had mean of about  $700\ \mu m$  with *standard* deviation of  $\approx 100\ \mu m$ . Systematic measurements of the cross-sectional area relevant to  $R_{ds}^{out}$  are lacking. This is the area between pyramidal cells, or the square of the distance between cells. A number of studies use  $20\ \mu m$  for this quantity, however, Traub [9] notes that the distance could easily be smaller and photomicrographs of

the hippocampus pyramidal cell layer suggests distances as low as  $10 \mu\text{m}$ . For the purposes of estimating the variance in resistance we shall assume  $A = (20 + / - 5\mu\text{m})^2$ . Applying a 25% variance in the *in vivo* measured apical dendritic resistivity of  $287 \Omega\text{-cm}$  [79] we estimate a range of  $R_{ds}^{out}$  between  $0.025R_{ds}^{in}$  and  $0.16R_{ds}^{in}$ <sup>3</sup>. This range of  $R_{ds}^{out}$  values may be compared to the parameterized range of  $R_{ds}^{out}$  used in our results.

### Frequency Dependent Conductivity in the ECS

The extracellular conductivity is frequency dependent [70, 83, 84]. The extracellular space behaves as a low-pass filter. Higher frequency components of a signal decay rapidly. In our model the ECC associated with the action potential of the polarized PR model is biphasic and occurs over a period of about 2 ms. The bulk of the power in the signal occurs above 500 Hz. Our action potential generated ECC is very similar to that computed by [70] using a one compartment conductance based model. Applying Bedard's [70] results to our model suggest very little attenuation over short distances  $\approx 5\mu\text{m}$  but more substantial attenuation of the higher frequency components over  $100 \mu\text{m}$ . We conclude that the longitudinal polarization will be little altered although there might be more substantial changes along the soma-dendrite axis. As in [6–8, 59] we use a purely resistive array.

#### 3.2.3 Synaptic strength and soma bias current modulate excitability

Constant bias currents such as  $I_s$  in the PR model adjust the excitability of the neuron. The more negative  $I_s$ , the longer it takes a given synaptic input to elicit a spike or the stronger the minimum synaptic strength needed simply spike at all. Physiologically, the bias current may be thought of as a crude approximation of inhibitory synaptic input without the feedback dynamics. Together, the synaptic AMPA conductance and the bias current establish a level of excitability in the chain of neurons. Close to a bifurcation, ephaptic effects are amplified.

---

<sup>3</sup>What we are calling the *standard* value for  $R_{ds}^{out}$  of  $8M\Omega$  differs from the  $R_{ds}^{out}$  obtained using the mean values cited. Specifically, for  $\rho = 287\Omega - \text{cm}$ ,  $l = 700\mu\text{m}$ , and  $A = 20 \mu\text{m}^2$   $R_{ds}^{out} \approx 5M\Omega$

### 3.2.4 Network Architecture

We first use a very simple chain of identical neurons as in Fig. 3.2. This network of identical neurons is nearest-neighbor and uni-directionally synaptically coupled. We initiate our computations by stimulating a single neuron. With no resistive lattice the neurons spike sequentially at fixed intervals and the computed TTFS between any two neurons in the chain should be identical (within numerical precision). We refer to this synaptic architecture as being sequentially excited SE.

To model the ECC we embed the sequentially excited chain in a resistive lattice. The ECC due to transmembrane current is global and attenuates with distance. In principal, this greater than nearest-neighbor ECC effect may lead to variance in the TTFS within the embedded chain. However, by implementing a sequentially excited architecture, the active states of nearby neurons will be separated in time by approximately the TTFS. If the TTFS is sufficiently long and the induced polarization sufficiently weak, then a neuron will have time to re-equilibrate in response to greater than nearest-neighbor spikes. In such cases, for a sequentially excited network the effects of the ECC are approximately nearest-neighbor as well. In addition, the SE architecture imposes a fixed relative timing between the polarization due to the ECC generated by a potential spike and the synaptic input. While it is reasonable to assume that the ECC propagates instantaneously, the synaptic (AMPA) current only begins to activate when the presynaptic somatic potential exceeds 20 mV, meaning that AMPA current trails the ECC by about 0.2 ms.

### 3.2.5 Simplified models

We used XPPAUT to compute and analyze our single-neuron models. To freely vary the timing of the ECC and to segregate effects by their causes we model the polarization by applying an interpolating function to two single-neuron models. To avoid possible confusion with the polarization,  $V_{ds}^{out}$ , obtained by solving the currents in the resistive lattice every time step, we denote the interpolated polarization by using all capitals and specifying that it is an explicit function of time,  $VDS(t)$ . The interpolating function for the polarization

is obtained by computing  $V_{ds}^{out}$  for the nearest neighbor of a spiking neuron using the full resistive lattice model (Eqs. 3.3-3.4). The polarizations from the full resistive model is then output at evenly spaced intervals using MATLAB's deval function. For the VDS(t) used here polarizations were calculated every 1e-6 seconds over a duration of 16 ms <sup>4</sup>.

In the first single neuron model the AMPA current was defined as in our chain of polarized neurons, with the active channel conductance  $W$  being a variable in the ODE. The equations follow:

$$C_m \cdot dV_s/dt = I_{sLeak}(V_s) + I_{Na}(V_s, h) + I_{K-DR}(V_s, n) \quad (3.6a)$$

$$+ \frac{g_c}{\rho} (V_d - V_s + Amp * H(t - \tau_{ECC}) * H(\tau_{ECC} + 16 - t) * VDS(t - \tau_{ECC})) + I_s(t)/\rho,$$

$$C_m \cdot dV_d/dt = I_{dLeak}(V_d) + I_{Ca}(V_d, s) + \quad (3.6b)$$

$$I_{K-AHP}(V_d, q) + I_{K-C}(V_d, Ca, c) +$$

$$\frac{g_c}{\rho} (V_s - V_d - Amp * H(t - \tau_{ECC}) * H(\tau_{ECC} + 16 - t) * VDS(t - \tau_{ECC}))$$

$$+ I_{ds}^{in} \frac{\rho}{1 - \rho} + \frac{I_{AMPA}(V_d)}{(1 - \rho)}$$

$$dCa/dt = -0.13I_{Ca} - 0.075Ca \quad (3.6c)$$

$$I_{AMPA} = -\bar{g}_{AMPA} W(t) (V_d - V_{syn}) \quad (3.7)$$

$$W' = H(V_{s,pre} - 20) - W/2.$$

Where H denotes the Heaviside function. We apply the AMPA current by defining  $V_{s,pre}$  as follows

---

<sup>4</sup>A full 16 ms far exceeds the time needed as after more than 2-3 ms the polarization due to the action potential is negligible.

$$\begin{aligned}
V_{s,pre} &= AH(t - t_{pre})H(t_{pre} + t_{spkdur} - t) \\
t_{spkdur} &= 1.2ms \\
A &> 20mV
\end{aligned} \tag{3.8}$$

Results are given in terms of the relative time between the presynaptic pulse,  $\tau_{pre}$ , and the time of the ECC polarization,  $\tau_{ECC}$ , due to the neighboring action potential. Thus, we define  $\tau = \tau_{ECC} - \tau_{pre}$  as the relevant parameter to describe timing effects. Amp modulates the amplitude of  $V_{ds}^{out}$  to parameterize the effects of changing extracellular resistance. The Heaviside functions on either side of  $VDS(t)$  in Eqs. 3.9 is there to make sure we do not use and extrapolated values beyond the 16 ms of data.

For the second single neuron model, we use the an interpolating function for  $I_{AMPA}$  as well as for  $V_{ds}^{out}$ . The data for the interpolated AMPA function is taken for a chain of PR neurons without any resistive lattice. The significance of the interpolated AMPA currents is that it will not be affected by hyperpolarization or depolarization of the postsynaptic dendrite due to the ECC, thus eliminating the synaptic-ECC coupling component. In addition, since the polarization used for the interpolation,  $VDS(t)$ , captures only the polarization due to a neighboring neurons' action potential source loading is absent from both single neuron models. The absence of source loading will have the effect of raising the excitability.

For the second model we have:

$$C_m \cdot dV_s/dt = I_{sLeak}(V_s) + I_{Na}(V_s, h) + I_{K-DR}(V_s, n) \quad (3.9a)$$

$$+ \frac{g_c}{\rho} (V_d - V_s + Amp * H(t - \tau_{ECC}) * H(\tau_{ECC} + 16 - t) * VDS(t - \tau_{ECC})) + I_s(t)/\rho,$$

$$C_m \cdot dV_d/dt = I_{dLeak}(V_d) + I_{Ca}(V_d, s) + \quad (3.9b)$$

$$\begin{aligned} & I_{K-AHP}(V_d, q) + I_{K-C}(V_d, Ca, c) + \\ & \frac{g_c}{\rho} (V_s - V_d - Amp * H(t - \tau_{ECC}) * H(\tau_{ECC} + 16 - t) * VDS(t - \tau_{ECC})) \\ & + I_{ds}^{in} \frac{\rho}{1 - \rho} + \frac{SYN(t - \tau_{pre})}{(1 - \rho)} \end{aligned}$$

$$dCa/dt = -0.13I_{Ca} - 0.075Ca \quad (3.9c)$$

The second single neuron model has the  $I_{AMPA}$  replaced by the interpolated function  $SYN(t)$ ,  $W$  is eliminated and there is no longer a need for  $V_{s,pre}$  as defined in Eq. 3.8. As mentioned, the data for the AMPA interpolations was obtained using calculations without the resistive lattice over a duration of 32.78 ms at a resolution of 1e-6 s. Both models used XPPAUT's lookup table function with the linear interpolation option. We denote  $\tau$  for the SE architecture by  $\tau^* \approx 0.2$  ms.

We then systematically explore the effects of the relative timing between the ECC from a spiking neuron and synaptic AMPA. This approach allows us to freely and easily adjust both the timing as well as the amplitude of the imposed polarization. This is similar to a phase-response analysis, however, in this case the unperturbed model is at rest rather than periodically spiking. Our phase-and amplitude- response of a resting neuron confirms, clarifies, and expands our understanding of the underlying mechanisms first observed with the one-dimensional sequentially excited embedded chain.

### 3.2.6 Integrals of currents to evaluate neural response to polarization.

To quantify the contributions and dependence on extracellular resistance,  $R_{ds}^{out}$  we integrated ionic currents and the dendritic membrane potential dependent part of the AMPA current over time to get a total charge per membrane area. These totals were computed for a range of  $R_{ds}^{out}$ . We isolated the response of the non-synaptic currents by using a full resistive lattice with no synaptic connectivity between neurons. One neuron was stimulated to spike and we computed the currents of a neighboring neuron. The neurons were initially at rest and the polarization induced currents but quickly returned to equilibrium.

$$Q_{ion}(R_{ds}^{out}) = \int_{t_0}^{t_f} (I_{ion}(t; R_{ds}^{out}) - I_{ion}(0)) dt, . \quad (3.10)$$

$$Q_{sc}(R_{ds}^{out}) = - \int_{t_0}^{t_f} g_{AMPA} W(t) V_d(t; R_{ds}^{out}) dt \quad (3.11)$$

### 3.2.7 Addition of a synaptically isolated and randomly spiking neuron.

We now consider the effect of a randomly spiking neuron within a chain of neurons in a SE architecture. The isolated neuron is resistively connected but synaptically isolated (see Fig. 3.19 (a)). One objective of this simulation is to explain the effects of this isolated and randomly spiking neuron on its neighbors through our previous analysis involving simpler models.

## 3.3 Results

### 3.3.1 The ECC from an isolated spike of a single neuron

In our resistive lattice (Fig. 3.2) the flow of current through the cellular membrane is modeled by currents connecting the soma and dendrite to the lattice. The total current

flowing between the compartments and the resistive lattice is proportional to the rate of change of their membrane potentials. Thus, if the neuron is at rest, then there is no net flow of current into or out of the lattice. Moreover, any gradual change in membrane potential, as might occur during a subthreshold stimulus, is bound to be small. Consequently, the dominant contribution to the ECC comes from active spiking or bursting neurons when the membrane potentials change rapidly. Indeed, the waveforms characteristic of action potential spikes is evident in field potential recordings [85–87]

In our model, the ECC affects neurons in the chain by imposing a polarization,  $V_{ds}^{out}$ , between the compartments.  $V_{ds}^{out} = I_{ds}^{out} R_{ds}^{out}$ , where  $I_{ds}^{out}$  is the current flowing in the extracellular space between the dendrite and soma (positive current means positive charge flows from the dendrite to soma).  $R_{ds}^{out}$  is the resistance along the dendritic-somatic axis.

Fig. 3.3 shows the polarization and membrane potentials for a single spiking PR neuron embedded in a resistive array with *standard* resistance values. The only connectivity between neurons is through the resistive lattice. The polarization induces a current between the soma and dendrite that redistributes the charge. This polarization does not *directly* alter the current flow in and out of the membrane and if the membrane is passive there is no change in the total charge stored in the neuron. However, membrane potential-dependent conductances are sensitive to polarization and the change in conductance alters the net charge. Notice that when one compartment depolarizes the other hyperpolarizes (compare (h) and (i) of Fig. 3.3). Since we use a purely resistive lattice the shape of the polarization does not change, however, the amplitude diminishes with distance from the source. For positive  $V_{ds}^{out}$  the potential of the ECS outside the dendrite is higher than that outside the soma. Positive  $V_{ds}^{out}$  occurs at the start of a spike when the rapid influx of sodium into the soma results in more net positive charge outside the dendrite than the soma. The shape of the polarization reflects the flow of current during a spike; initial fast depolarizing sodium current followed by the slower hyperpolarizing potassium delayed-rectifying current. Also, the polarization current flowing between compartments is small compared to the currents during an action potential.

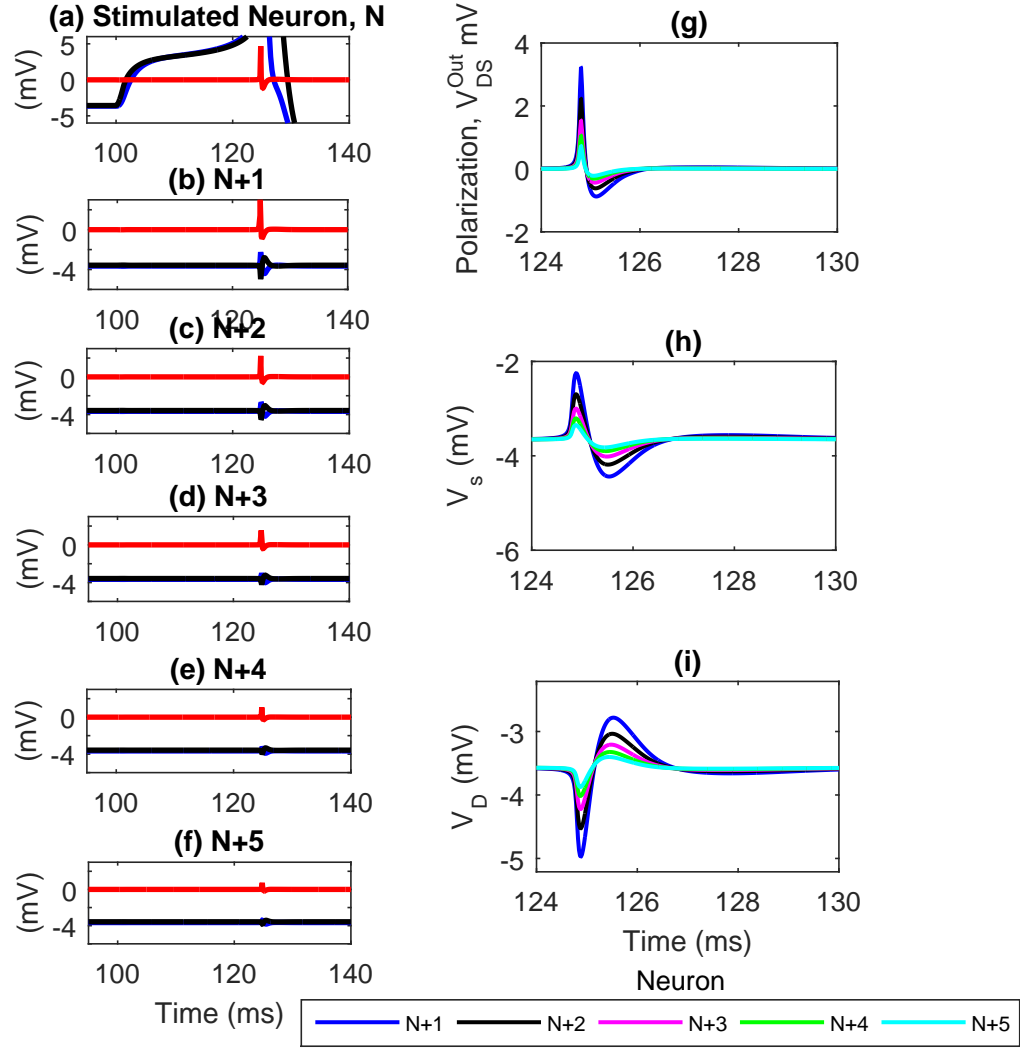


Figure 3.3: Shown is the polarization induced between the soma and dendrite compartments by the ECC of a single spike and the resulting transmembrane potentials. There is no synaptic connectivity. Computations are with 51 PR neurons in a chain embedded in a resistive lattice as in Fig. 3.2. The  $N$ th neuron is stimulated through its synaptic (AMPA) conductance (see methods). As a result the stimulated neuron responds with a single isolated spike. The changing membrane potentials produce ECC that flow to either side of the lattice. In the figure, results are shown only on one side of the stimulated neuron as the results are symmetric around  $N$ . (a)-(f) show the polarization,  $V_{ds}^{out}$ , (red) and the somatic and dendritic membrane potentials (blue and black respectively) for the stimulated neuron and its five closest neighbors. In (a) the soma and dendrite spike sharply to above 80 mV and 40 mV respectively (The y-axis is cut off to show the much smaller polarization) in only 1-2 ms. The ECC during this period dominates that produced over the prior 25 ms of subthreshold depolarization. The ECC propagate instantaneously through the lattice but diminishes significantly with distance from the stimulated neuron (b-f). The polarization,  $V_{ds}^{out}$ , and the resulting induced membrane potentials are shown for the five nearest neighbors (g-i). The amplitude decreases with neuronal position, however, the temporal profile of the signal does not change through the purely resistive lattice.

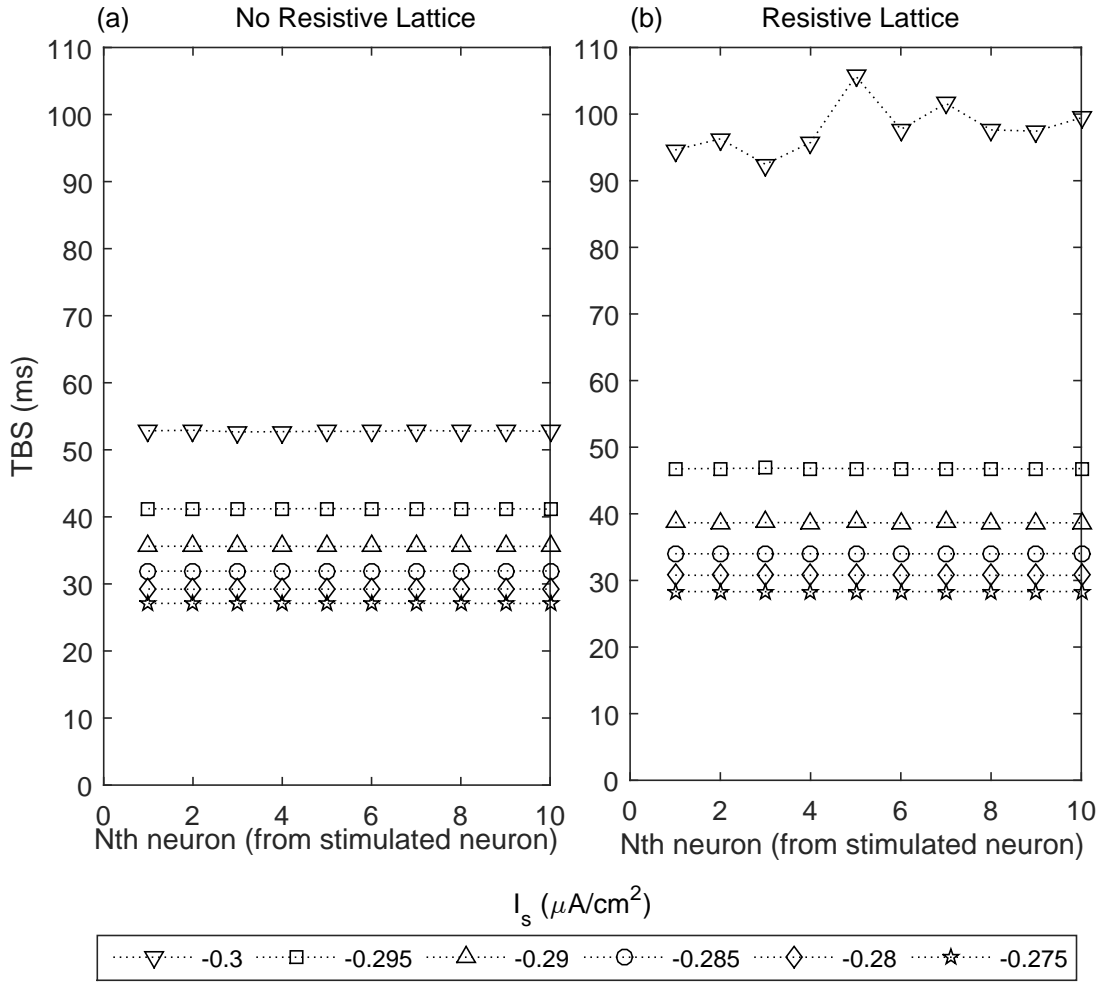


Figure 3.4: Time Between Spikes (TBS) down a sequentially excited chain. Results are shown with (b) and without (a) the resistive lattice. The symbol indicates the level of inhibition,  $I_s$ . The less inhibition the shorter the TTFS. Notice that in both cases the gap in TBS grows with increasing inhibition with a dramatic jump going from  $I_s = -0.295 \mu A/cm^2$  to  $I_s = -0.3 \mu A/cm^2$  especially in the resistive lattice case where the TBS more than doubles. This rapid increase in TBS near the bifurcation is shown more explicitly in Figs 3.5 and 3.7 and is characteristic of Type I neurons as discussed in Sec. 3.3.3. Next notice how there is little variation in TBS down the chains except for  $I_s = -0.3 \mu A/cm^2$ . Without the resistive lattice only small differences, proportional to the integration step size, are observed. This is as expected since the only coupling between neurons (without the resistive lattice) is synaptically which by design was made to be nearest-neighbor only. The inclusion of the resistive lattice does provide a global coupling that could introduce variability in the TTFS down the chain. However, in this case (sequentially excited architecture with *standard* resistances), greater than nearest-neighbor ECC effects are evidently negligible except for  $I_s = -0.3 \mu A/cm^2$  which is close to the point where spike failure occurs.

### 3.3.2 Sequentially excited chain with resistance is dominated by nearest-neighbor interactions.

By design, in the sequentially excited chain without resistance, propagation between any two neurons should be identical. The addition of the ECC, modeled by the resistive lattice, adds a global component. In principle, the addition of the ECC may result in a cumulative effect and spike propagation between neurons may vary. In Fig. 3.4, we computed the TTFS for ten consecutively spiking neurons sequentially excited with and without the resistive lattice. Computations were made for fixed maximal *gAMPA* and over a range of inhibition,  $I_s$ . Without resistance (a), any variation in the TTFS' appears negligible. With resistance (b), noticeable variation is found only at a level of inhibition that places the neurons near spike failure ( $I_s = -0.3 \mu A/cm^2$ , filled, downward triangles). As would be expected, any variability in the TTFS for the sequentially excited architecture without resistance is attributable to numerical precision and are step-size dependent.

To quantify the variance in Fig. 3.4 we compute the percent difference ( $100 * (\text{std. dev}/\text{mean})$ ) in the TTFS for the ten neurons for each  $I_s$  (not shown). The variance in TTFS is quite low and decreases with increasing  $I_s$ . For example, at  $I_s = -0.295 \mu A/cm^2$  the TTFS is around 42 ms and the percent difference is 0.028 equating to about 0.01 ms. The percent difference for  $I_s = -0.3 \mu A/cm^2$ , very near the threshold to non-spiking, is about 3.7% with resistance and 0.7% without. These larger errors occur near the spike bifurcation and are consistent with increased sensitivity to both numerical accuracy and greater than nearest-neighbor ECC effects.

Since the variations in TTFS from neuron to neuron are due to numerical accuracy all results for the sequentially excited architecture are given in terms of the mean TTFS.

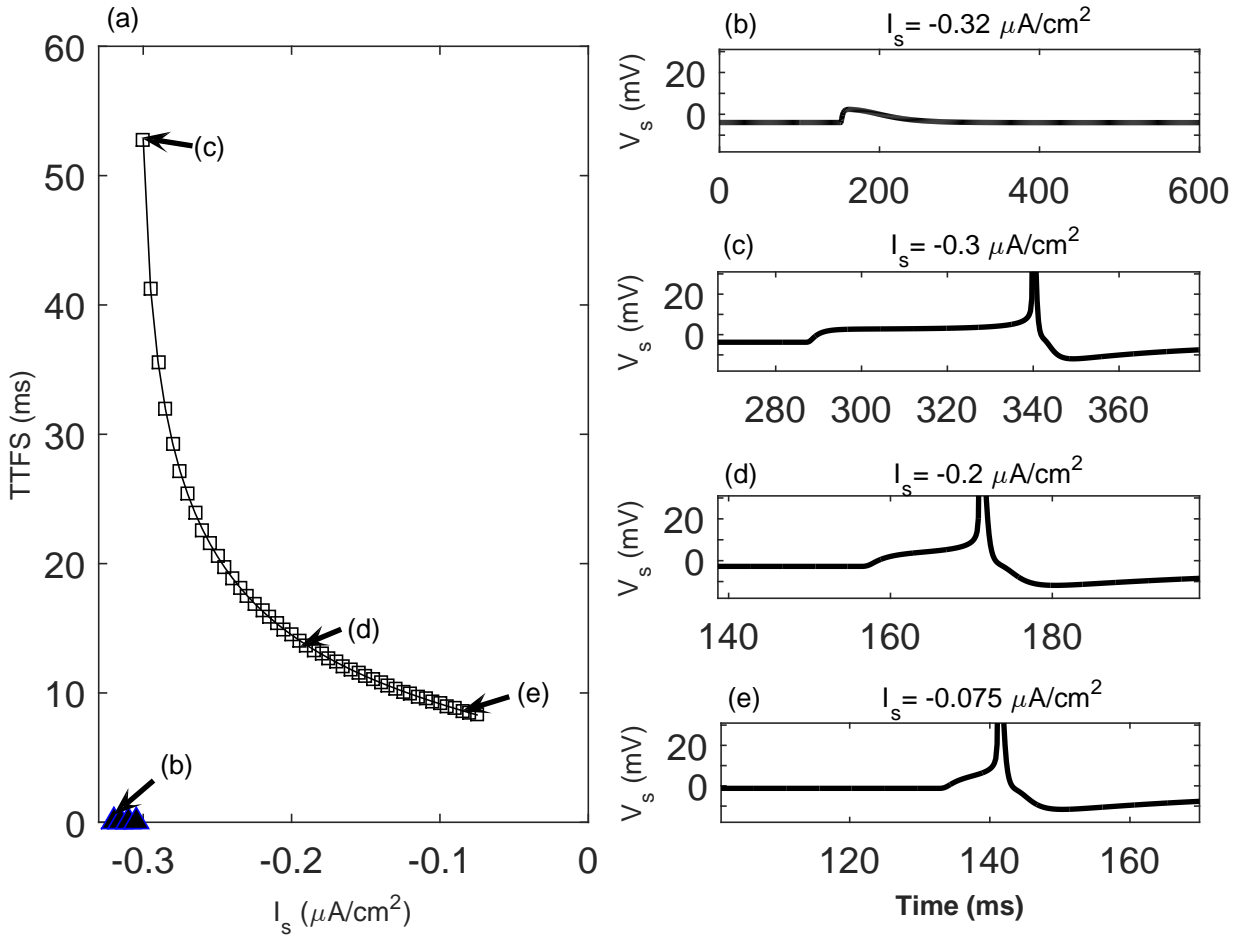


Figure 3.5: The TTFS down a synaptically (AMPA) connected chain as a function of excitability ( $I_s$ ) with no resistive lattice and thus no ECC. In (a) the black triangles (lying on the x-axis below  $I_s = -0.3 \mu\text{A}/\text{cm}^2$ ) denote failure to spike. The TTFS is seen to increase rapidly as  $I_s$  decreases to the threshold for spiking. In (b)-(e) we plot the somatic potential as a function of time for four different  $I_s$  values. In (b) for  $I_s = -0.32 \mu\text{A}/\text{cm}^2$ , the stimulation from the AMPA conductance ( $g_{\text{AMPA}} = 0.142 \text{ mS}/\text{cm}^2$ ) is not sufficient to elicit a spike. In (c)-(e) as the neurons become more excitable the period of latency —a prolonged period of almost constant membrane potential —shrinks. The TTFS here is actually the mean of the differences in consecutive spiking neurons in the chain. The differences in the computed time to pass through 30 mV is nearly identical down the chain (Fig. 3.4) as would be expected given that all PR neurons are identical and the synaptic connectivity is nearest-neighbor.

### 3.3.3 Sequentially excited architecture without extracellular resistance and Type I excitability.

Fig. 3.5 shows the TTFS as a function of  $I_s$  for fixed  $g_{AMPA}$ . As expected the TTFS increases with decreasing  $I_s$  and does so at an increasing rate (Fig. 3.5 (a)). At  $I_s = -0.32 \mu A/cm^2$  the inhibition is too strong and a spike is not generated (Fig. 3.5 (b)). In Fig. 3.5 (b-d) the TTFS increases with increasing inhibition. The increased TTFS is associated with a prolonged period at a near constant soma potential of around two mV (compare Fig. 3.4 (b)-(d)). We refer to this period of near constant membrane potential as a plateau potential, and it occurs near an unstable equilibrium where the dynamic flow approaches zero. This increasing spike latency is suggestive of a Type I neuron with an arbitrarily long period (see Introduction). This type of behavior is also characteristic of a loss of stability of equilibrium through a saddle-node bifurcation. Neuro-computationally, the significance is that the long latency allows for the encoding of small changes, such as the oscillating pulse in the membrane potentials due to the ECC from the action potential of a neighboring neuron (Fig. 3.3). In contrast, a Type II neuron will have a maximum TTFS that may not provide the dynamic range to differentiate such small differences in input.

We approach the complex dynamics of the eight-dimensional PR neuron by first asserting that the dendritic compartment remains mostly passive, and the interesting dynamics occur in the somatic compartment. We project the trajectories of the eight-dimensional model onto the  $V_s - n$  plane. By doing this for a number of initial conditions using the same parameter set we may observe stable and unstable points, or limit cycles. If the trajectories in the  $V_s - n$  plane are qualitatively different when we change a parameter value, then we have a strong suspicion that a bifurcation has occurred. As mentioned, the saddle-node on the invariant circle (SNIC) bifurcation has been associated with very long spike latency and arbitrarily long periods. A SNIC bifurcation implies that as a parameter varies two saddle-node equilibrium (one stable and one unstable) approach and annihilate one another. It is an invariant circle because both equilibrium are heteroclinic trajectories connecting the stable and unstable nodes. At the SNIC bifurcation, the two nodes vanish leaving only a limit

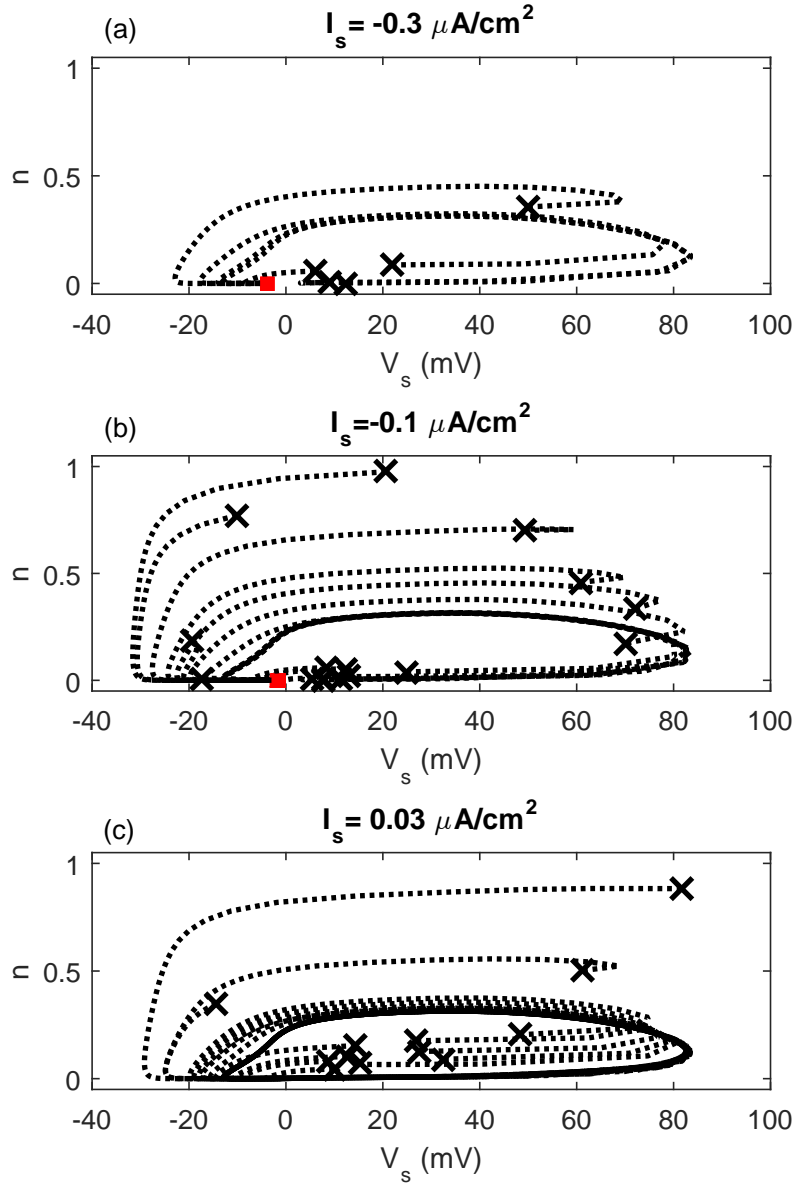


Figure 3.6: The flow of trajectories projected onto the  $V_s - n$  plane is characteristic of dynamics near a SNIC bifurcation. Shown are many different trajectories for three different  $I_s$ . X marks the beginning of a trajectory and in (a) and (b) the red square makes the stable equilibrium. The influence of the unstable equilibrium is evident in the divergent trajectories where for two nearby initial conditions one takes a more direct path towards the stable equilibrium and the other takes a more round about way. In (a) and (b), regardless of our initial conditions, all trajectories end at the stable equilibrium (red square). In (b) as  $I_s$  increases to  $-0.1 \mu\text{A}/\text{cm}^2$  the two equilibrium points approach each other. Then, in (c), for slightly positive  $I_s$  the two equilibrium have vanished and the unstable manifold has formed a limit cycle. All trajectories eventually lead to the limit cycle and the neuron spikes periodically.

cycle. When a neuron is at rest in the proximity of a saddle-node bifurcation on the invariant circle (SNIC), we would expect to see one stable and one unstable equilibrium. Then as we approach the bifurcation, the two equilibria approach one another, eventually coalescing and annihilating each other at the bifurcation point. What remains is the unstable manifold that forms the periodic orbit.

We use the software XPPAUT [11] to help capture the changing flow of trajectories as our model solution passes from resting to periodically spiking. In Fig. 3.6 we sample the initial conditions for the PR model at three different levels of inhibition  $I_s$ . For both of the two most inhibited cases, the trajectories converge to a single stable equilibrium (a and b) while the least inhibited results in periodic spikes (c). In (a) and (b) the region about  $V_s = 0$  mV and  $n=0$  is near both a stable and unstable equilibrium. In (a) and (b), the stable equilibrium occurs at the lower membrane potential. In (b) we see the gap close and then in (c) there are no remaining equilibrium and all trajectories eventually fall onto the limit cycle and spike periodically. This observation, the identification of a characteristic flow associated with a SNIC bifurcation, is dependent on our parameter values and is observed here for normal potassium levels and no polarization. In this work, we treat the small transient polarization due to the ECC as a parameter with no other polarization. Changes in  $E_K$  and the polarization could potentially move the dynamics away from the SNIC bifurcation and towards the influence of some other bifurcation and thus change the characteristic excitability.

### 3.3.4 Sequentially excited architecture with resistive lattice.

As explained in the introduction, data on the extracellular resistance in the hippocampus is sparse and the values that have been obtained, either directly or indirectly, have varied substantially. Here, we treat the extracellular resistance as a free parameter. However, to establish a point of reference we define the resistances used in the one-dimensional lattice of Gluckman and Park [6–8] as *standard*. How these *standard* resistances relate to physiological states of either slice preparations or in-vivo experiments, remains to be determined.

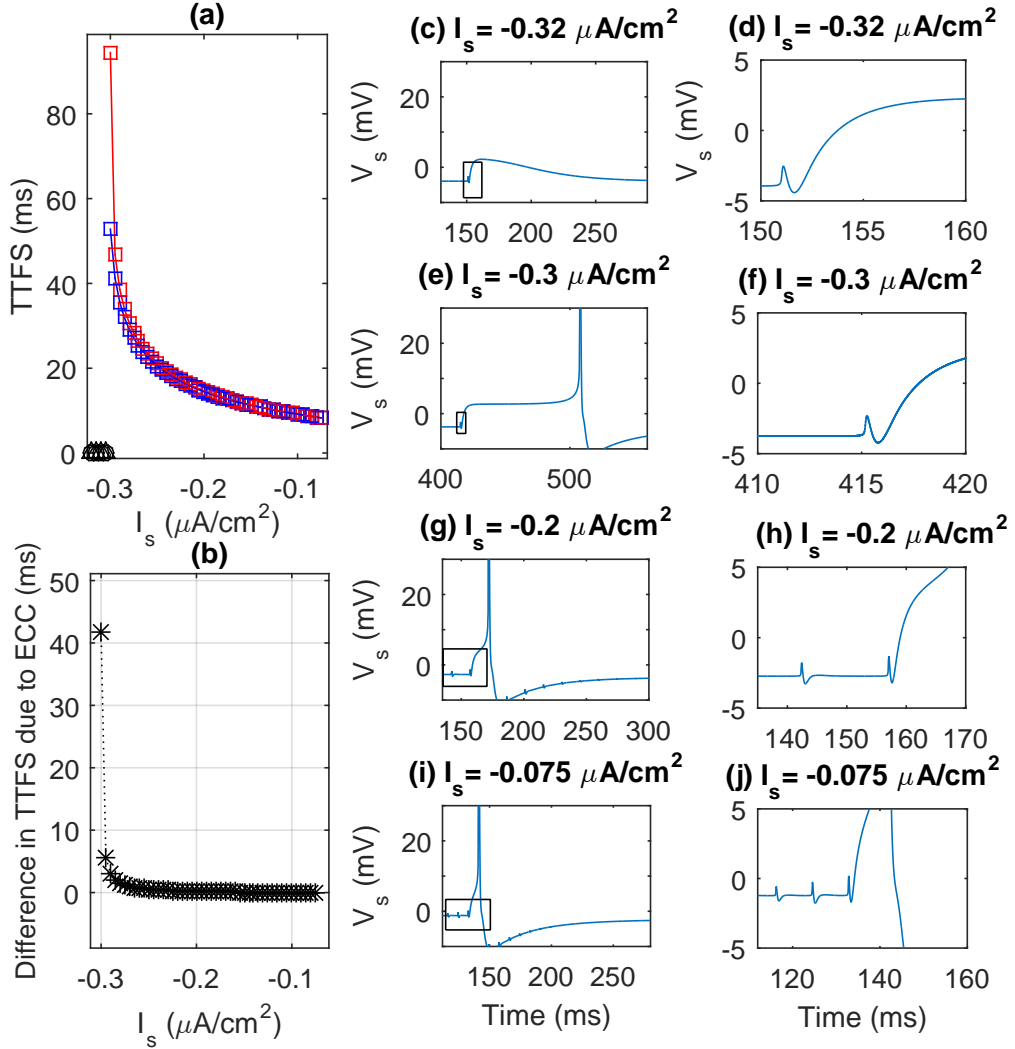


Figure 3.7: Far from the threshold to non-spiking the sequentially excited (SE) architecture has the same TTFs with or without the resistive array. Whereas, very near to the threshold the SE with resistive array has a higher TTFs and right at the threshold it has a much higher TTFs. This is shown in (a) where the average TTFs as a function of excitability,  $I_s$ , with (red squares) and without (blue squares) the resistive array are plotted. The black triangle on the x-axis denotes failure to spike. In (b) we plot the difference in TTFs with and without the resistive array. In this figure, the resistive array is set to *standard* values (see Methods) and here and for all computations we use  $g_{\text{AMPA}} = 0.142 \mu\text{A}/\text{cm}^2$ . The addition of the resistive array and thus the ECC has an inhibitory effect on the SE architecture. For the SE, the timing of the ECC from the action potential is always fixed and precedes the synaptic current by  $\approx 0.2$  ms. In (c),(e),(g),and (i)  $V_s$  is plotted showing the response to the pre-synaptic spike. (d),(f),(h), and (j) show the same computations but are zoomed in to highlight the effects of the ECC. In (c) and (d), we have spike failure. (e), (g), and (i) demonstrate the characteristic latency associated with the excited PR neurons near the critical point of spike failure. This property of latency is present with or without the ECC. In (h) and (j), we can see not only the ECC from the pre-synaptic neuron but also from the preceding spiking neurons.

To model the dependence of the spike propagation on extracellular resistance we began by computing the propagation of synaptic (AMPA) spikes down a chain of neurons using the sequentially excited network with and without resistance (see Methods and Fig. 3.2 for schematic diagram).

Spike propagation in the resistively embedded, sequentially excited network, is shown in Fig. 3.7 for the *standard* resistances and a range of  $I_s$ . For all  $I_s$ , the inclusion of the resistive lattice retards the TTFS (see Fig. 3.7 a and b). As we saw previously (Fig. 3.5) the increase in TTFS with  $I_s$  is steep as we near the threshold to spike. Fig. 3.7 (c-j) plots somatic potential over time for four different  $I_s$ . Plots (c,e,g, and i) highlight the increased spike latency with increased inhibition. Plots (d,f,h, and j) are zoomed in views of plots (c,e,g, and i) respectively, to resolve the small pulses of oscillatory somatic membrane potential associated with the action potential of neighboring neurons.

**The relative timing between the ECC due to neighboring action potentials and the synaptic AMPA current.**

Fig. 3.8 shows the somatic potential (solid, plotted against the right y-axis), the AMPA current (dots), and the inter-compartment current (dash-dot) due to the induced polarization,  $V_{ds}^{out}$ , for three different values of the extracellular resistance along the somatic-dendritic axis,  $R_{ds}^{out}$ . For the sequentially excited networks, the relative timing between the ECC and the AMPA is fixed, with the soma-depolarizing phase of the ECC starting slightly ( $\approx 0.2$  ms) before the AMPA current. The amplitude of the ECC due to the neighboring action potential is monotonically increasing with increased  $R_{ds}^{out}$  while the AMPA current is unaffected by  $R_{ds}^{out}$ . Although the amplitude of the  $V_{ds}^{out}$  increases from (a) to (c) the resulting TTFS is nearly equal at the low and high  $R_{ds}^{out}$  values and is greatest at the intermediate  $R_{ds}^{out}$  (b) (TTFS not visible in figure). The reason for this unimodal behavior (seen more clearly in Fig. 3.10) is explained in the remaining chapter.

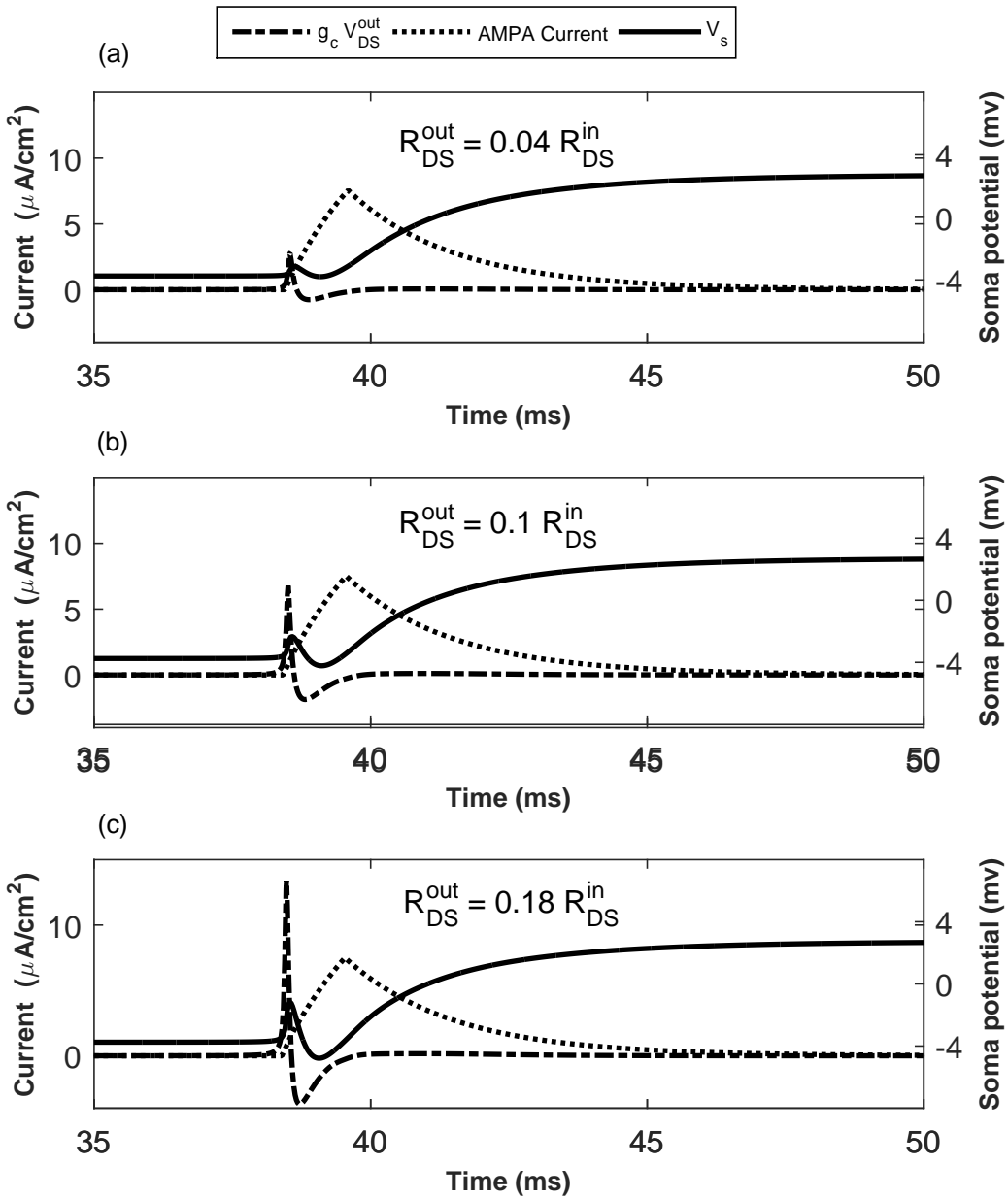


Figure 3.8: Shown in (a)-(c) are the inter-compartment currents,  $g_c V_{ds}^{out}$  (dash-dot), the AMPA current (dots), and the soma membrane potential,  $V_s$  (solid), for three different values of  $R_{ds}^{out}$ . For each  $R_{ds}^{out}$  the polarization and its current increase in amplitude for increased resistance but the purely resistive lattice maintains the waveform. It is not immediately obvious how the ECC and its resulting polarization effects the TTFS. For example (a) and (c) result in practically the same TTFS even though the amplitude of the polarization current differs by at least a factor of four. The explanation of these effects is the primary subject of the remaining chapter.

### **Response of the lattice to trans-membrane current: R-V curves,**

We can understand how the current flows in the resistive lattice by simply replacing the neurons with constant current sources. Fig. 3.9 (a) shows how the polarization from constant currents  $I_d^{tot}$  and  $I_s^{tot}$  varies with  $R_{ds}^{out}$  and position from the source. The polarization is monotonically increasing for increasing  $R_{ds}^{out}$ . For the constant injected currents we use  $I_d^{tot} = 0.4 \text{ nA}$  and  $I_s^{tot} = 0 \text{ nA}$  which may be placed into context by Fig. 3.9 (b). In (b) we plot the transmembrane currents from both the dendritic and somatic compartments during a single action potential.

### **Sensitivity of TTFS to extracellular resistance.**

The TTFS for the resistively embedded SE architecture is unimodal with respect to resistance along the somatic-dendritic axis,  $R_{ds}^{out}$ . Fig. 3.10(a) plots the TTFS as a function of  $R_{ds}^{out}$  for a series of  $I_s$  values. As might be expected the sensitivity to  $R_{ds}^{out}$  increases the lower  $I_s$  and the closer the neuron is to the threshold for firing. As noted above the unimodal profile is somewhat surprising and much of the remaining chapter is dedicated to explaining this and the mechanisms behind the observed dependence of spike timing on ECC. Fig. 3.10(a) is unimodal with respect to  $R_{ds}^{out}$  even though we saw in Fig. 3.9 that the amplitude of the polarization is monotonically increasing with  $R_{ds}^{out}$ . Thus, the effects of the localized ephaptic ECC are increasingly inhibitory for increasing  $R_{ds}^{out}$  and increasing polarization current up until a certain point, after which, continually increasing the  $R_{ds}^{out}$  and polarization amplitude now increases the excitability. The unimodal profile disappears with the removal of neuron-to-neuron resistors (Fig. 3.11).

#### **3.3.5 Initial observations on how the ECC effects TTFS.**

We divide the total localized ephaptic effect into three components: (1) source loading, (2) the response of non-synaptic membrane currents of neighboring neurons and (3) synaptic coupling. The source loading component depends on both non-synaptic membrane currents

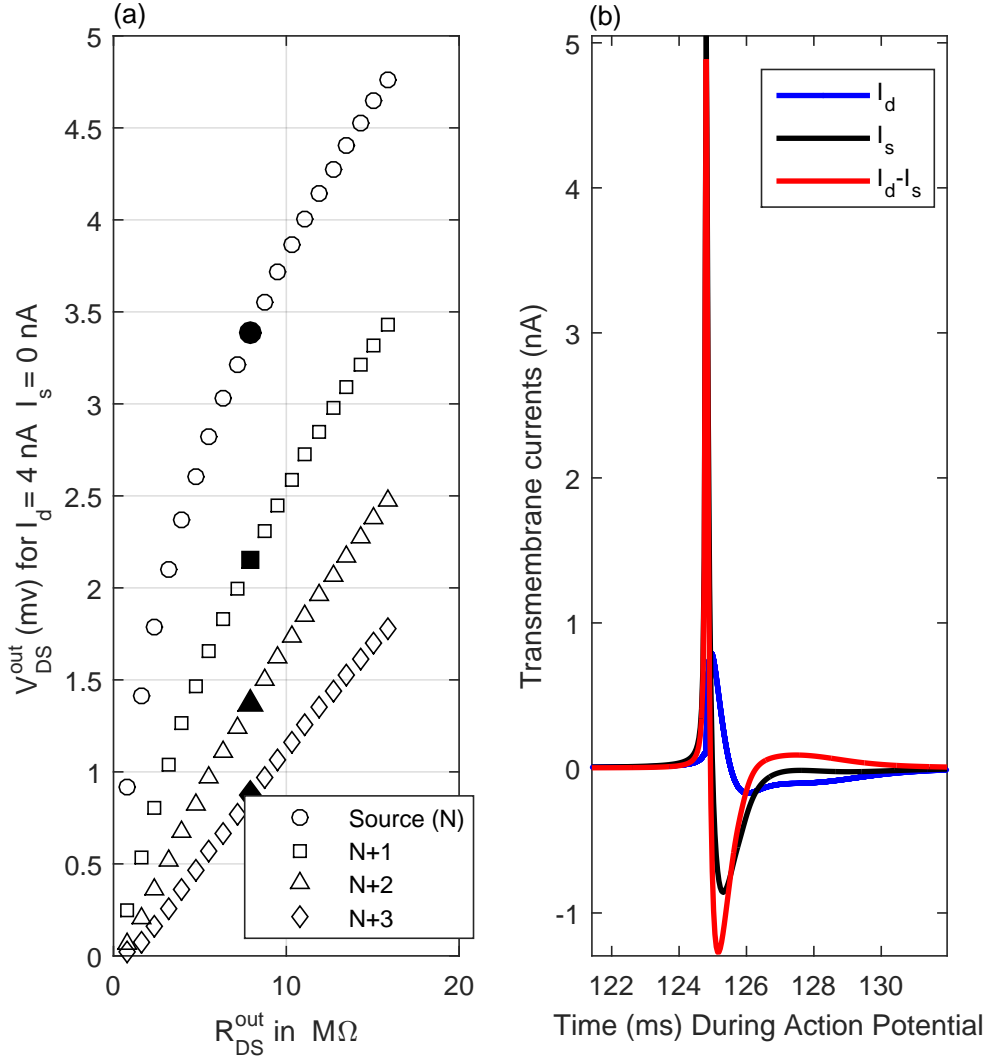


Figure 3.9: (a) Shows the response of the resistive lattice (no neurons) as a function of  $R_{ds}^{out}$ . The transmembrane currents are replaced by constant currents at the junctions where the somatic and dendritic compartments would be. In this case  $I_d = 4$  nA and  $I_s = 0$  nA so that there is 4 nA of current flowing outside the source neuron from the dendrite to the soma. Shown are the polarizations at the source and the next three posts in the chain. Polarization is symmetric around the source neuron (i.e.  $V_{ds}^{out}(N+x) = V_{ds}^{out}(N-x)$ ). In all cases the neuron-neuron resistances are fixed to the *standard* values ( $R_{dd} = R_{ss} = 0.01R_{ds}^{in}$ ). Filled symbols denote *standard* resistance values of  $R_{ds}^{out}$ . The monotonicity persists over increased  $R_{ds}^{out}$  and increased neural distance from source. (b) We consider the transmembrane currents during an action potential for a single neuron by plotting  $I_s$  (black),  $I_d$  (blue) and  $I_d - I_s$  (red). Notice that the constant 4 nA current used in (a) is only exceeded for a fraction of a millisecond

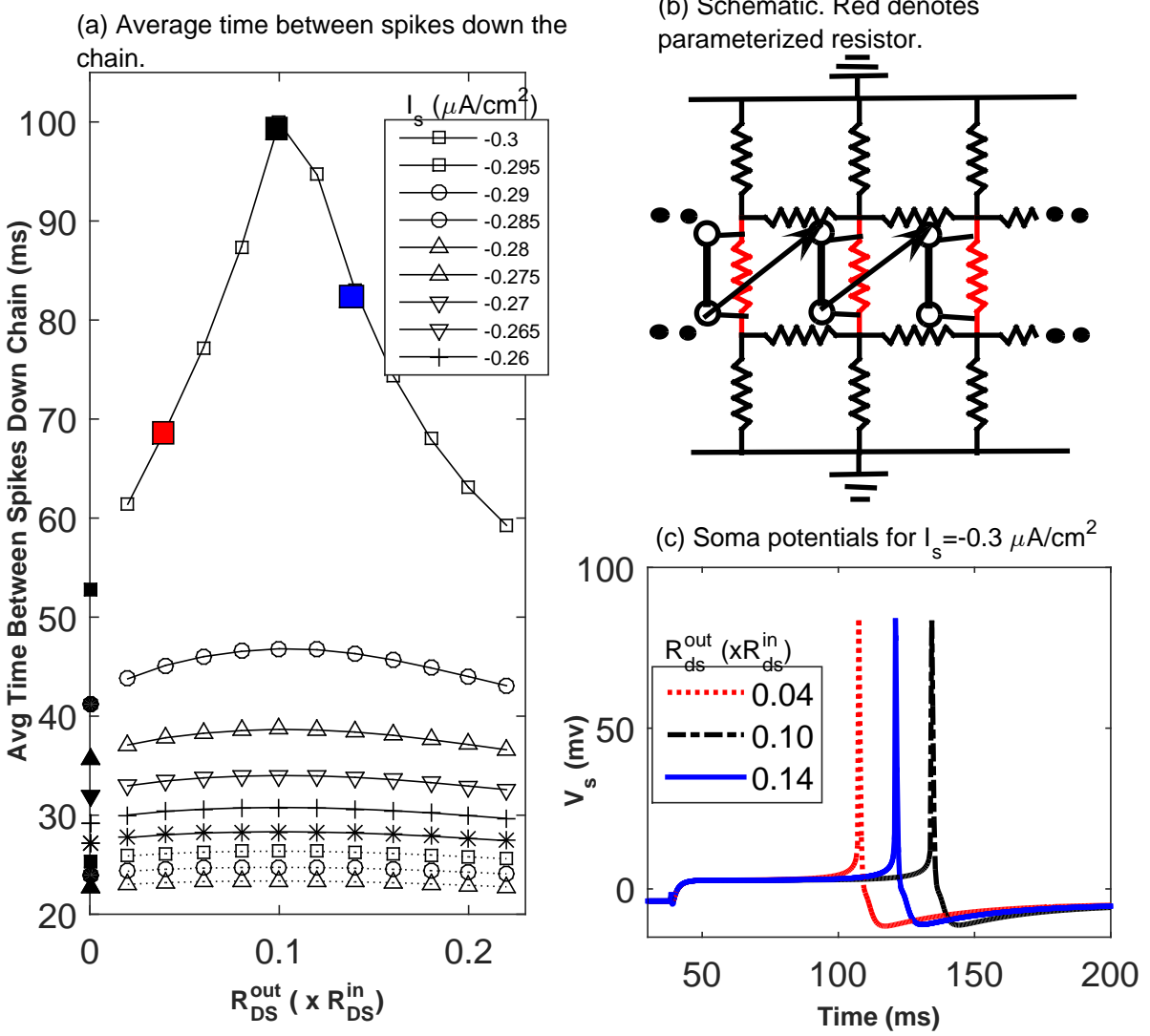


Figure 3.10: For the SE architecture with a resistive array the TTFS is unimodal with increasing resistance along the soma-dendrite axis,  $R_{ds}^{out}$ . In (a) we plot the mean time between spikes as  $R_{ds}^{out}$  is varied for a range of  $I_s$ . As expected the higher  $I_s$  and the more intrinsically excitable the neurons are, the less noticeable the effect of the extracellular resistance. Interestingly, the TTFS has a peak at about the *standard* resistance values. The filled symbols on the left y-axis at  $R_{ds}^{out} = 0.1R_{ds}^{in}$  are the TTFS for the SE architecture with no resistive lattice. In (b) we draw a schematic for the scenario used in the figure. The resistance in red denotes that these values are varied over the range along the x-axis of (a). In this picture, the soma lies beneath the dendrite and the arrows denote that the presynaptic soma triggers the AMPA current in the postsynaptic dendrite. Above we only vary the  $R_{ds}^{out}$  fixing the resistances connecting neuron to neuron to their *standard* values of  $0.01 R_{ds}^{out}$ . In (c) we plot  $V_s$  versus time for three  $R_{ds}^{out}$  at  $I_s = -0.30 \mu A/cm^2$  and correspond to the squares of like colors in (a). As  $R_{ds}^{out}$  increases, the resulting time-varying polarization,  $V_{ds}^{out}$  due to the action potential associated ECC increases in amplitude while maintaining its shape (Fig. 3.3). The effect of this monotonically increasing polarization amplitude on the TTFS is, however, not monotonic and the reasons for this will become clear through the work that follows.

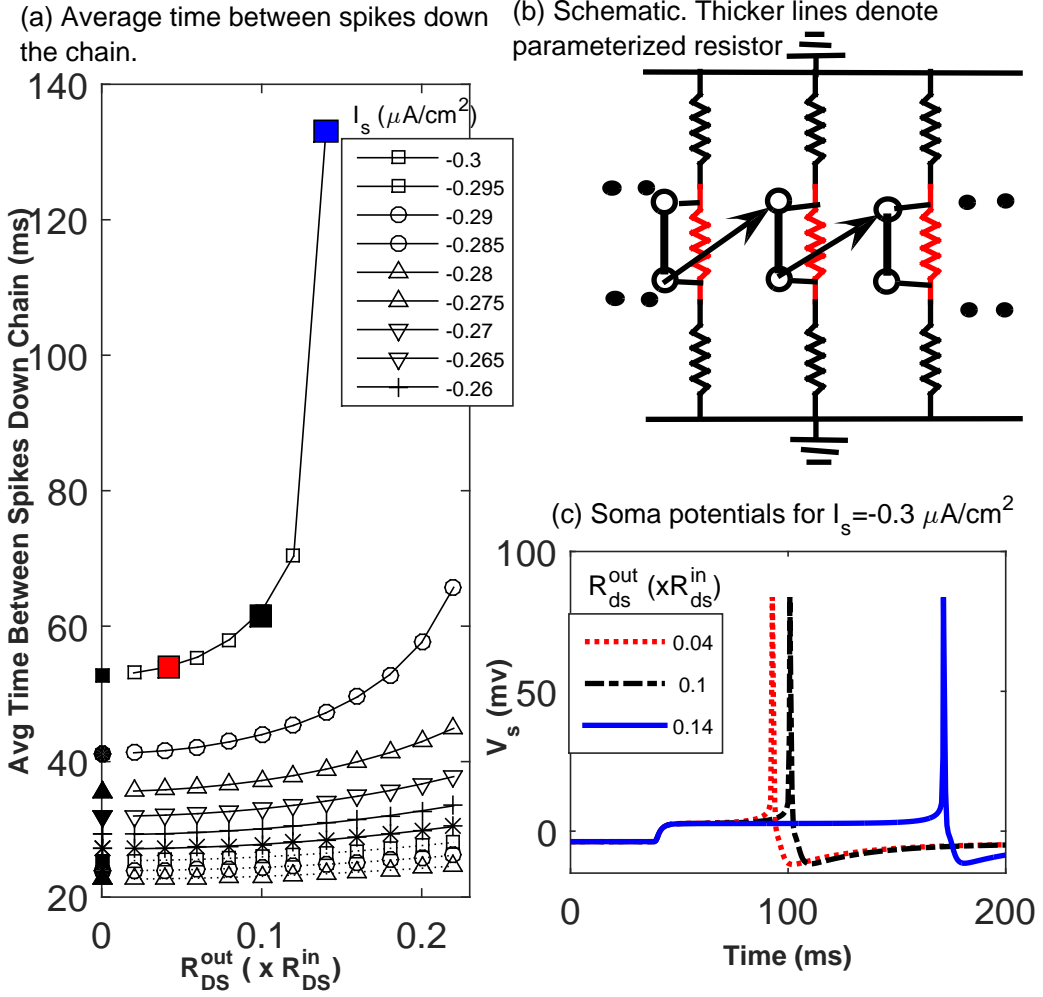


Figure 3.11: With the neuron-to-neuron resistances removed the TTFS with respect to  $R_{ds}^{out}$  is monotonically increasing. (a) plots TTFS as a function of  $R_{ds}^{out}$  for a range of  $I_s$ . The filled symbols along the left y-axis are the TTFS for no resistive lattice. (b) shows a schematic for the scenario in this figure. Notice the complete absence of neuron-to-neuron resistance and thus, no neuron-to-neuron flow of ECC. The only effect the extracellular currents of each neuron has is due to self-polarization (referred to as source loading in the Introduction). In (c) we plot  $V_s$  versus time for the same three  $R_{ds}^{out}$  values sampled in Fig. 3.10 and correspond to the squares of like colors in (a). We conclude that the source loading component of the ephaptic effect is inhibitory and from Fig. 3.10 the remaining synaptic coupling and/or the non-synaptic membrane currents must have an excitatory component.

and synaptic coupling but serves to make the distinction between the effects of ECC due to other neurons and those that are self-generated. Since all of these components are coupled physiologically as well as in the model's ODE, we employed various modifications to tease out their relative contributions. These modifications included: disconnecting the neuron-neuron resistance and utilizing linearly interpolated functions based on the polarization and AMPA currents in the embedded chain.

### **Effects of source loading in the SE Architecture**

By severing the conductivity between neurons, we eliminate the neuron-neuron interactions. In this way, we isolate the effects of the ECC on a neurons TTFS due to that own neurons transmembrane currents. We refer to this type of effect as source loading. The situation is depicted in Fig. 3.11(b) and the TTFS as a function of  $R_{ds}^{out}$  for various levels of inhibition are plotted in Fig. 3.11(a). For all levels of inhibition the TTFS increases with increasing  $R_{ds}^{out}$  (and increasing polarization amplitude). We thus consider the source loading to be inhibitory. There are only two transmembrane events that generate significant ECC. One corresponds to the injection of synaptic AMPA to the dendrite and the other is the action potential. Without extracellular resistance and thus without polarization the AMPA current delivered to the post-synaptic dendrite is proportional to the post-synaptic  $V_d$ . As the dendrite is depolarized this synaptic drive diminishes the total AMPA current delivered. With extracellular resistance the internal polarization current further depolarizes the post synaptic dendrite and thus further diminishes the total AMPA current. This effect is a form of synaptic coupling which takes on a greater role, as discussed below, when coupled with the ECC due to neighboring action potentials. For source loading the synaptic coupling due to the polarization induced by the depolarizing AMPA current is small compared to that which occurs when the synaptic drive is coupled to the AP generated ECC. The other effect is the induced polarization due to the action potential. The TTFS is defined when  $V_s$  first passes through 30 mV. This phase of the action potential is dominated by the rush of depolarizing  $Na^+$  atoms into the soma. Such a strong depolarizing somatic current would only enhance

further depolarization of the soma through the intercompartmental current and would thus be slightly excitatory. Neither of these effects explain the increasing inhibitory effect on the neuron with increasing  $R_{ds}^{out}$ .

To explain the inhibitory effect we need to look at how the polarization effects the spike width and thus the total AMPA current delivered to the neighboring neuron. Fig. 3.12 (a) plots  $V_s$  and  $V_{ds}^{out}$  for individually polarized neurons as depicted in Fig. 3.11. In this case the ECC currents that induce the polarization are entirely self-generated. The plot displays three  $V_s$  and  $V_{ds}^{out}$  pairs for three  $R_{ds}^{out}$  for  $I_s = -0.3\mu A/cm^2$  shown in Fig. 3.11 (a). This plot shows the growing amplitude of the polarization and the fact that the positive  $V_{ds}^{out}$  occurrence during the leading sodium depolarizing phase followed by a negative  $V_{ds}^{out}$  as the soma membrane potential repolarizes. The polarization current during the repolarization has the effect of further hyperpolarizing the soma and thus brings the somatic potential down below the threshold for AMPA conductance slightly sooner. The result of this can be seen in Fig. 3.12 (b) where we plot spike width versus  $R_{ds}^{out}$ . Although the spike width decreases only about two-percent over the range of resistances this results in significant differences in TTFS especially near the threshold to failure to spike.

### The effect of coupling between the ECC and synaptic AMPA

In the sequentially excited architecture, the time between the ECC and the AMPA current is fixed and is shown in Fig. 3.8. We see that for this relative timing the ECC associated with a neighboring neurons' action potential is significant only for the beginning portion of the rising slope of the AMPA current. The AMPA current is proportional to the potential difference between the post-synaptic dendritic potential and a reversal potential. Thus, for a given level of synaptic conductance,  $W$ , the current into the dendrite is reduced by depolarization and increased by hyperpolarization of the postsynaptic dendrite. In the case of the SE architecture, the dendrite depolarizing phase of the ECC coincides with the higher levels of synaptic conductance. Thus, for the SE architecture, the inhibitory effect of the ECC-AMPA coupling outweighs the excitatory effect due to the hyperpolarizing phase of

the ECC. Further, we see from Fig. 3.8 that the inhibitory effect of the ECC on the AMPA current is amplified with increasing polarization due to increasing  $R_{ds}^{out}$ . The fact that both source loading and the synaptic drive are inhibitory and Fig. 3.10 is unimodal implies that the response of the non-synaptic membrane currents of neighboring neurons must have an overall excitatory effect, at least for the SE architecture.

### **Non-synaptic membrane currents and their response to action potential generated ECC.**

The ECC from an isolated potential spike lasts only several milliseconds (Fig. 3.3). In the cell, response to such a high-frequency pulse would depend on currents with fast membrane time constants and ion-channel kinetics. The depolarizing sodium current of the Soma has a fast membrane time constant and very fast channel kinetics. In fact, the sodium gating channel kinetics in the PR model are assumed instantaneous. Fig. 3.13 shows the response of the non-synaptic membrane currents to the polarization induced by a neighboring neurons' action potential. The response of the sodium current is clearly more pronounced than for the other non-synaptic membrane currents.

### **The contributions of synaptic coupling and non-synaptic membrane currents to the localized ephaptic effect and their dependence on extracellular resistance.**

As detailed in the Methods section we estimate the contributions of the coupled non-synaptic membrane currents and synaptic coupling by integrating the currents for the range of  $R_{ds}^{out}$ . Specifically, we integrate over the non-synaptic currents in response to a full lattice model with no synaptic connectivity. Here we stimulate one neuron to spike then see how the currents react. This is exactly the situation shown in Fig. 3.13 (a) and here we integrate each of the currents for each  $R_{ds}^{out}$ . The result is shown in Fig. 3.14 (a). Here, each data point for each current is the integrated current density or charge density for a given extracellular resistance,  $R_{ds}^{out}$ . We see that the leading contribution comes from the sodium current and that while there are hyperpolarizing currents the total active charge density

is positive. The total net charge will, of course, be zero as the neuron starts from rest and ends at rest. However, the passive leak currents act so slowly as to be insignificant in the course of synaptic AMPA current. Importantly the increase in the active non-synaptic currents with  $R_{ds}^{out}$  is superlinear. In Fig. 3.14 (b) to quantify the contribution of synaptic coupling we integrate over the dendritic membrane potential dependent part of the AMPA conductance,  $-g_{AMPA}W(t)V_d$ . Here it is impossible to separate the synaptic effects from the non-synaptic current effects as they each affect one another. However, we can compute how the synaptic effect grows with increasing  $R_{ds}^{out}$ . As we have mentioned, for the SE architecture the net effect of the synaptic coupling is inhibitory and in (b) we show that the inhibition increases linearly with increasing  $R_{ds}^{out}$ . We are now prepared to explain the non-monotonicity found in Fig. 3.10 (a). At low resistances the TTFS is increasing with increasing  $R_{ds}^{out}$  and thus the increased polarization is inhibitory. At these resistances the inhibitory synaptic coupling dominates the excitatory response of the non-synaptic currents. For further increasing resistances the TTFS decreases. In this case, the non-synaptic currents, whose conductances generally increase nonlinearly, start dominating over the inhibitory synaptic coupling effect.

### 3.3.6 Generalization of AP related ephaptic effects using single-neuron models.

As detailed in Sec. 3.2.5 we utilize two single-neuron models solved using XPPAUT to explore how changes in timing and amplitude of the induced polarization effects the excitability. In both models, we represent the polarization,  $V_{ds}^{out}$ , as an interpolated function that may be applied freely at any time and strength. In the second single-neuron model, we also represent the AMPA current by an interpolated function. With these simplified models, we re-affirm our conclusions drawn from the sequentially excited network, generalize them to pertain to a wider range of synaptic architectures, and further clarify the role of the different components of localized ephaptic effects.

Using the single-neuron model with interpolated  $V_{ds}^{out}$  we computed TTFS for a range of

$\tau$ , defined as the difference in time between the ECC and AMPA, as well as the amplitude of the polarization, defined as Amp (see Methods). The excitability profile is shown in Fig. 3.15 as a function of  $\tau$  and Amp. To help visualize the parameters  $\tau$  and Amp we provided plots along the y and x axis to show the relative timing and polarization amplitude respectively. We point out two features: (1) An interval around  $\tau = 0$  ms of increasing TTFS surrounded by regions of higher excitability. (2) With the exception of the interval around  $\tau = 0$  ms the TTFS decreases with increasing Amp. In Fig. 3.16 we look at alternate views of the same data as in Fig. 3.15. In (a) of Fig. 3.16 we show a projection of the three-dimensional TTFS versus  $\tau$  and Amp data. In (b) we show five series of points for  $\tau$  about  $\tau^*$  as a function of polarization amplitude, Amp. In (c) for Amp=1 (corresponding to  $R_{ds}^{out} = 0.1R_{ds}^{in}$ ) we see how TTFS varies with  $\tau$ . Figs. 3.15 and 3.16 are the result of a single neuron model equipped with a polarization term  $V_{ds}^{out}$  for which we apply an interpolating function based on the polarization felt by a neuron in the full resistive lattice due to the action potential of a neighboring neuron. As in the resistive lattice models the spike is driven by an AMPA synaptic current which couples to the ECC via the post-synaptic dendritic membrane potential. Unlike the resistive lattice models, however, there is no source loading due to self-polarization or feedback between the neurons own transmembrane currents and the extracellular space. So for this single-neuron model the localized ephaptic effects are limited to synaptic coupling and non-synaptic currents due only to the polarization matching the shape of that induced by the action potential of a nearest-neighbor. In Fig. 3.15 and Fig. 3.16 (a) and (c) the response due to  $\tau$  reflects the effect of the varying overlap between the bi-phasic  $V_{ds}^{out}$  which alternately hyperpolarizes then depolarizes the dendrite. This effect can either enhance or diminish the total flow of AMPA current into the post-synaptic dendrite and thus decrease or increase the TTFS. For  $\tau$  greater than about 4 ms the ECC polarization ceases to overlap with the AMPA current and dependence on  $\tau$  and synaptic coupling is eliminated. Outside of the parabolic TTFS profile due to synaptic coupling the TTFS is monotonically decreasing with increasing Amp. This response to increasing Amp must then be due to effects of the non-synaptic membrane currents. A key

part of the non-synaptic membrane currents is the voltage dependent conductance of the ion-specific channels. As mentioned  $V_{ds}^{out}$  does not directly add current to the neuron and if the compartments were totally passive then internal current would flow back and forth between the compartments for several ms but then would quickly equilibrate. With voltage dependent conductances however the oscillating internal current could momentarily raise the membrane potential and thus change the conductance and allow more total current to flow into the neuron.

In our second single-neuron model we eliminate synaptic coupling by using an interpolating function of AMPA without any dependence on the post-synaptic dendritic potential. The absence of the synaptic coupling is immediately evident in Fig. 3.17, The only response to the interpolated polarization is through the non-synaptic membrane currents. This particular model is most like the Hippocampal slice experiments when all synaptic current is blocked. Since in those experimental models we would expect the ephaptic effects to be dominated by non-synaptic membrane currents. Here as in Qiu [50] we see increasing spike propagation speed (decreasing TTFS) with increasing Amp (and increasing  $R_{ds}^{out}$ ). We can now see that the region of increased excitability that surrounded the parabolic increase in TTFS was not due to synaptic coupling but due to non-synaptic membrane currents. That there is an increased sensitivity to the polarization around  $\tau = 0$  ms may be explained that the effect of added internal current on potential-dependent conductances will have greater effect when coupled with the peak of the AMPA current.

In Fig. 3.18 we take different views of the same data shown in Fig. 3.17. In (b) as we did for the first single-neuron model for several fixed values of  $\tau$  around  $\tau^*$  we plot TTFS versus Amp. Clearly, the response of the non-synaptic currents to increasing Amp is excitatory and, in this region, linear. In (c) for Amp=1 (and  $R_{ds}^{out} = 0.1R_{ds}^{in}$ ) we see that the ephaptic effect due to non-synaptic membrane currents is most excitable near  $\tau^*$  which from the figures on the y-axis of Fig. 3.17 occurs when the peak of the AMPA current and the peak of the polarization coincide.

We can now identify the mechanisms behind the non-monotonic TTFS profile with

increasing  $R_{ds}^{out}$  seen in Fig. 3.10 for the full lattice model. In Fig. 3.16 (b) for  $\tau$  around  $\tau^*$  the TTFS does exhibit a non-monotonic relationship with increasing Amp. However, this effect is not pronounced as the total change in TTFS is less than 0.2 ms. This single-neuron model has both synaptic coupling which is inhibitory for  $\tau$  about  $\tau^*$  and non-synaptic membrane current effects which from our second single-neuron model we know to be clearly excitatory with increasing Amp. We conclude that in the full model at  $\tau = \tau^*$  there is both an inhibitory effect due to the synaptic coupling and an excitatory effect due to the non-synaptic membrane currents. For smaller values of Amp and  $R_{ds}^{out}$  the inhibitory synaptic coupling dominates, however, as  $R_{ds}^{out}$  increases further the excitatory effect of the non-synaptic membrane currents becomes greater than the inhibitory synaptic coupling effect. That the strength of the synaptic coupling and non-synaptic membrane currents would grow at different rate is not surprising since the synaptic coupling is linearly dependent on membrane potential while active currents, such as the sodium current, have a nonlinear (superlinear) dependence on membrane potential. It is also apparent that the SE architecture resulted in a rather special  $\tau$  and that synaptic time delays and more complex synaptic architectures may make it difficult to experimentally observe the non-monotonicity in Fig. 3.10.

### 3.3.7 Effects of the ECC associated with a randomly spiking, synaptically isolated, neuron on spike-timing.

We now consider a randomly spiking and synaptically isolated PR neuron along with a chain of PR neurons embedded in a resistive lattice. A schematic diagram of the scenario is drawn in Fig. 3.19 (a). In the figure the synaptically isolated neuron,  $I_1$ , is colored blue and is sandwiched between  $C_1$  and  $C_2$  of a six neuron ( $C_0 - C_5$ ) SE network. After stimulating  $C_0$  to spike  $C_1 - C_5$  spike sequentially as depicted in the timeline.

In (b) and (c) of Fig. 3.19 the same unimodal profile of TTFS as a function of  $R_{ds}^{out}$  is evident with a peak at the *standard*  $R_{ds}^{out} = 0.1 R_{ds}^{in}$ . These plots are very low resolution in the sense that  $I_1^*$  was stepped in 2 ms increments, which is too large of a step size to

capture the detail seen in Fig. 3.16 (c), especially the parabolic feature found right around the peak of the AMPA current. A higher resolution plot is shown in Fig. 3.20 and shows the  $\tau_{ECC}$  dependence seen in Fig. 3.16 (a and c). Here, unlike in Fig. 3.16 (c), at the top of the parabolic profile the neuron fails to spike.

### 3.4 Discussion

We find that the excitability, as measured by the TTFS, is non-monotonic with respect to increasing resistance along the somatic-dendritic axis. The non-monotonicity occurs over a range of resistance values consistent with the variance in geometry and resistivity observed in and around pyramidal cells of the hippocampus. To further understand these surprising results we segregate the components of this nonlinear coupled ODE. We define three components of the localized ephaptic effects: (1) source loading; (2) synaptic coupling, and (3) nonsynaptic membrane currents. Source loading refers to the effects of a neurons' ECC on its spike generation. To isolate this effect, we simply removed the neuron-to-neuron resistors in the lattice. With only source-loading our computations showed that the neuron was increasingly inhibited with increasing  $R_{ds}^{out}$  Fig. 3.11. The coupling of the synaptic current and the ECC is through the dependency of the AMPA current on the membrane potential of the post-synaptic dendrite. Within two milliseconds The induced biphasic polarization current,  $g_c V_{ds}^{out}$ , first hyperpolarizes than depolarizes the dendrite. Meanwhile, the AMPA current first rises to its peak value in under 2 ms then begins a slow decay over about 7 ms. For the SE architecture, the relative timing is fixed (Fig. 3.8) and is inhibitory. Using the single-neuron model we see that the effect of the synaptic coupling depends on the relative timing parameterized by  $\tau_{ECC}$  Fig. 3.16 (c). The effect is inhibitory for about 2 ms until the ECC crests the peak of the AMPA at which point it becomes excitatory. Finally, we capture the contributions from the non-synaptic membrane currents by applying an interpolated function for the AMPA current as well as for the polarization

in a modified single-neuron model. Our results show that the contributions of the non-synaptic effects are excitatory with respect to increasing resistance and the closer in time the ECC is to the onset of the AMPA current Fig. 3.17. The explanation for the monotonic excitatory response can be largely attributed to the very fast kinetics of the depolarizing sodium current which drives an overall depolarizing non-synaptic current response. The dominance at higher extracellular resistance is due to the fact that the voltage-dependent gating channels increase superlinearly with increase membrane potential and thus increased  $R_{ds}^{out}$ .

Additional future work would include the effects of other synaptic currents. In particular, NMDA has a more complicated dependency on the post-synaptic dendritic membrane potential that results from the need for the postsynaptic neuron to knock out blocking  $Mg^{2+}$  ions [88]. It would also be interesting to see if other currents such as  $I_h$  would qualitatively change our results. Additional analysis would consider changes to the neuron-to-neuron resistances and frequency-dependent conductivity of the ECS. The fact that the soma-depolarizing phase of the ECC has higher frequency components than the hyperpolarizing phase should have interesting consequences when we consider frequency-dependent conductivity.

Perhaps the most interesting future work would involve extensions to the isolated spiking neuron simulations. In particular, a situation where a population of synaptically isolated neurons spike synchronously and are interspersed among a chain of neurons might be revealing. It is possible that these dynamics might be predicted and explained through repeated application of our response curves computed with the single-neuron model. Also, it would be interesting to extend this work using a three-dimensional lattice.

The effect of extracellular resistance on spike timing may have implications for certain neurological conditions, aging, and development [68, 81, 89]. Changes in tortuosity and volume fraction impacts the extracellular resistance. As we have noted some of these changes occur at the millisecond level while others appear to occur gradually with age or disease. *In vivo* measurements and computational modeling of the interstitial space is challenging

and is the subject of current research [90, 91]. The models used here should be revisited with the improved and expanded knowledge of the extracellular conduction.

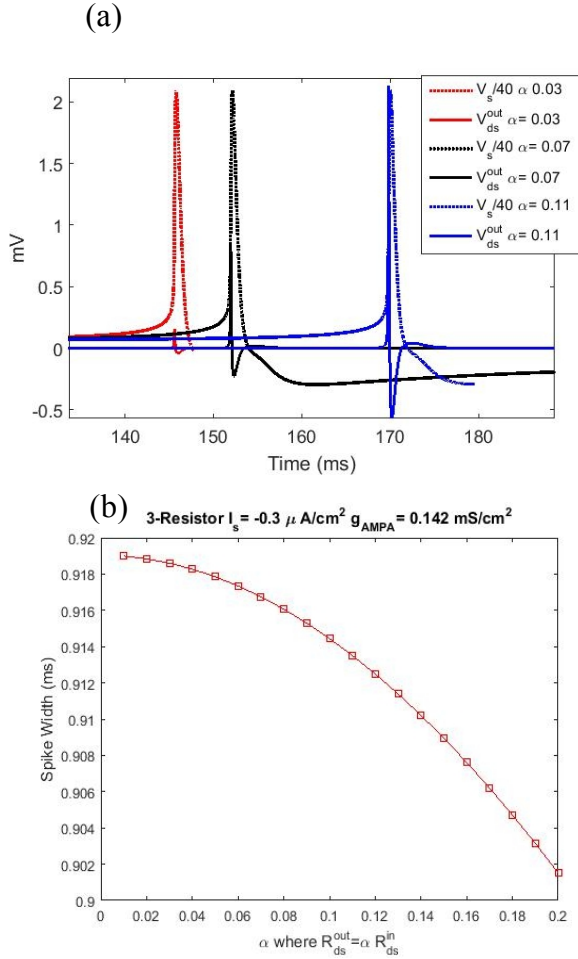


Figure 3.12: The case of no neuron-to-neuron resistance as depicted in Fig. 3.11 (b). Here we show the induced polarization  $V_{ds}^{out}$  (solid) and  $V_s$  (at 1/40th scale) (dotted) for three different  $R_{ds}^{out}$  due to a neurons own action potential in (a) and the resulting decrease in spike width in (b). The polarization current associated with the repolarization of the soma results in further hyperpolarization of the soma and subsequent shorter time above the threshold for AMPA conductance (20 mV). Although the difference in spike width is only several percent, near the threshold to failure to spike the slight difference in AMPA current can make substantial difference in the TTFS.

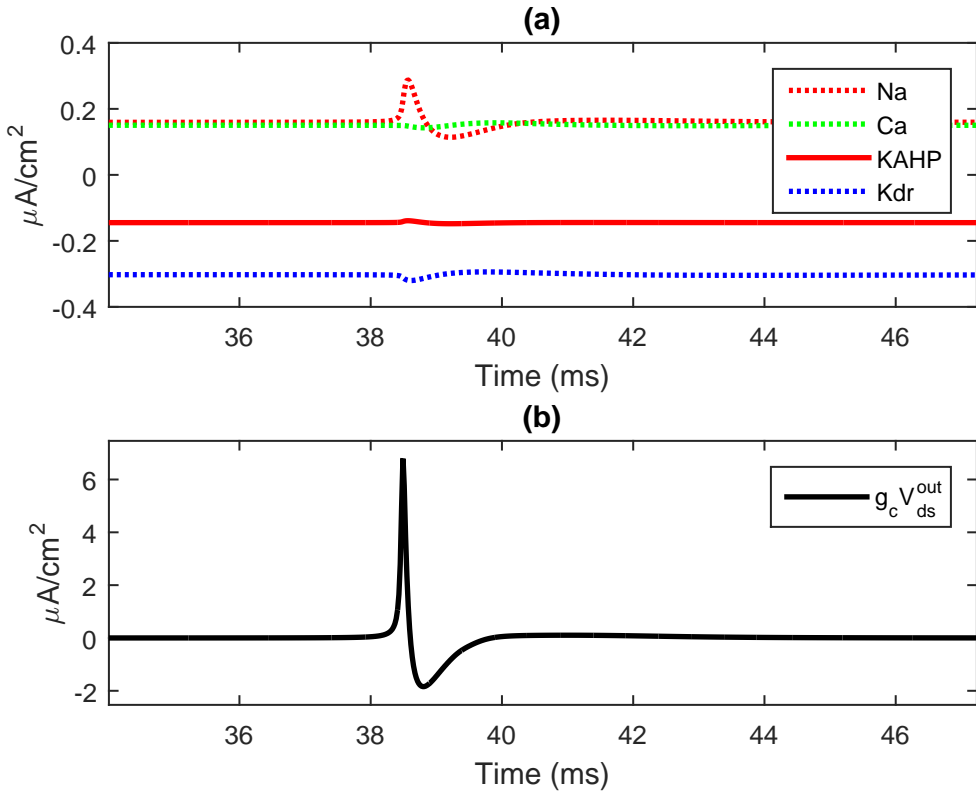


Figure 3.13: This figure illustrates the strong reaction of the sodium current compared to other nonsynaptic membrane currents. Here, a chain of PR neurons is embedded in a full resistive array (as in Fig. 3.10) but without any synaptic connectivity. Depicted are the membrane currents (a) and the polarization current,  $g_c V_{ds}^{out}$ , (b) of a neuron in response to a nearest neighbors' spike. The polarization due to an action potential is a short pulse of less than 2 ms and thus contains high-frequency components that are filtered out by slowly activating currents. Also, the response of a given current will be dependent on the activation state of the potential-dependent channels prior to the spike and associated ECC. This is just one possible state existing at the moment the ECC occurs. In this case, the neuron depicted was completely at rest without any synaptic input and  $V_s \approx -3.75$  mV, and all of the currents are at a very low activation level. We see in (a) that the very fast activating sodium current dominates the somatic Kdr, the dendritic Ca and KAHP currents. The dendritic KC current is negligible and remains constant due to the depletion of  $\text{Ca}^{2+}$ . We will show (see for example Fig. 3.17) that the overall effect of the ECC on the membrane currents is excitatory and that the dominant response of the sodium current offers an explanation.

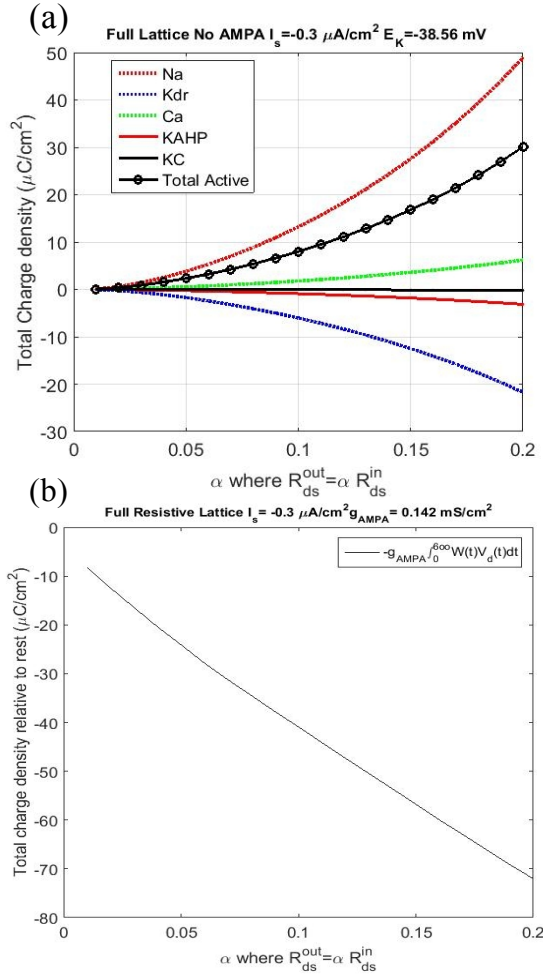


Figure 3.14: The response of the non-synaptic membrane currents and the polarization-dependent AMPA to a polarization induced by a neighboring AP on a resting neuron is characterized by integrating from when the neuron is at rest through the AP generated ECC and a sufficient time afterward until the neuron returns to rest. In this particular case, in (1) for the non-synaptic quantities we plot the total charge per  $\text{cm}^2$  from  $t = 0$  to  $t = 600$  ms.  $Q = \int_0^{600} I_{ion}(t) dt$ . In (b) we plot the total charge per  $\text{cm}^2$  for the polarization-dependent, that is  $V_d$  dependent, AMPA conductance,  $Q_{sa} = -g_{AMPA} \int_0^{600} W(t) V_d(t) dt$ . We see in (a) that the total integrated non-synaptic membrane charge (black line with circles) is positive and increases superlinearly with increasing  $R_{ds}^{out}$  and that the biggest contributor is the sodium current. In (b) we see that the increasing polarization with increasing  $R_{ds}^{out}$  leads to increasing depolarization of the post-synaptic dendritic potential and thus a decrease in AMPA. In summary, for the full lattice the response to increasing polarization due to a neighboring AP is excitatory and increases superlinearly with resistance while synaptic coupling term is inhibitory and increases linearly. For the lowest  $R_{ds}^{outs}$  the linearly increasing inhibitory synaptic coupling is dominant then as the  $R_{ds}^{out}$  continues to increase the superlinear excitatory effect of the non-synaptic currents overtakes the inhibitory effect.

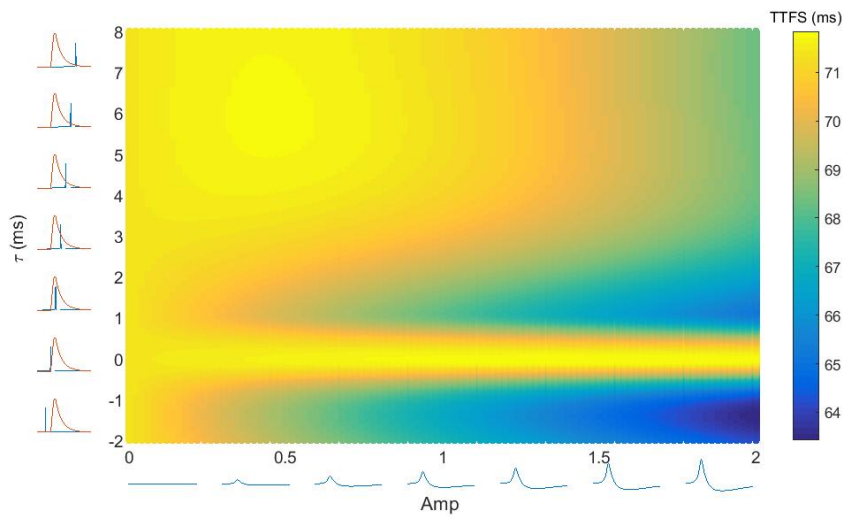


Figure 3.15: The TTFS using the single neuron model with interpolated  $V_{ds}^{out}$ . TTFS is computed as a function of both polarization amplitude and the difference in time,  $\tau$ , from the polarization due to a neighboring neuron's action potential and the initiation of synaptic AMPA. On the y-axis  $\tau$  is plotted along with graphical representation of the ECC induced polarization (blue) and the AMPA current red. The x-axis displays the amplitude which is a unitless scalar multiplying the  $V_{ds}^{out}(t)$  due to a neighboring neurons action-potential at standard resistances. Main features include peak inhibitory response around  $\tau = \tau^*$  surrounded by several milliseconds of relatively excitatory responses. For a fixed  $\tau$  the response is always more excitatory with increased polarization amplitude and thus extracellular resistance.

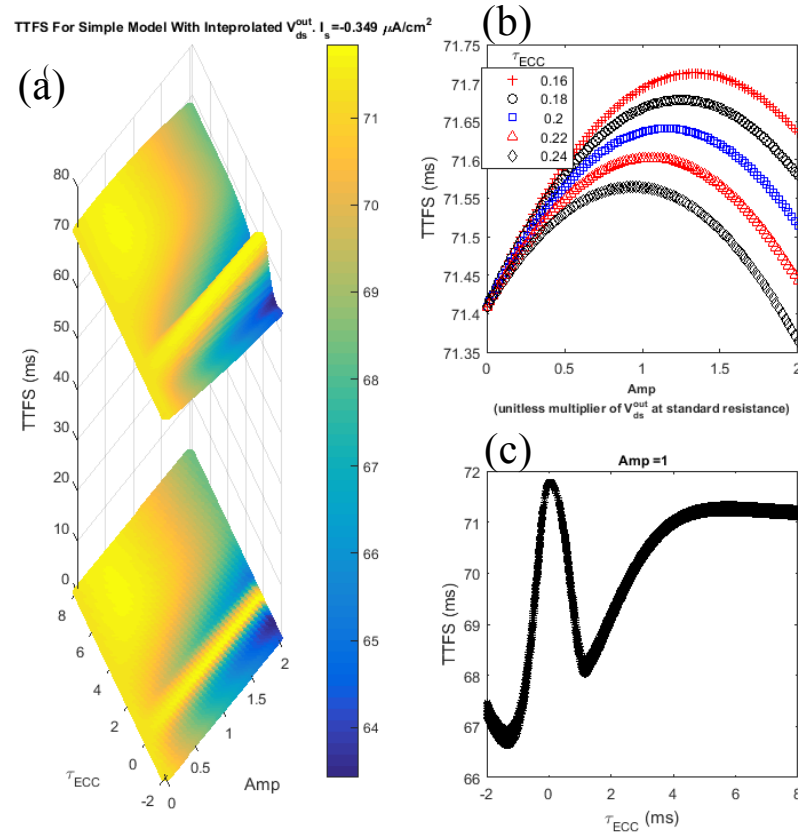


Figure 3.16: This figure shows different views of the single neuron model with interpolated  $V_{ds}^{out}$  shown in Fig. 3.15. In (a) is a three dimensional view of TTFS showing the change in TTFS as a projected height. In (b) we show for five different  $\tau$ 's around  $\tau^*$  TTFS as a function of Amp. Although the curves resemble the non-monotonic curve found using the full resistive lattice notice that the total difference in TTFS is only about 0.2 ms. In (c) for Amp=1 corresponding to  $R_{ds}^{out} = 0.1 R_{ds}^{in}$  we see the pronounced dependence on  $\tau$  around  $\tau^*$ . Also note that by  $\tau = 4$  ms the sensitivity to  $\tau$  is greatly diminished.

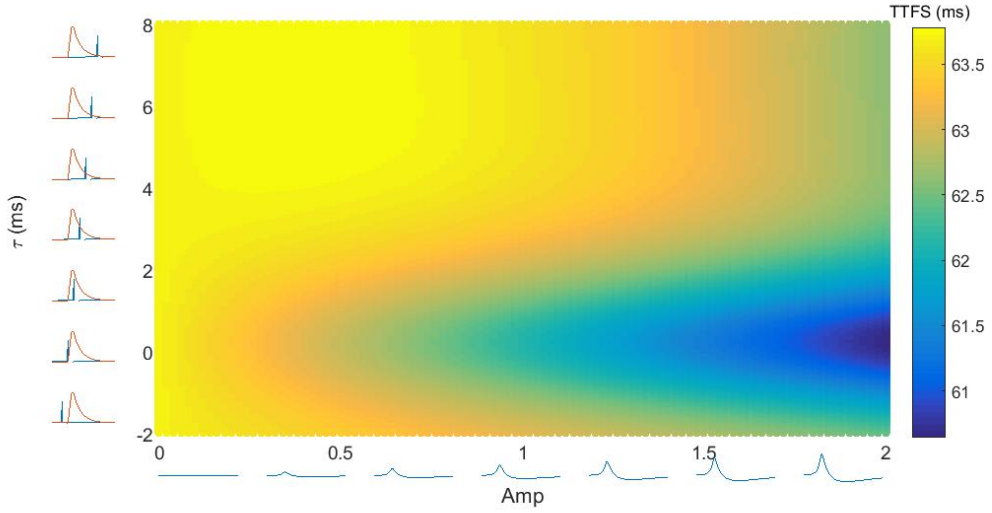


Figure 3.17: The dependence of TTFS on polarization amplitude and spike timing with synaptic coupling and source loading removed. The response is due to the non-synaptic component of localized ephaptic effect. This single-neuron model uses a linear interpolation function for both  $V_{ds}^{out}$  and AMPA. Here  $I_s = -0.3 \mu A/cm^2$ . The region of inhibition seen in Fig. 3.15 around  $\tau = \tau^*$  is now absent. What remains is an excitatory response due to the non-synaptic currents around  $\tau$  around  $\tau^*$ . This single-neuron model with interpolated  $V_{ds}^{out}$  and with synaptic coupling eliminated is perhaps most similar to experiments of bulk spike propagation in pathologically excited hippocampal tissues with synaptic currents blocked which show increasing spike propagation with increasing EC resistance.

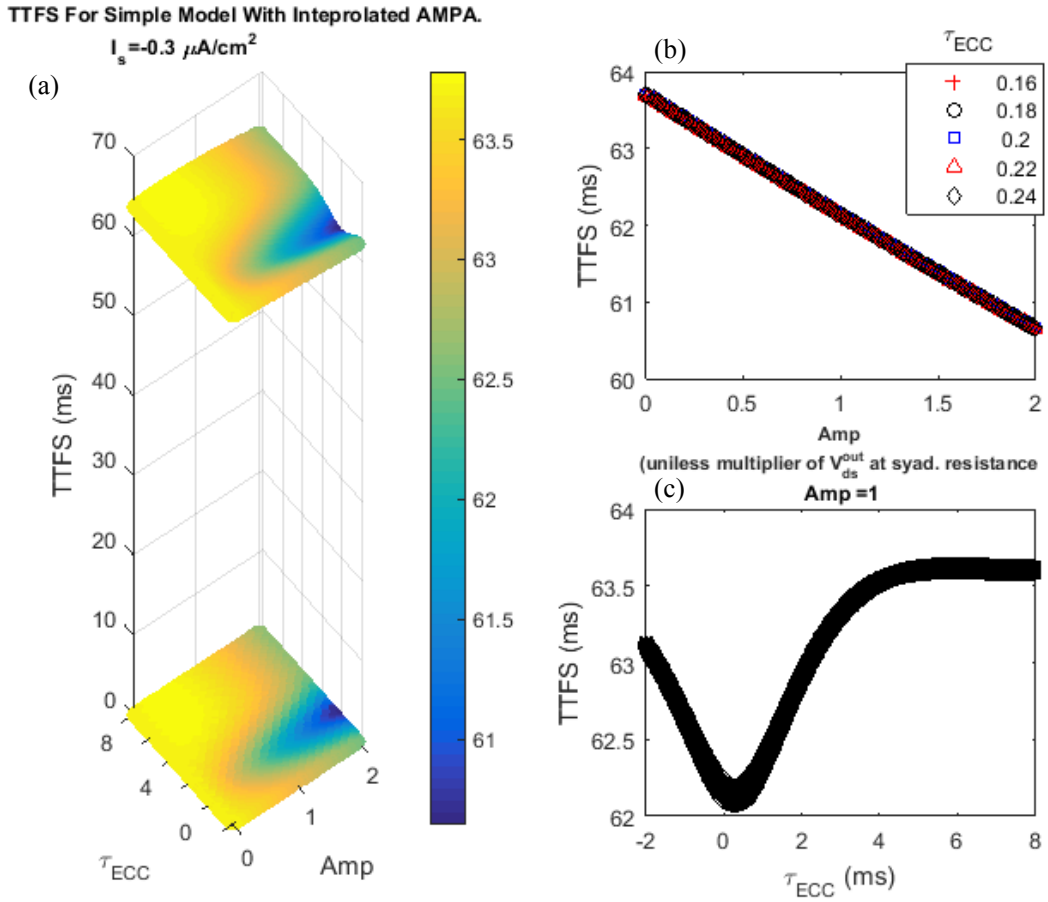


Figure 3.18: These are different views of the same data shown in Fig. 3.17. In (a) we can also visualize the response in three-dimensional projection. (b) shows that for  $\tau$  close to  $\tau^*$  the TTFS decreases linearly with increasing polarization amplitude. In (c) for Amp=1 equivalent to  $R_{ds}^{\text{out}} = 0.1R_{ds}^{\text{in}}$  the TTFS is at a minimum at  $\tau^*$  and increases as the polarization induced by a neighboring neurons spike stops overlapping the input from the interpolated AMPA.

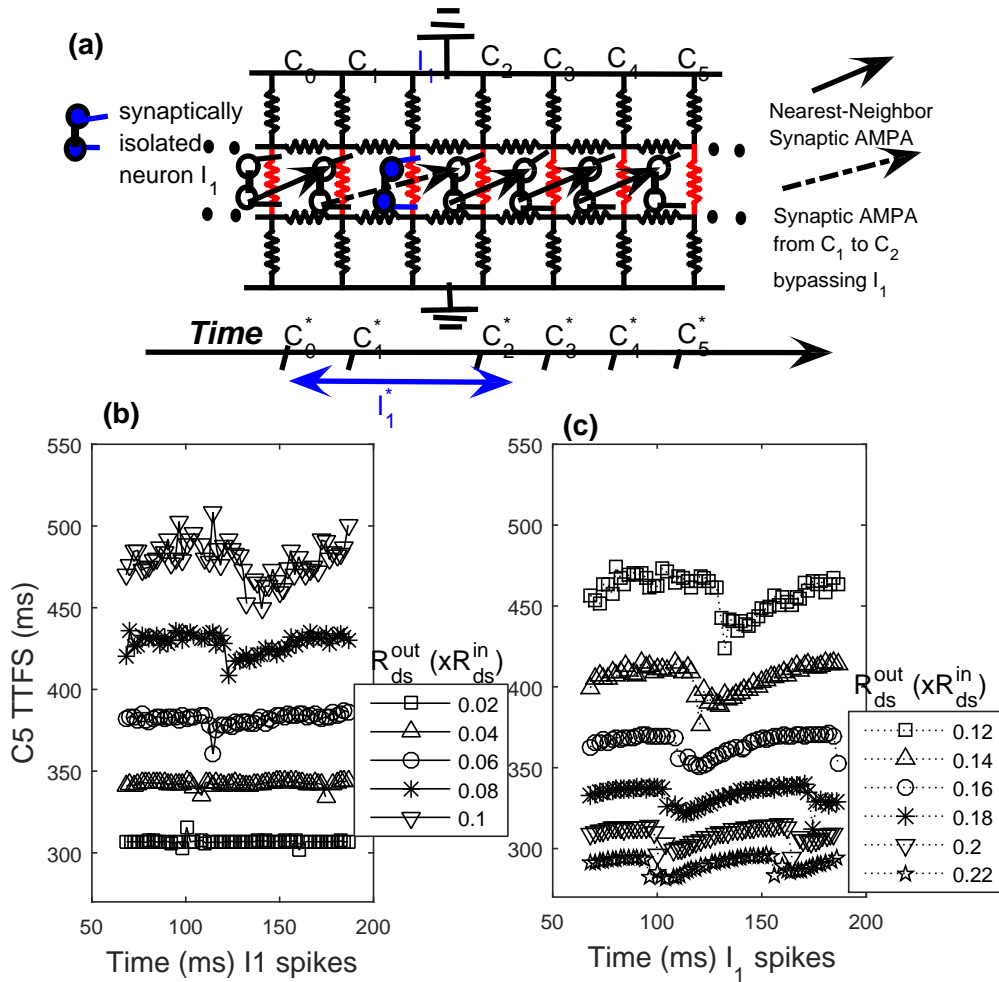


Figure 3.19: Here we show that with the full resistive lattice the spike propagation times for six sequentially excited neurons is similar to our single neuron model. Fig. 3.20 shows for a higher resolution of  $I_1$  spike times the detail when the ECC and the AMPA are within 10 ms of each other. In (a) the network architecture and stimulation protocol are illustrated in the schematic and timeline respectively. Here, we use the full resistive array with neurons  $C_0 - C_5$  unidirectionally connected to their neighbors except for the synaptic connection between  $C_1$  and  $C_2$  which bypasses the synaptically isolated randomly spiking neuron  $I_1$  (filled blue). The timeline shows the sequentially spiking  $C_1 - C_5$  (spike times are denoted with an asterisk) and a range of spiking times for the isolated neuron  $I_1^*$ . By varying  $I_1^*$  we are changing the relative time between the ECC and the AMPA current analogous to varying  $\tau_{ECC}$  for the single neuron models Fig. 3.16. (b) and (c) plot  $C_5^*$  for five and six different  $R_{ds}^{out}$  respectively. As with the TTFS in Fig. 3.10, the mean level of the  $C_5$  TTFS is unimodal with respect to increasing  $R_{ds}^{out}$ . The unimodal profile is hard to recognize since (b) and (c) split the results into increasing and decreasing TTFS. Observe that in (b)  $C_5$  TTFS at  $R_{ds}^{out} = 0.02R_{ds}^{in}$  (square) the TTFS is slightly above 300 ms. Then as  $R_{ds}^{out}$  increases up to  $R_{ds}^{out} = 0.1R_{ds}^{in}$  (down triangle) so does the TTFS.

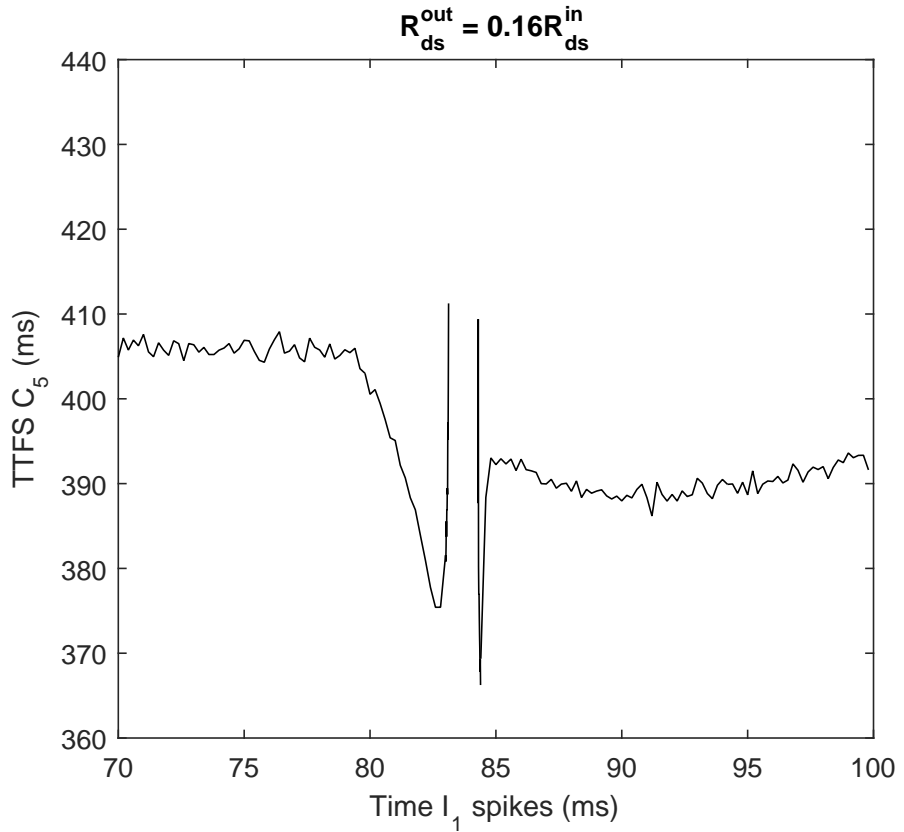


Figure 3.20: A step size of 0.01 ms for  $I_1^*$  reveals important structure not evident in Fig. 3.19. Shown here is a zoomed in look of the TTFS with open circles in Fig. 3.19 (c) with  $R_{ds}^{out} = 0.16R_{ds}^{in}$ . At the top of what we called the parabolic feature for the single-neuron model around 84 ms spike propagation has failed at  $C_2$ . This again shows the importance of the AMPA-ECC coupling effect. For a difference of a fraction of a millisecond in the spike time of  $I_1$   $C_2$  goes from spiking about 30 – 40% faster to failing to spike.

## Chapter 4: Conclusion

Using computational models drawn from experimental data, we consider both the effects of uniform constant electric fields and the brief oscillating currents associated with a single spiking neuron, on neural excitability. In Chapter 2 we identified novel polarization-dependent excitability that should be amenable to experimental verification. One of the main findings was the significance of the relative strength of depolarizing and hyperpolarizing currents as the polarization is increased. Slight changes in physiological parameters would yield slight changes in the TTFS at weak polarizations but at stronger polarization these trajectories could diverge significantly. In Chapter 3 we investigated the effects of extracellular currents generated from a neurons' action potential on the excitability of neighboring neurons in a chain. We used the same computational model for a single neuron used in Chapter 2 but created a synaptically connected chain that was then embedded in a resistive lattice. This work was driven largely by the observation of non-monotonicity in the spike propagation times with increasing extracellular resistance. The findings were especially compelling since the range of resistances for which the non-monotonicity was well-defined fell within the range of resistance inferred by measured resistivity and extracellular dimensions. To explain the non-monotonicity we segregate the localized ephaptic effects described by the high-dimensional nonlinear coupled ODE into three components. The segregation into source loading, synaptic coupling, and nonsynaptic membrane currents proved fruitful. We found that the source loading was always inhibitory and the nonsynaptic membrane currents always excitatory. The synaptic coupling could be either excitatory or inhibitory with a complex response to both timing and extracellular resistance.

This work contributes to our understanding of the complex interactions of electric fields and neurons. We have utilized similar computational methods to investigate both strong

static fields and very weak oscillating endogenous fields. Our results have a number of implications and insights into the modulation of neural activity using applied DC fields. This work is relevant to existing and future medical applications. Our work on localized ephaptic effects due to individual action potentials sheds a light on an often overlooked aspect of the general problem of endogenous fields and ephaptic effects. Our work qualitatively predicts and explains how spike propagation times vary in response to both changes in extracellular resistance and the timing of excitatory synaptic input relative to the extracellular currents. Implications for our work on localized ephaptic effects include memory encoding and retrieval and neural synchrony.

## Bibliography

## Bibliography

- [1] D. Gasparini, S DiFrancesco, “Action of serotonin on the hyperpolarization-activated cation current ( $i_h$ ) in rat ca1 hippocampal neurons,” *European Journal Of Neuroscience*, 1999.
- [2] A. Lippert and V. Booth, “Understanding effects on excitability of simulated  $I_h$  modulation in simple neuronal models.,,” *Biological Cybernetics*,, 2009.
- [3] L. Galvani. ACademia della Scienze, 1791.
- [4] P. F. Pinsky and J. Rinzel, “Intrinsic and network rhythmogenesis in a reduced traub model for ca3 neurons,” *Journal of Computational Neuroscience*, vol. 1, no. 1-2, pp. 39–60, June 1994.
- [5] R. Traub, J. Jefferys, and M. Whittington, “Enhanced nmda conductance can account for epileptiform activity-induced by low mg<sup>2+</sup> in the rat hippocampal slice,” *Journal Of Physiology-London*, vol. 478, no. 3, pp. 379–393, AUG 1 1994.
- [6] B. J. Gluckman, P. So, T. I. Netoff, M. L. Spano, and S. J. Schiff, “Stochastic resonance in mammalian neuronal networks,” *Chaos: An Interdisciplinary Journal of Nonlinear Science*, vol. 8, no. 3, pp. 588–598, 1998. [Online]. Available: <http://link.aip.org/link/?CHA/8/588/1>
- [7] E.-H. Park, P. So, E. Barreto, B. Gluckman, and S. Schiff, “Electric field modulation of synchronization in neuronal networks,” *Neurocomputing*, vol. 52-54, pp. 169–175, 2003. [Online]. Available: <http://www.sciencedirect.com/science/article/B6V10-47T2GNT-K/2/5e5a42a4855dfd83da36607af3a75b8e>
- [8] E.-H. Park, E. Barreto, B. J. Gluckman, S. J. Schiff, and P. So, “A model of the effects of applied electric fields on neuronal synchronization,” *Journal of Computational Neuroscience*, vol. 19, pp. 53–70, august 2005. [Online]. Available: <http://www.springerlink.com/content/w1681302gth46592>
- [9] R. Traub, F. Dudek, R. Snow, and W. Knowles, “Computer simulations indicate that electrical field effects contribute to the shape of the epileptiform field potential,” *Neuroscience*, vol. 15, no. 4, pp. 947–958, 1985.
- [10] R. Reznik, E. Barreto, E. Sander, and P. So, “Effects of polarization induced by non-weak electric fields on the excitability of elongated neurons with active dendrites,” *Journal of Computational Neuroscience*, pp. 1–24, 2015. [Online]. Available: <http://dx.doi.org/10.1007/s10827-015-0582-4>

- [11] B. Ermentrout, *Simulating, Analyzing, and Animating Dynamical Systems*, J. J. Don-garra, Ed. SIAM, 2002.
- [12] C.-L. Han, W. Hu, M. Stead, T. Zhang, J.-G. Zhang, G. A. Worrell, and F.-G. Meng, “Electrical stimulation of hippocampus for the treatment of refractory temporal lobe epilepsy,” *Brain Research Bulletin*, vol. 109, no. 0, pp. 13 – 21, 2014. [Online]. Available: <http://www.sciencedirect.com/science/article/pii/S0361923014001336>
- [13] M. Bikson, M. Inoue, H. Akiyama, D. J. K, J. Fox, H. Miyakawa, and J. Jefferys, “Effects of uniform extracellular dc electric fields on excitability in rat hippocampal slices in vitro,” *J Physiol*, vol. 557.1, pp. 175–190, 2004.
- [14] B. J. Gluckman, H. Nguyen, S. L. Weinstein, and S. J. Schiff, “Adaptive electric field control of epileptic seizures,” *J. Neurosci.*, vol. 21, no. 2, pp. 590–600, 2001. [Online]. Available: <http://www.jneurosci.org/cgi/content/abstract/21/2/590>
- [15] R. Ghai, M. Bikson, and D. Durand, “Effects of applied electric fields on low-calcium epileptiform activity in the ca1 region of rat hippocampal slices,” *Journal Of Neurophysiology*, vol. 84, no. 1, pp. 274–280, JUL 2000.
- [16] B. J. Gluckman, E. J. Neel, T. I. Netoff, W. L. Ditto, M. L. Spano, and S. J. Schiff, “Electric field suppression of epileptiform activity in hippocampal slices,” *J Neurophysiol*, vol. 76, no. 6, pp. 4202–4205, 1996. [Online]. Available: <http://jn.physiology.org/cgi/content/abstract/76/6/4202>
- [17] R. Mikkelsen, M. Andreasen, and S. Nedergaard, “Suppression of epileptiform activity by a single short-duration electric field in rat hippocampus in vitro,” *Journal of Neurophysiology*, vol. 109, no. 11, pp. 2720–2731, 2013.
- [18] S. Sunderam, N. Chernyy, N. Peixoto, J. P. Mason, S. L. Weinstein, S. J. Schiff, and B. J. Gluckman, “Seizure entrainment with polarizing low-frequency electric fields in a chronic animal epilepsy model,” *Journal Of Neural Engineering*, vol. 6, no. 4, AUG 2009, in Vivo very low freq to modulate excitability in tetanically induced epileptic rats.
- [19] K. A. Richardson, B. J. Gluckman, S. L. Weinstein, C. E. Glosch, J. B. Moon, R. P. Gwinn, K. Gale, and S. J. Schiff, “In vivo modulation of hippocampal epileptiform activity with radial electric fields.” *Epilepsia Series 4)*, vol. 44, no. 6, pp. p768 – 777, 2003.
- [20] M. Bikson and A. Rahman, “Origins of specificity during tdcS: anatomical, activity-selective, and input-bias mechanisms,” *Frontiers in Human Neuroscience*, vol. 7, no. 688, 2013.
- [21] P. C. Miranda, M. Lomarev, and M. Hallett, “Modeling the current distribution during transcranial direct current stimulation,” *Clinical Neurophysiology*, vol. 117, no. 7, pp. 1623 – 1629, 2006. [Online]. Available: <http://www.sciencedirect.com/science/article/pii/S1388245706001726>
- [22] S. A. Weiss and D. S. Faber, “Field effects in the CNS play functional roles,” *Frontiers In Neural Circuits*, vol. 4, May 18 2010.

- [23] J. K. Deans, A. D. Powell, and J. G. R. Jefferys, "Sensitivity of coherent oscillations in rat hippocampus to ac electric fields," *JOURNAL OF PHYSIOLOGY-LONDON*, vol. 583, no. 2, pp. 555–565, SEP 1 2007.
- [24] T. Radman, Y. Su, J. H. An, L. C. Parra, and M. Bikson, "Spike timing amplifies the effect of electric fields on neurons: Implication for endogenous field effects," *The Journal of Neuroscience*, vol. 27, pp. 3030–3036, 2007.
- [25] T. Radman, R. L. Ramos, J. C. Brumberg, and M. Bikson, "Role of cortical cell type and morphology in subthreshold and suprathreshold uniform electric field stimulation in vitro," *Brain Stimulation*, vol. 2, pp. 215–228, 2009, experimental and Theoretic polarization of neuron.
- [26] I. Dietzel, U. Heinemann, and H. Lux, "Relations between slow extracellular potential changes, glial potassium buffering, and electrolyte and cellular-volume changes during neuronal hyperactivity in cat brain," *Glia*, vol. 2, no. 1, pp. 25–44, 1989.
- [27] J. T. Francis, B. J. Gluckman, and S. J. Schiff, "Sensitivity of neurons to weak electric fields," *J. Neurosci.*, vol. 23, no. 19, pp. 7255–7261, 2003, experimental weak EField minimum to cause response. [Online]. Available: <http://www.jneurosci.org/cgi/content/abstract/23/19/7255>
- [28] G. Pucihaar, D. Miklavcic, and T. Kotnik, "A time-dependent numerical model of transmembrane voltage induction and electroporation of irregularly shaped cells," *Biomedical Engineering, IEEE Transactions on*, vol. 56, no. 5, pp. 1491 –1501, may 2009.
- [29] J. Berzhanskaya, A. Gorchetchnikov, and S. J. Schiff, "Switching between gamma and theta: Dynamic network control using subthreshold electric fields," *Neurocomputing*, vol. 70, no. 10-12, pp. 2091 – 2095, 2007, computational, neural circuitry. [Online]. Available: <http://www.sciencedirect.com/science/article/B6V10-4M9Y1V1-G/2/05a532a351f790864e8ff5511052b9c3>
- [30] D. Reato, A. Rahman, M. Bikson, and L. C. Parra, "Low-intensity electrical stimulation affects network dynamics by modulating population rate and spike timing," *J. Neurosci.*, vol. 30, no. 45, pp. 15 067–15 079, 2010. [Online]. Available: <http://www.jneurosci.org/cgi/content/abstract/30/45/15067>
- [31] R. Traub, F. Dudek, C. P. Taylor, and W. D. Knowles, "Simulation of hippocampal afterdischarges synchronized by electrical interactions," *Neuroscience*, vol. 14, pp. 1033–1038, 1985.
- [32] R. D. Traub, R. K. Wong, R. Miles, and H. Michelson, "A model of a ca3 hippocampal pyramidal neuron incorporating voltage-clamp data on intrinsic conductances," *J Neurophysiol*, vol. 66, no. 2, pp. 635–650, 1991. [Online]. Available: <http://jn.physiology.org/cgi/content/abstract/66/2/635>
- [33] G.-S. Yi, J. Wang, X.-L. Wei, K.-M. Tsang, W.-L. Chan, B. Deng, and C.-X. Han, "Exploring how extracellular electric field modulates neuron activity through dynamical analysis of a two-compartment neuron model," *Journal of*

*Computational Neuroscience*, vol. 36, no. 3, pp. 383–399, 2014. [Online]. Available: <http://dx.doi.org/10.1007/s10827-013-0479-z>

- [34] J. Csicsvari, B. Jamieson, K. Wise, and G. Buzsaki, “Mechanisms of gamma oscillations in the hippocampus of the behaving rat,” *NEURON*, vol. 37, no. 2, pp. 311–322, JAN 23 2003.
- [35] K. A. Richardson, S. J. Schiff, and B. J. Gluckman, “Control of traveling waves in the mammalian cortex,” *Phys. Rev. Lett.*, vol. 94, no. 2, p. 028103, Jan 2005. [Online]. Available: <http://prola.aps.org.mutex.gmu.edu/abstract/PRL/v94/i2/e028103>
- [36] G. R. Holt and C. Koch, “Electrical interactions via the extracellular potential near cell bodies,” *Journal of Computational Neuroscience*, vol. 6, no. 2, pp. 169–184, March 1999. [Online]. Available: <http://www.springerlink.com.mutex.gmu.edu/content/u262m146864wu008/fulltext.pdf>
- [37] D. Tranchina and C. Nicholson, “A model for the polarization of neurons by extrinsically applied electric fields,” *Biophysical Journal*, vol. 50, pp. 1139–1156, 1986.
- [38] E. Vigmond, J. L. P. Velazquez, T. A. Valiante, B. L. Bardakjian, and P. L. Carlen, “Mechanisms of electrical coupling between pyramidal cells,” *J Neurophysiol*, vol. 78, pp. 3107–3116, 1997.
- [39] R. D. Traub and R. Miles, *Neuronal Networks of the Hippocampus*. Cambridge, 1991.
- [40] W. J. Moody, K. J. Futamachi, and D. A. Prince, “Extracellular potassium activity during epileptogenesis,” *Experimental Neurology*, vol. 42, no. 2, pp. 248 – 263, 1974. [Online]. Available: <http://www.sciencedirect.com/science/article/B6WFG-4BJW0K8-S5/2/5a1576e44b031b336a2de8069c9f4a03>
- [41] J. Cressman, JohnR., G. Ullah, J. Ziburkus, S. Schiff, and E. Barreto, “The influence of sodium and potassium dynamics on excitability, seizures, and the stability of persistent states: I. single neuron dynamics,” *Journal of Computational Neuroscience*, vol. 26, no. 2, pp. 159–170, 2009. [Online]. Available: <http://dx.doi.org/10.1007/s10827-008-0132-4>
- [42] J. Cressman, G. Ullah, J. Ziburkus, S. Schiff, and E. Barreto, “Erratum to: The influence of sodium and potassium dynamics on excitability, seizures, and the stability of persistent states: I. single neuron dynamics,” *Journal of Computational Neuroscience*, vol. 30, no. 3, pp. 781–781, 2011. [Online]. Available: <http://dx.doi.org/10.1007/s10827-011-0333-0>
- [43] E. Barreto and J. Cressman, “Ion concentration dynamics as a mechanism for neuronal bursting,” *Journal of Biological Physics*, vol. 37, no. 3, pp. 361–373, 2011. [Online]. Available: <http://dx.doi.org/10.1007/s10867-010-9212-6>
- [44] J. McNamara, “Cellular and molecular basis of epilepsy,” *J. Neurosci.*, vol. 14, no. 6, pp. 3413–3425, 1994. [Online]. Available: <http://www.jneurosci.org>
- [45] N. Golding, T. Mickus, Y. Katz, W. Kath, and N. Spruston, “Factors mediating powerful voltage attenuation along ca1 pyramidal neuron dendrites,” *Journal Of Physiology-London*, 2005.

- [46] J. Dyhrfjeld-Johnsen, R. J. Morgan, and I. Soltesz, “Double trouble? potential for hyperexcitability following both channelopathic up- and downregulation of i(h) in epilepsy.” *Frontiers in neuroscience*, 2009.
- [47] D. Janigro, “Brain water and ion fluxes: a hard-to-die hypothesis to explain seizure,” *Epilepsy Currents*, 2006.
- [48] D. Binder, X. Yao, Z. Zador, T. Sick, A. Verkman, and G. Manley, “Increased seizure duration and slowed potassium kinetics in mice lacking aquaporin-4 water channels,” *GLIA*, vol. 53, no. 6, pp. 631–636, APR 15 2006.
- [49] A. Bose and V. Booth, *Bursting in 2-compartment neurons: A case study of the Pinsky-Rinzel model*, CAMS, Ed. Center for Applied Mathematics and Statistics, 2004.
- [50] C. Qiu, R. S. Shivacharan, M. M. Zhang, and D. M. Durand, “Can neural activity propagate by endogenous electrical field?” *Journal Of Neuroscience*, 2015.
- [51] C. A. Anastassiou, R. Perin, H. Markram, and C. Koch, “Ephaptic coupling of cortical neurons,” *Nature Neuroscience*, vol. 14, no. 2, pp. 217–U304, FEB 2011.
- [52] C. P. Taylor and F. E. Dudek, “A physiological test for electrotonic coupling between cal pyramidal cells in rat hippocampal slices,” *Brain Research*, vol. 285, pp. 351–357, 1982.
- [53] Taylor and Dudek, “Synchronization without active chemical synapses during hippocampal afterdischarges,” *J Neurophysiol*, vol. 52, no. 1, pp. 143–155, 1984, ephaptic. [Online]. Available: <http://jn.physiology.org/cgi/content/abstract/52/1/143>
- [54] J. Jefferys and H. Haas, “Synchronized Bursting of CA1 Hippocampal Pyramidal Cells In The Absence Of Synaptic Transmission,” *NATURE*, vol. 300, no. 5891, pp. 448–450, 1982.
- [55] R. W. Snow and F. E. Dudek, “Electrical fields directly contribute to action-potential synchronization during convulsant-induced epileptiform bursts,” *Brain Research*, 1984.
- [56] J. Okeefe, “review Of The Hippocampal Place Cells,” *progress In Neurobiology*, vol. 13, no. 4, pp. 419–439, 1979.
- [57] J. Okeefe and M. Recce, “Phase relationship between hippocampal place units and the eeg theta-rhythm,” *Hippocampus*, vol. 3, no. 3, pp. 317–330, JUL 1993.
- [58] W. Skaggs, B. McNaughton, M. Wilson, and C. Barnes, “Theta phase precession in hippocampal neuronal populations and the compression of temporal sequences,” *HIPPOCAMPUS*, vol. 6, no. 2, pp. 149–172, 1996.
- [59] M. Cong, W. Jiang, Q. Ying-Mei, W. Xi-Le, C. Yan-Qiu, and D. Bin, “Spiking patterns of a hippocampus model in electric fields,” *Chinese Physics B*, vol. 20, no. 12, DEC 2011.
- [60] C. A. Anastassiou and C. Koch, “Ephaptic coupling to endogenous electric field activity: why bother?” *Current Opinion in Neurobiology*, vol. 31, no. 0, pp. 95 – 103, 2015, sI: Brain rhythms and dynamic coordination. [Online]. Available: <http://www.sciencedirect.com/science/article/pii/S0959438814001809>

- [61] J. G. R. Jefferys, "Nonsynaptic modulation of neuronal activity in the brain: Electric currents and extracellular ions," *Physiological Reviews*, vol. 75, no. 4, pp. 689–723, October 1995.
- [62] L. de Almeida, M. Idiart, and J. E. Lisman, "Memory retrieval time and memory capacity of the ca3 network: Role of gamma frequency oscillations," *Learning & Memory*, vol. 14, no. 11, pp. 795–806, 2007. [Online]. Available: <http://learnmem.cshlp.org/content/14/11/795.abstract>
- [63] C. A. Anastassiou, S. M. Montgomery, M. Barahona, G. Buzsaki, and C. Koch, "The effect of spatially inhomogeneous extracellular electric fields on neurons," *Journal Of Neuroscience*, vol. 30, no. 5, pp. 1925–1936, FEB 3 2010, ephaptic.
- [64] F. Froehlich and D. A. McCormick, "Endogenous electric fields may guide neocortical network activity," *NEURON*, vol. 67, no. 1, pp. 129–143, JUL 15 2010.
- [65] X. Wei, Y. Chen, M. Lu, B. Deng, H. Yu, J. Wang, Y. Che, and C. Han, "An ephaptic transmission model of ca3 pyramidal cells: an investigation into electric field effects," *Cognitive Neurodynamics*, vol. 8, no. 3, pp. 177–197, 2014. [Online]. Available: <http://dx.doi.org/10.1007/s11571-013-9269-6>
- [66] S. W. Kuffler and D. D. Potter, "Glia in the leech central nervous system: Physiological properties and neuron-glia relationship," *Journal of Neurophysiology*, vol. 27, no. 2, pp. 290–320, 1964.
- [67] C. J. McBain, S. F. Traynelis, and R. Dingledine, "Regional variation of extracellular space in the hippocampus," *Science*, vol. 249, pp. 674–677, 1990.
- [68] E. Sykova, "Diffusion properties of the brain in health and disease," *Neurochemistry International*, vol. 45, no. 4, pp. 453–466, SEP 2004.
- [69] G. Buzsaki, C. A. Anastassiou, and C. Koch, "The origin of extracellular fields and currents - eeg, ecog, lfp and spikes," *Nature Reviews Neuroscience*, vol. 13, no. 6, pp. 407–420, JUN 2012.
- [70] C. Bedard, H. Kroger, and A. Destexhey, "Modeling extracellular field potentials and the frequency-filtering properties of extracellular space," *Biophysical Journal*, vol. 86, pp. 1829–1842, 2004, frequency filtering extra-cellular currents.
- [71] A. Hodgkin, "The local electric changes associated with repetitive action in a non-medullated axon," *J. Phsiol.*, 1948.
- [72] B. Ermentrout, "Type 1 membranes, phase resetting curves, and synchrony," *Neural Computation*, 1996.
- [73] F. Skinner, "Moving beyond type i and type ii neuron types," *F1000Research 2013, 2:19 (doi: 10.12688/f1000research.2-19.v1)*, 2013.
- [74] E. M. Izhikevich, *Dynamical Systems in Neuroscience: The Geometry of Excitability and Bursting*. MIT Press, 2007.

- [75] S. A. Prescott, S. Ratte, Y. De Koninck, and T. J. Sejnowski, “Pyramidal neurons switch from integrators in vitro to resonators under in vivo-like conditions,” *Journal Of Neurophysiology*, vol. 100, no. 6, pp. 3030–3042, DEC 2008.
- [76] A. Destexhe, “The high-conductance state of neocortical neurons in vivo.” *Nat Rev Neuroscience*, 2003.
- [77] J. Ranck, “Electrical Impedance In Subicular Area Of Rats During Paradoxical Sleep,” *Experimental Neurology*, vol. 16, no. 4, pp. 416–&, 1966.
- [78] G. Pyapali, A. Sik, M. Penttonen, G. Buzsaki, and D. Turner, “Dendritic properties of hippocampal ca1 pyramidal neurons in the rat: Intracellular staining in vivo and in vitro,” *Journal Of Comparative Neurology*, vol. 391, no. 3, pp. 335–352, FEB 16 1998.
- [79] L. Lopez-Aguado, J. Ibarz, and O. Herreras, “Activity-dependent changes of tissue resistivity in the Ca1 region in vivo are layer-specific: Modulation of evoked potentials,” *NEUROSCIENCE*, vol. 108, no. 2, pp. 249–262, 2001.
- [80] J. Fox, M. Bikson, and J. Jefferys, “Tissue resistance changes and the profile of synchronized neuronal activity during ictal events in the low-calcium model of epilepsy,” *Journal Of Neurophysiology*, vol. 92, no. 1, pp. 181–188, JUL 2004.
- [81] E. Sykova and C. Nicholson, “Diffusion in brain extracellular space,” *Physiological Reviews*, vol. 88, no. 4, pp. 1277–1340, OCT 2008.
- [82] A. D. Sherpa, P. van de Nes, F. Xiao, J. Weedon, and S. Hrabetova, “Gliotoxin-induced swelling of astrocytes hinders diffusion in brain extracellular space via formation of dead-space microdomains,” *GLIA*, vol. 62, no. 7, pp. 1053–1065, JUL 2014.
- [83] S. Gabriel, R. Lau, and C. Gabriel, “The dielectric properties of biological tissues .2. Measurements in the frequency range 10 Hz to 20 GHz,” *Physics In Medicine And Biology*, vol. 41, no. 11, pp. 2251–2269, NOV 1996.
- [84] C. Bedard, S. Rodrigues, N. Roy, D. Contreras, and A. Destexhe, “Evidence for frequency-dependent extracellular impedance from the transfer function between extracellular and intracellular potentials,” *Journal Of Computational Neuroscience*, vol. 29, no. 3, pp. 389–403, DEC 2010.
- [85] C. Gold, D. A. Henze, C. Koch, and G. Buzsaki, “On the origin of the extracellular action potential waveform: A modeling study,” *J Neurophysiol*, vol. 95, no. 5, pp. 3113–3128, 2006. [Online]. Available: <http://jn.physiology.org/cgi/content/abstract/95/5/3113>
- [86] E. W. Schomburg, C. A. Anastassiou, G. Buzsaki, and C. Koch, “The spiking component of oscillatory extracellular potentials in the rat hippocampus,” *JOURNAL OF NEUROSCIENCE*, vol. 32, no. 34, pp. 11 798–11 811, AUG 22 2012.
- [87] S. Weiss, M. J. G, R. Goodman, R. G. Emerson, A. Trevelyn, M. Bikson, and C. A. Schevon, “Field effects and ictal synchronization: insights from in homine observations,” *Frontiers In Human Neuroscience*, 2013.

- [88] P. Dayan and L. Abbott, *Theoretical Neuroscience*, T. J. Sejnowski and T. Poggio, Eds. The MIT Press, 2001.
- [89] A. D. Sherpa, P. van de Nes, F. Xiao, J. Weedon, and S. Hrabetova, “Gliotoxin-induced swelling of astrocytes hinders diffusion in brain extracellular space via formation of dead-space microdomains,” *GLIA*, vol. 62, no. 7, pp. 1053–1065, JUL 2014.
- [90] R. Thorne and C. Nicholson, “In vivo diffusion analysis with quantum dots and dextrans predicts the width of brain extracellular space,” *Proceedings Of The National Academy Of Sciences Of The United States Of America*, vol. 103, no. 14, pp. 5567–5572, APR 4 2006.
- [91] J. Hrabe, S. Hrabov, and K. Segeth, “A model of effective diffusion and tortuosity in the extracellular space of the brain,” *Biophysical Journal*, vol. 87, no. 3, pp. 1606 – 1617, 2004. [Online]. Available: <http://www.sciencedirect.com/science/article/pii/S0006349504736425>

## **Curriculum Vitae**

Robert I. Reznik received a B.S. in Honors Physics from University of Pittsburgh in 1992. M.S. in Physics in 1995. Since then he has worked for Leidos (formerly SAIC) as a scientist, systems analyst, and project manager. At Leidos he has had the privelage of working on a wide range of problems including those related to Aerospace, Optics, and detection and tracking.